

Brewster Angle Microscopy Study of Model Lung Surfactant Systems at the Air-Water
and Air-Physiological Buffer Interfaces

Thesis

Presented in Partial Fulfillment of the Requirements for the Degree Master of Science
in the Graduate School of The Ohio State University

By

Hardy Zingalaoa Castada, B.S.

Graduate Program in Chemistry

The Ohio State University

2010

Thesis Committee:

Heather C. Allen, Advisor

Susan V. Olesik

Copyright by
Hardy Zingalaoa Castada
2010

ABSTRACT

The lungs have the ability to function normally due to its physiological and molecular components. In the lungs, air is delivered to the bloodstream through the bronchi down to the lower airways that divide into smaller branches called bronchioles and eventually reaching the alveoli or air sacs. Type II cells of the alveolar epithelium produces natural lung surfactants to line the alveolar walls, reduce the surface tension in the alveoli and maintain a large surface area so gas exchange can easily take place. Absence or reduction of these natural lung surfactants could increase the surface tension leading to collapse of the alveoli and stiffening of the lungs causing the impairment of gas exchange, which could ultimately cause life threatening diseases.

Different replacement lung surfactants (RLS) are currently used worldwide to supplement the lack of natural lung surfactants, especially in premature babies. RLS vary in their formulations and can be derived from animal or synthetic sources.

Current research involves the study of the different compounds making up these natural or replacement lung surfactants. Model lung surfactant systems are created and studied in vitro to be able to have a better understanding of the structure, function and the physicochemical aspects of individual and mixed components, which are all are valuable in formulating better design for replacement lung surfactants.

This thesis presents the building and testing of the Brewster angle microscope (BAM) in the Allen laboratory. The behavior of the different components of lung surfactant model systems on water and physiological buffer (pH 7) subphase acquired through surface pressure-area isotherms and BAM images are also presented. This thesis also demonstrates that the monolayer formed by various individual and mixed lipids and fatty acid behave differently at different subphase at room temperature of $23 \pm 1^\circ\text{C}$. Shifting of the surface-pressure area isotherms of all lung surfactant model systems towards higher mean molecular areas when spread on the buffer subphase was observed. Various theories exist explaining such shifting and are explored in this thesis. Furthermore, the fluidizing effect of POPG and condensing effect of PA in their binary and ternary mixtures were observed. Also, the effect of KL₄ (a 21 amino acid peptide that is believed to mimic the structure of the surface protein SP-B in natural lung surfactants) in the ternary mixture of DPPC-POPG-PA spread on the buffer subphase was explored and observed to play a part in the formation of more condensed phase in the system.

This thesis is dedicated to my wife and twin pokokoys.

ACKNOWLEDGMENTS

It is a great honor and privilege for me to have worked in the Department of Chemistry at The Ohio State University, more so to work on a thesis and having been able to set it down in black and white. With this, it is my pleasure to thank those who have contributed towards the realization of this thesis. I could not possibly do what I was able to accomplish without the approval of my adviser, Dr. Heather Allen, for allowing me to work in the laser world of the Allen laboratory and to be one of her advisees. Her strong motivations and worthy supervisions have contributed the greatest in the completion of this thesis. To Dr. James Rathman, for lending me the objective lenses (Nikon 10x, 20x, and 50x), which by far are the most important optics in the BAM. To Mr. Larry Antal of the Department of Chemistry-Machine Shop for his notable fabrication of the goniometer. To the Allen group, especially to Dr. Casillas-Ituarte, Dr. Sierra-Hernandez, Dr. Tang and Dr. Cheng for their invaluable help and scholarly insights. To Ms. Minette Ocampo, my accomplice in applying to graduate school, and whose support and friendship has served me a long way. To my inspiration, my wife Hanna, whose love has kept my sanity intact and whose encouragement made me go this far. To my motivation and joy, our twins, as we patiently expect their arrival. Above all, to God, who makes all things possible and has made everything mentioned herewith, possible.

VITA

March, 1983.....Born—Angeles City, Philippines

2004.....B.S. Chemistry
University of the Philippines–Diliman

2005-2006Chemist
NCA LABS-Philippines

2006-2008Chemist and Research Associate
Environmental Engineering Graduate Program,
University of the Philippines–Diliman

2008-2010.....Graduate Teaching Assistant
Department of Chemistry
The Ohio State University

2008-2010.....Graduate Research Associate
Department of Chemistry
The Ohio State University

PUBLICATIONS

Casillas-Ituarte, N. N. Chen, X., Castada, H. and Allen, H. C. *Na⁺ and Ca²⁺ effect on the hydration and orientation of the phosphate group of DPPC at air–water and air–hydrated silica interfaces.* Journal of Physical Chemistry B. **2010**. 114 (29):9485-9495

FIELDS OF STUDY

Major Field: Chemistry

TABLE OF CONTENTS

Abstract	ii
Dedication	iv
Acknowledgments.....	v
Vita	vi
Publications	vi
Fields of study.....	vii
Table of contents.....	viii
List of Tables	xi
List of Figures	xii
Chapter 1: Introduction	1
Chapter 2: The Brewster angle microscope	5
2.1 Principles and theory of the Brewster angle microscope	5
2.1.1 The Brewster angle	5
2.1.2 Mathematical basis of the Brewster angle	7
2.1.3 Contributing factors affecting the intensity of the reflected light... ..	10
2.2 The Brewster angle microscope set-up	14
2.2.1 Components of the BAM in the Allen Laboratory	16

2.2.1.1 Goniometer	16
2.2.1.2 Light Source - He-Ne laser.....	18
2.2.1.3 Polarizer	19
2.2.1.4 Objective lens and tube lens	20
2.2.1.5 CCD camera	21
2.2.1.6 Other accessories	22
2.2.2 Image acquisition and optimization of the BAM	23
2.2.3 Image quality, image artifacts and resolution of the BAM	24
Chapter 3: Brewster angle microscopy studies of lung surfactants at the air-water interface	34
3.1 Lung surfactants	34
3.2 Experimental	42
3.3 Results and Discussion	45
3.3.1 BAM images and compression isotherms of individual lipids and fatty acid	45
3.3.2 BAM images and compression isotherms of mixed lipids and fatty acid	55
Chapter 4: Brewster angle microscopy studies of lung surfactant on physiological buffer solution.....	79
4.1 Introduction	79
4.2 Experimental	81
4.3 Results and Discussion	85

4.3.1 BAM images and compression isotherms of individual lipids and fatty acid	85
4.3.2 BAM images and compression isotherms of mixed lipids, fatty acid and peptide	90
Chapter 5: Conclusion and recommendations	111
Appendix A: Brewster angle microscopy images and surface pressure-area isotherms of other lung surfactant model systems on water subphase	114
Appendix B: Guidelines on Brewster angle microscope image acquisition using the Andor Solis software.....	121
References.....	132

LIST OF TABLES

Table 2.1 Technical data of cylindrical Helium-Neon laser head	18
Table 3.1 Biophysical properties of lung surfactant and physiological actions supported.	38

LIST OF FIGURES

Figure 2.1 Schematic diagram of polarization of reflected light on reflection from a dielectric medium.....	12
Figure 2.2 The reflectivity of a Fresnel interface between air ($n=1$) and water ($n=1.33$) for p-plane (R_p) and s-plane polarization (R_s)	13
Figure 2.3 Schematic diagram of the BAM principle.....	28
Figure 2.4 The Brewster angle microscope and KSV Langmuir Trough set-up at the Allen Laboratory.....	29
Figure 2.5 Fabrication of goniometer by Larry Antal of the Department of Chemistry Machine Shop	30
Figure 2.6 Positioning the black glass plate on the Langmuir trough	31
Figure 2.7 Image distortions in BAM Images of stage micrometer and DPPC on water using 20x infinity-corrected objective lens.....	32
Figure 2.8 Image distortions in BAM Images of stage micrometer and PA on water using 20x infinity-corrected objective lens	33
Figure 3.1 The molecular structures of DPPC, POPG and PA.....	67
Figure 3.2 Surface pressure-area isotherm of DPPC on water subphase.....	68
Figure 3.3 BAM Images of DPPC on water subphase at 24°C and total barrier compression speed rate of 5 mm/min	69

Figure 3.4 Surface pressure-area isotherm of POPG on water subphase	70
Figure 3.5 BAM Images of POPG on water subphase at 24°C and total barrier compression speed rate of 5 mm/min	71
Figure 3.6 Surface pressure-area isotherm of PA on water subphase.....	72
Figure 3.7 BAM Images of PA on water subphase at 24°C and total barrier compression speed rate of 5 mm/min.....	73
Figure 3.8 Surface pressure-area isotherm of 3:1 DPPC-POPG on water subphase	74
Figure 3.9 BAM Images of 3:1 DPPC-POPG on water subphase at 24°C and total barrier compression speed rate of 5 mm/min	75
Figure 3.10 Surface pressure-area isotherm of 9:3:1 DPPC-POPG-PA on water subphase	76
Figure 3.11 BAM Images of 9:3:1 DPPC-POPG-PA on water subphase at 24°C and total barrier compression speed rate of 5 mm/min.....	77
Figure 3.12 Surface pressure-area isotherm of 9:3:1 DPPC-POPG-PA and 3:1 DPPC- POPG on water subphase at 24°C.....	78
Figure 4.1 Surface pressure-area isotherm of DPPC on water subphase and on physiological buffer solution at 24°C	99
Figure 4.2 BAM Images of DPPC on physiological buffer subphase at 24°C and total barrier compression speed rate of 5 mm/min.....	100
Figure 4.3 Surface pressure-area isotherm of POPG on water subphase and on physiological buffer solution at 24°C	101

Figure 4.4 BAM Images of POPG on physiological buffer subphase at 24°C and total barrier compression speed rate of 5 mm/min.....	102
Figure 4.5 Surface pressure-area isotherm of PA on water subphase and on physiological buffer solution at 24°C.....	103
Figure 4.6 BAM Images of PA on physiological buffer subphase at 24°C and total barrier compression speed rate of 5 mm/min	104
Figure 4.7 Surface pressure-area isotherm of DPPC-POPG on water subphase and on physiological buffer solution at 24°C	105
Figure 4.8 BAM Images of 3:1 DPPC-POPG on physiological buffer subphase at 24°C and total barrier compression speed rate of 5 mm/min.....	106
Figure 4.9 Surface pressure-area isotherm of DPPC-POPG-PA on water subphase and on buffer solution at 24°C.....	107
Figure 4.10 BAM Images of 9:3:1 DPPC-POPG-PA on physiological buffer subphase at 24°C and total barrier compression speed rate of 5 mm/min	108
Figure 4.11 Surface pressure-area isotherms of DPPC-POPG-PA-KL ₄ (66/22/7/5 by weight ratio), DPPC-POPG-PA and DPPC-POPG on physiological buffer solution at 24°C	109
Figure 4.12 BAM Images of DPPC-POPG-PA-KL ₄ on physiological buffer subphase at 24°C and total barrier compression speed rate of 5 mm/min	110
Figure A.1 Surface pressure-area isotherm of 1:1 DPPC-PA on water subphase	115
Figure A.2 BAM Images of 1:1 DPPC-PA on water subphase at 24°C and total barrier compression speed rate of 5 mm/min	116

Figure A.3 Surface pressure-area isotherm of Tripalmitin on water subphase.....	117
Figure A.4 BAM Images of Tripalmitin on water subphase at 24°C and total barrier compression speed rate of 5 mm/min	118
Figure A.5 Surface pressure-area isotherm of 1:1 DPPC-Tripalmitin on water subphase	119
Figure A.6 BAM Images of 1:1 DPPC-Tripalmitin on water subphase at 24°C and total barrier compression speed rate of 5 mm/min.....	120
Figure B.1 Temperature control dialog box.....	122
Figure B.2 Shutter control dialog box.....	123
Figure B.3 Custom Setting dialog box of External Shutter control.....	124
Figure B.4 Setup Acquisition dialog box.....	125
Figure B.5 Imaging dialog box	126
Figure B.6 Data Type dialog box.....	127
Figure B.7 Acquisition of a Background Image	128
Figure B.8 Rescale Data Mode and Custom Mode Selection.....	129
Figure B.9 Export As dialog box	130

CHAPTER 1

INTRODUCTION

Pulmonary lung surfactants consist of complex material of lipids and proteins that line the bronchoalveolar units of the lungs. These substances are very essential for the normal functioning of the lungs as they keep the surface tension at the gas-fluid interface at a minimum.^{1,2} Pulmonary lung surfactants form a monolayer at the alveolar-air interface as they lower the surface tension at the air/liquid interface and reduce the normal air-water surface tension.^{3-10,11-13} Basically, pulmonary surfactants are fundamental for normal lung function since they provides mechanical stability especially for the prevention of atelectasis or the collapse of the alveoli during expiration.¹

A complex mixture of lipids and proteins make up the lung surfactant produced by the lung's alveolar type II cells. Composition analysis of lung surfactants reveals that lipids and phospholipids comprise most of the bulk, about 90% and the surfactant-specific proteins completes the 10% of the composition.^{2,3,14,15} Each component has various roles but altogether, they function to support the proper performance of the lungs during breathing. It has been suggested that the general function of the unsaturated lipids is to promote better adsorption rates although characterized as having poor active surface-tension lowering properties. On other hand, saturated lipids such as phosphatidylcholines,

are believed to have unusually good dynamic surface tension-reducing properties, which, is the very essence of having proper normal lung function.³

Physiologically, the critical roles of lung surfactants have been established and as such, deficiency or dysfunction of these complex systems results to life threatening disorders.^{3,11,16,17} The well-known respiratory distress syndrome (RDS), commonly affecting premature newborns, is identified to be one of the effects of lung surfactant deficiency. It is caused by insufficient supply of surfactant stores resulting in the low stability of surface tension lowering ability of the lungs. Other forms of RDS affecting both infant and adults alike include ARDS (acute respiratory distress syndrome) and ALI (acute lung injury). These forms of RDS are caused by the dysfunction of lung surfactants rather than deficiency and are related to other problems outside the lungs.

The present treatment to such diseases involves the application of effective exogenous lung surfactants, a process called surfactant replacement therapy or replacement lung surfactants (RLS).^{3,17} Effective RLS comes from animal sources. However, several critical problems including inadequate supply, viral contamination and unfavorable immunological responses among others have been identified with these sources. Such drawbacks motivate continuous studies and researches in the discovery and development of better and effective RLS.³

Monolayer experiments can be employed in studying model lung surfactants containing key components in exogenous and replacement lung surfactants.^{13,17,18,19} In general, amphiphilic molecules in monomolecular layers serve as well-defined model systems to study biological membranes and important molecular interactions of proteins

and surfactants at interfaces.²⁰ In such experiments, the physico-chemical phase behavior of surfactant monolayer can be observed and studied. Bubble surfactometer and Langmuir trough are commonly used techniques for performing experiments in monolayer surfactants and in such techniques, the surface tension of a monolayer is monitored while the available surface area is being compressed or expanded.^{9,11,13} The surface pressure-area isotherm data acquired from Langmuir trough experiments are thought to depict intermolecular forces in molecules that provide valuable data particularly in the packing of these molecules.¹⁸

Imaging techniques, such as Brewster angle microscopy and Fluorescence microscopy, can be employed along side Langmuir trough monolayer experiments.^{20,21} Unlike Fluorescence microscopy, Brewster angle microscopy does not use fluorescent dyes or probe molecules to detect inhomogeneities and domain formation in surfaces of monolayers. Fluorescent probes may perturb local environment causing the appearance of intricate artifacts that are difficult to deduce and interpret.²² Elimination of such dye is possible using Brewster angle microscopy, a technique that is very responsive to interfacial changes due to properties of phase domains in monolayers such as surface density, anisotropy and interfacial roughness and thickness.^{21,22,23}

In depth studies of monolayers usually in the air-water interface can be made using the BAM.²¹ Indeed, Brewster angle microscopy has been extensively used as a powerful imaging technique especially in the study of monolayers on liquid and solid surfaces alike since its advent in the early 20th century.²³

In this thesis, surface pressure-area isotherm experiments coupled with Brewster angle microscopy are employed in the studies of lung surfactant model systems. In Chapter 2, the theory behind Brewster angle and the principle of Brewster angle microscopy is concisely introduced. Also, the building of a BAM in the Allen lab, along with the discussion of the set-up and its individual components are discussed in Chapter 2. Additionally, the optimization and resolution of the BAM and the quality and artifacts in the images acquired using the Allen Lab Brewster angle microscope are discussed in this chapter.

Chapter 3 presents the experimental data using surface pressure-area isotherms with corresponding BAM images of individual and mixed lung surfactant model systems on water subphase at 24°C. Alternatively, the surface pressure-area isotherms and BAM images of the same lung surfactant model systems on physiological buffer solution (pH 7.0) at 24°C are described in Chapter 4.

A brief summary, conclusions and further recommendations about the studies made in this thesis are reported in Chapter 5. In the Appendices, Appendix A reports some additional data obtained from surface pressure-area isotherms and BAM images of tripalmitin, DPPC-tripalmitin and DPPC-PA mixtures on water subphase. Appendix B, on the other hand, describes a step-by-step guideline in the acquisition of images using the Allen Lab BAM operated by the Andor-Solis software.

CHAPTER 2

THE BREWSTER ANGLE MICROSCOPE

Brewster angle microscopy is a recent non-invasive imaging technique for the study of thin films on a flat surface. This imaging technique is based on the properties of light reflectivity of interfaces at Brewster angle. Currently, it is used to image films as thin as monomolecular films such as Langmuir films, which are monolayer of amphiphilic molecules at the free surface of water.^{3,24} The working principles and theory of Brewster angle microscopy will be briefly discussed in the succeeding sections and the BAM set-up built in the Allen laboratory will be presented subsequently.

2.1 Principles and Theory of the Brewster Angle Microscope

2.1.1 The Brewster Angle

Natural lighting (e.g. sunlight) and other forms of artificial illumination produce light waves whose electric field vectors vibrate in all planes that are perpendicular with respect to the direction of propagation. When light strikes a flat surface of a dielectric or insulating medium, the light is reflected and becomes partially polarized. Polarization happens when the electric vectors of the reflected light vibrate in a plane that is parallel to the surface of the material.²⁵ Figure 2.1 illustrates this light polarization phenomenon.

This light polarization phenomenon is believed to be first conceived by Sir David Brewster in the 19th century. In Brewster's light polarization experiments,^{26,27} he was able to deduce that when a beam light at a certain angle hits a reflective surface, plane-parallel polarization (single plane) of the reflected light occurs²⁵ or in mathematical terms, if the angular sum of the incident and refracted light equals $\pi/2$ this results to the linear polarization of the reflected light.²⁸ In Brewster's letter addressed to Sir Joseph Banks in 1815,²⁷ he put together these ideas and in Section 1 (On the laws of the polarisation of light, by reflexion from the first surfaces of transparent bodies) of this paper his exact Proposition I was and I quote:

“When a pencil of light is incident upon a transparent body at an angle, whose tangent is equal to the index of refraction, the reflected portion will be either wholly polarised, or the quantity of polarised light which it contains will be a maximum.”

This polarization angle is now commonly referred to as the Brewster's angle.^{25,28} Figure 2.1 also shows the Brewster angle between the incident light and the surface normal and the 90° angle between the refracted and reflected rays. In this figure, the incident light, although shown here to only have two vector vibrations, represents all other vibrations perpendicular to the propagation. The illustration suggests that the reflected ray has electric vectors oriented parallel to the surface and perpendicular to the plane of incidence. This reflectivity behavior of light at interfaces is the basis of the non-invasive imaging technique—Brewster angle microscope.^{3,24,29}

In the following section, a condensed mathematical basis of the Brewster angle will be discussed. On the other hand, general factors contributing to the reflectivity characteristics of light at Brewster angle is concisely introduced in Section 2.1.2. A more

in depth discussion of the theory of light polarization and reflectivity is available in other literatures.^{3,24,30}

2.1.2 Mathematical Basis of the Brewster Angle

Figure 2.2 shows the reflectivity of p polarization (electric field in plane of incidence) and s polarization (electric field perpendicular to the plane of incidence) between a Fresnel interface of air and water with refractive indices, n , of 1 and 1.33, respectively.^{21,24} A Fresnel interface is defined as a flat interface between two isotropic media where the refractive indices in such media changes abruptly at level $z = 0$ from n_1 ($n_{\text{incident medium}}$) to n_2 ($n_{\text{second medium}}$).²⁴

The vector compositions of light being an electromagnetic wave are the orthogonal electric and magnetic field vectors. The magnitudes of these vectors oscillate in a sinusoidal manner and the direction of propagation of light waves is perpendicular to these vectors. Typically, the direction of the electric field vector specifies the polarization angle of the light.³ As defined above, the orientation of the electric field of a p-polarized light is parallel to the plane of incidence while that of an s-polarized light, is oriented perpendicular to the plane of incidence.

For an incident p-polarized light striking an ideal interface at a Brewster angle, no reflection is produced. In a real interface, on the other hand, the reflectivity of such light is observed but only in a minimum reflectivity values as seen in Figure 2.2.^{3,21,24}

The Fresnel equations for the reflectivity of the p-polarized and s-polarized lights are given by Equations (1) and (2), respectively along with the Snell's equation in Equation (3).²⁴

$$R_P = \left(\frac{\tan(\theta_i - \theta_r)}{\tan(\theta_i + \theta_r)} \right)^2 \quad (1)$$

$$R_S = \left(\frac{\sin(\theta_i - \theta_r)}{\sin(\theta_i + \theta_r)} \right)^2 \quad (2)$$

$$n_1 \sin \theta_i = n_2 \sin \theta_r \quad (3)$$

In the equations above, θ_i is the angle of incidence, θ_r is the angle of refraction, n_1 is the refractive index of the first medium (usually air, $n = 1$) and n_2 is the refractive index of the second medium (water, $n = 1.33$). The graph of R_s in Figure 2.2 behaves in such a way that the incident angle increases from $[(n_2 - n_1)/(n_2 + n_1)]^2$ to 1. Conversely, R_p behaves differently from R_s where R_p proceeds with an abrupt decline in reflectivity and then increases to 1. The angle when R_p declines and reaches a minimum reflectivity value (ideally, 0) is called the Brewster angle (θ_B) and the condition needed in this scenario, as Equation (1) suggests, is that when the denominator, $\tan(\theta_i + \theta_r)$, reaches infinity values, or mathematically when $(\theta_i + \theta_r) = \pi/2$. Geometrically, this happens when the reflected beam becomes perpendicular to the refracted beam or when the reflected

beam makes a 90° angle with the refracted beam (Figure 2.1) as suggested by Equation (4).²⁴

$$\theta_i + \theta_r = 90^\circ \quad (4)$$

Graphically, at this angle, as the incident beam strikes the second medium (in this case, water, $n = 1.33$), the dipolar moments induced by the electric field points out in the direction of reflection and therefore these electric field do not radiate in this direction, in essence, no reflectivity is observed.^{24,31}

In simple terms, if we equate Snell's laws, Equation (3), with Equation (4), and writing θ_r in terms of θ_i , that is, $\theta_r = 90 - \theta_i$, we can isolate an incident angle, $\theta_i = \theta_B$, at which no light is reflected upon satisfying the conditions stated above.²⁵ So if we substitute $\theta_r = 90 - \theta_i$ in Equation (3) and after rearrangement, we get,

$$n_1 \sin \theta_B = n_2 \sin (90 - \theta_B) = n_2 \cos (\theta_B) \quad (5)$$

and upon further isolation and rearrangement,

$$\frac{\sin (\theta_B)}{\cos (\theta_B)} = \frac{n_2}{n_1} \quad (6)$$

$$\tan (\theta_B) = \frac{n_2}{n_1} \quad (7)$$

$$\theta_B = \arctan \left(\frac{n_2}{n_1} \right) \quad (8)$$

Essentially, Equation (8) shows that if the refractive indexes (n_1 and n_2) of the two mediums in the path of light are known, Brewster angle can easily be determined.

2.1.3 Contributing Factors Affecting the Intensity of the Reflected Light

In an ideal interface, the reflectivity of p-polarized light at the Brewster angle vanishes. On the other hand, in a real interface, the reflectivity of p-polarized light only reaches a minimum value but does not completely disappear. The origin of this discrepancy or the minimal reflected intensity at the Brewster angle strongly depends on the structure and properties of the interfacial zone. This minimum reflected intensity observed in real interface is attributed to three sources, namely, thickness and roughness of real interface and the anisotropy of monolayers. Only brief descriptions are going to be mentioned in this thesis since these origins have long been established and can be found in different literatures.^{3,22,24}

In a Fresnel interface, the refractive index changes steeply from n_1 to n_2 for $z=0$. In a real interface, on the other hand, the presence of an interfacial thickness, l , causes the refractive index to change less abruptly at $z=0$. The refractive index changes to a different $n(z)$, instead of the n_1 to n_2 transition. This difference in the refractive index, $n(z)$ over a thickness $l = 20 \text{ \AA}$, is due to the dense monolayer of amphiphilic molecules. In addition, another that contributes to the difference in the reflectivity of a p-polarized light in a real

interface is variations in reflectivities of different phase domains. These phase domains affect the $n(z)$ and the interfacial thickness, which in turn, contributes to such anomaly.

The liquid interfacial roughness, on the other hand, is due to the thermal fluctuations at the surface of the liquid or water. This roughness of the real interfaces introduces a small error on the thickness of the monolayer ($\sim 3\text{\AA}$) and hence, to the difference in the resulting reflectivity of the p-polarized light.

Third, the anisotropy of the monolayers at real interfaces significantly increases the intensity of the reflected light. Optical anisotropy is observed in concentrated phases of the monolayer and induced by the preferential orientation of non-spherical molecules in an interfacial layer. Difference in reflectivity is also observed because the reflected light becomes a function of the planar orientation of the monolayer especially if the vertical axis z of symmetry is not present in these optically anisotropic monolayers.²²

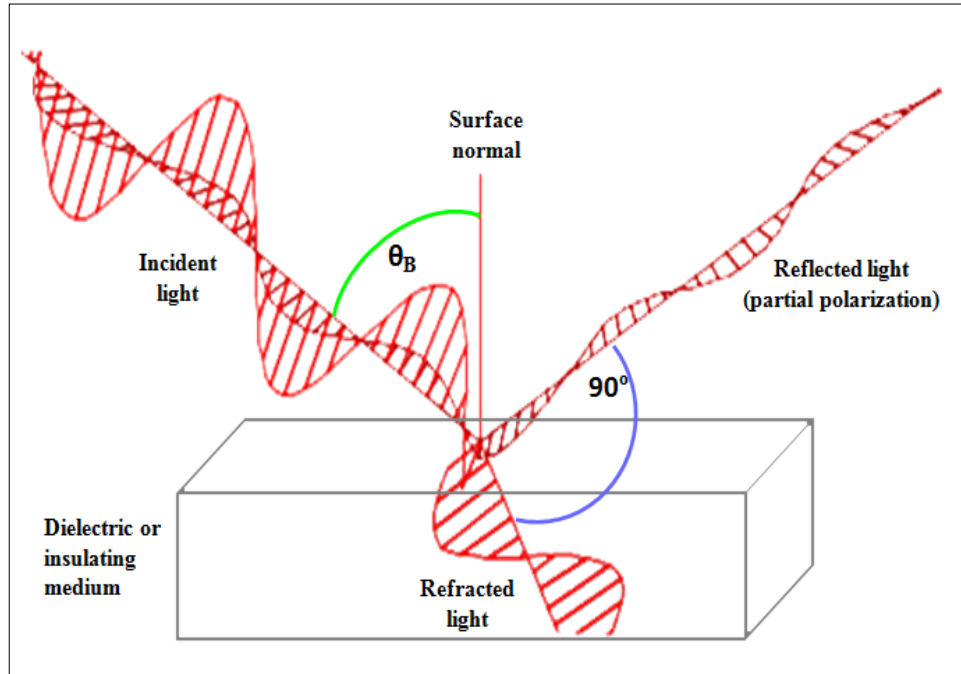


Figure 2.1 Schematic diagram of polarization of reflected light on reflection from a dielectric medium.

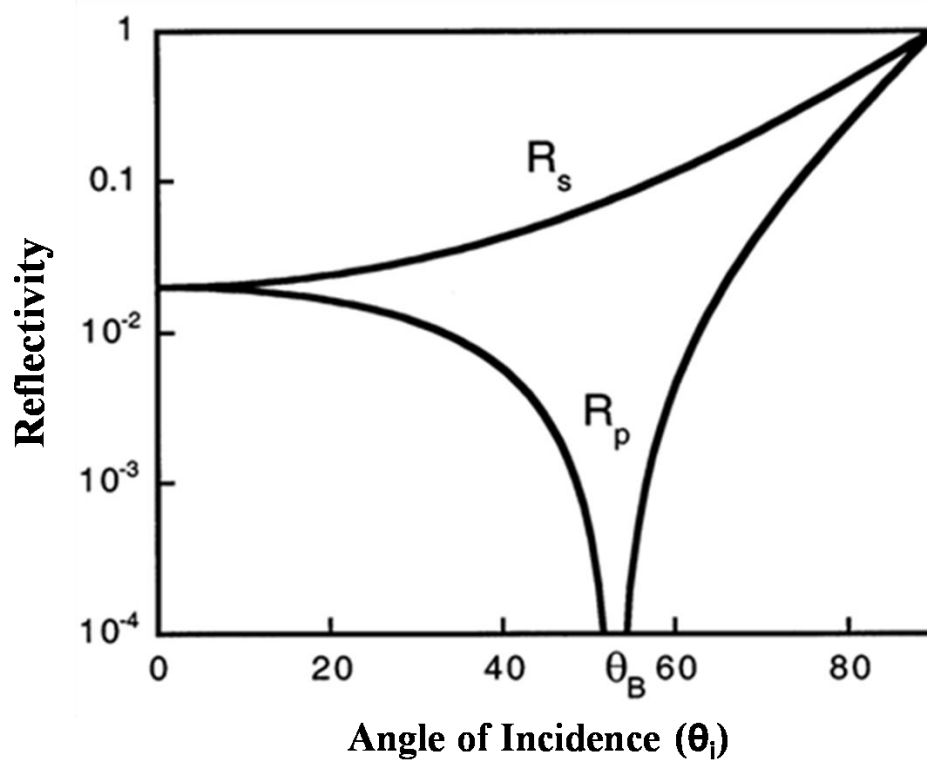


Figure 2.2 The reflectivity of a Fresnel interface between air ($n=1$) and water ($n=1.33$) for p-plane (R_p) and s-plane polarization (R_s).⁹

2.2 The Brewster Angle Microscope Set-up

The theory of Brewster angle discussed in Section 2.1 is the working principle behind the construction of a BAM. The BAM instrument uses vertically linearly polarized light (p-polarized light) as the light source, which is incident at the Brewster angle of an interface. In this configuration, a very low reflectivity results, that is, the image shows a dark background without any contrast. The incident p-polarized light at the Brewster angle, although generating minimum reflectivity, is highly sensitive to interfacial structures. This intrinsic characteristic of the BAM makes it a powerful imaging instrument able to acquire images of very thin monomolecular films such as Langmuir films and fine films at the free surface of a flat surface transparent medium like water.^{24,32} Figure 2.3 illustrates the principle in a Brewster angle microscopy set-up. In Figure 2.3a, as the vertically linearly polarized light illuminates pure water surface at the Brewster angle ($\theta_B=53.1$, $n_{\text{water}}=1.33$), no reflection is seen, that is, the image formed is a dark background without any contrast. On the other hand, Figure 2.3b presents a different picture where now, a film of monolayer is spread on the water surface and upon illumination of vertically linearly polarized light at the Brewster angle results in a reflectivity leading to formation of contrast and distinguishable figures in the image acquired.

Brewster angle microscopy is considered advantageous over other imaging instruments particularly in contrast to fluorescence microscopy.^{22,24,33} In Brewster angle microscopy experiments, apart from preventing perturbation, no impurity or fluorescent dyes are added to the film to be able to capture any contrast difference leading to image

formation. Any difference in the film's refractive index apart from the subphase can contribute to the background contrast and such film can be imaged by BAM. In addition, optical anisotropy of monolayers is believed to be more easily and directly studied using Brewster angle microscopy than polarized fluorescence microscopy since in the latter, subtle differences in transition and shifts in transition surface pressures are observed due to the presence of fluorescent impurity.^{24,34} Owing to the powerful capabilities and advantages of the BAM, it is not only proven to be an excellent tool for the characterization of surface morphologies of insoluble monolayer^{32,35} but a wide range of application have utilized Brewster angle microscopy in various research and studies such as in the field of polymer science,³⁶⁻³⁹ in biosensing,^{40,41} in biochemistry field such as studies of lipids, fatty acids and DNA⁴²⁻⁴⁸, ions, crystals and crystalline structures,⁴⁹⁻⁵¹ and many other applications.^{52,53}

A simple home-built Brewster angle microscope was constructed in the Allen laboratory. Primarily, the building of this microscope will support the different biophysics, atmospheric aerosol and geochemistry experiments in the Allen group. This section will deal with the different parts and optics used in building the microscope, the steps needed to align and optimize the instrument, the procedures used to acquire the images and a short discussion on the image quality, image artifacts and resolution of the BAM instrument. The Brewster angle microscope and KSV Langmuir trough set-up is shown in Figure 2.4.

2.2.1 Components of the BAM in the Allen Lab

The BAM set-up built in the Allen lab consists primarily of six major parts and optics: goniometer, a laser source, a polarizer, objective lens and a CCD detector for image capture. A considerable effort and care was done to be able to combine and build a functional Brewster Angle microscope capable of imaging lipid monolayer on the surface of water and on other salt solutions. The succeeding sections will describe the function and structure of each of these individual components and other additional materials in building the microscope. The procedures that are used to align and calibrate the microscope are also discussed as well as the procedures used to do experiments and capture images using the Brewster angle microscope.

2.2.1.1 Goniometer

Brewster angle microscopy is based on the properties of reflectivity of light at interfaces.^{32,33} A low intensity reflection at the Brewster angle with light polarized in the plane of incidence is highly dependent on the properties of interfaces and highly sensitive to interfacial structures.^{22,24} Moreover, the reflectivity of an interface with a p-polarized light (light polarized in the plane of incidence) at the Brewster angle is sensitive to the dielectric constant of a surface film with a monolayer thickness.³⁴ The low intensity reflection or low reflectivity at the Brewster angle, $r_p(\theta_B)$, in an air/water interface for example, can be observed directly. However, a suitable accuracy of the incident angle ($\theta_B = 53.1^\circ$ from vertical for a pure water surface)⁵⁴⁻⁵⁸ and of the polarization of the

incident light is required so that the Brewster angle, (θ_B), is not exceeded by the increase of the Fresnel reflectivity due to an error in the characteristics of the incident light.²⁴

To be able to achieve the desired angle of incident, or more specifically, the Brewster angle, θ_B , for a particular interface such as air-water surface, an instrument called a *goniometer* was fabricated. A goniometer is defined as an instrument used not only for measuring the angles of crystals⁵⁹ but also used to measure angles and allows an object to be rotated to a precise angular position.⁶⁰ A goniometer should be able to provide very good control over the angles of the incident and reflected beams.²⁹ The goniometer was constructed at the machine shop (by Larry Antal) of the Department of Chemistry at the The Ohio State University. Figure 2.5 shows a photograph of the fabricated goniometer. The design of the goniometer is described as follows. The goniometer is built with two headboards, which are both fabricated from aluminum metal. The back headboard acts as the base and major support in holding the front headboard in place where the optics, light source and all other parts are attached. The front headboard secures two arms of the goniometer. These two arms are adjustable according to the desired angle position. Mounted to these arms are breadboards to hold in place the light source (He-Ne laser) on one hand and the imaging optics on the other hand. And as mentioned, these arms can be pivoted around the reflection point so that the angle of incidence can be adjusted to the Brewster angle of the subphase used.

The goniometer has two adjusting knobs where one is located on the top of the front headboard and the other at the top of the back headboard. The adjusting knob up front is used to change the angle of incidence based on Brewster angle of the substrate

used. On the other hand, the adjusting knob positioned at the back is used to modify and correct the height or vertical position of the microscope based on the elevation of the sample stage and substrate height. In this way, it is made certain that the incident light hits the surface of the substrate and that the reflected light is captured and positioned at the center of the imaging optics. The extent of angular travel of the goniometer is from 35° to $90^\circ (\pm 0.1^\circ)$ with respect to surface normal.

2.2.1.2 Light Source – He-Ne Laser

The light source of the BAM is a visible wavelength helium-neon laser system purchased from Research Electro-Optics. The technical data⁶¹ of this cylindrical He-Ne laser is summarized in Table 2.1. The He-Ne laser is mounted using four 4-40 Unified National Course Thread holes in a fabricated frame screwed in a quarter breadboard attached to one arm of the goniometer. The laser is operated using an HCU turn-key power supply with a remote interlock operation equipped with a key switch to activate and deactivate the laser.

Table 2.1 Technical Data of Cylindrical Helium-Neon Laser Head⁶¹

Wavelength	633 nm
Minimum Output Power	17.0 mW
Polarization	Linear > 500:1
Beam Diameter	0.98 mm
Beam Divergence	0.82 mrad
Weight	840 g
Dimensions	
Length	660.4±1.0 mm (26.00±0.04")
Diameter	44.5±0.5 mm (1.75±0.02")

2.2.1.3 Polarizer

One of the basis of the BAM is that it utilizes the zero reflectance of an interface illuminated with a vertically linearly or p-polarized light introduced at the Brewster angle of incident.²⁵ A polarized light source is needed to be able to create an image contrast between the substrate background and the actual compound of interest. Thus, a polarizer is a very important component in a BAM since it can be able to generate the needed pure p-polarized light for every Brewster angle microscopy experiment.

The polarizer component of the BAM instrument is a Glan-Laser calcite polarizer purchased from Thorlabs.⁶² This Glan-Laser polarizer (GL10-A) offers an extinction ratio of 100,000:1. Extinction ratio is the defined as the relative amount of the maximum to the minimum transmittance when a polarizer is aligned to the place of polarized beam and then rotated parallel to the beam direction.³⁰ It is constructed with a laser quality natural calcite that provides low scattering of light. The polarizer has a high damage threshold value of 500 W/cm² of continuous wave power or 500 MW/cm². The prism has a dimension of 12mm x 13.7 mm (W x L) and an aperture of 10mm x 10 mm in size. The coating wavelength range of this polarizer is about 350-700 nm. The Glan-Laser polarizer is mounted on to a polarizing prism, which, on the other hand is attached to a high precision rotation mount micrometer adjustment with prism mounting hardware (PRMGL10, Thorlabs).

2.2.1.4 Objective Lens and Tube Lens

Objective lenses are believed to be the most important optical component of any light microscope as they are responsible for the primary image formation in a microscope.^{60,64,65} Objective lens also plays an important role in the determination of the quality of images produced and in the magnification and resolution of the fine details of specimen viewed under the microscope.⁶⁵

The objective lens used in the BAM set-up is an infinity-corrected Nikon CF Plan EPI lens courtesy of Dr. James Rathman of the Chemical and Biomolecular Engineering department, College of Engineering at The Ohio State University. The specifications of the objective lens are as follows: linear magnification – 20x; numerical aperture – 0.35; and working distance of 20.5 mm. Other objective lens used are 10x and 50x but the most optimized lens for the BAM set-up is the 20x objective lens. The working distance of 20.5 mm is considered as super-long working distance (SLWD) in Nikon objective lenses. This objective lens is also termed as CF or “chrome-free” objective as it is separately corrected for aberrations and needs no other optics to achieve maximum utilization.^{65,66} Also, the lens is corrected for projecting flat images rather than curved images and thus labeled as “Plan” objective lens. The objective lens is also an infinity-corrected lens. In such lenses, when light enters the objective, a flux of parallel light wave trains is produced and imaged at infinity, or in the infinity space, in which, with the help of a tube lens, is brought into focus at the intermediate plane. Infinity optical systems are very practical in terms of using auxiliary components such as polarizers, differential interference prisms (DIC), etc. into the parallel optical path between the

objective and tube lens. Such auxiliary components produce aberrations when used with the finite optical systems.⁶⁷

A second objective lens unit, termed as tube lens, is coupled with the objective lens. As mentioned, this tube lens is used to focus the parallel light beams from the objective onto the image plane. The built-in type 2nd objective lens unit is purchased from Nikon (MXA22018 CFI second lens unit tube lens element) and it is compatible with the infinity-corrected CF Plan 20 x objective lens. The tube lens has a focal length of 200 mm, typical for Nikon's infinity optical systems. The tube lens is placed 100 mm away from the objective's shoulder as directed⁶⁸ to obtain the optimal objective performance.

2.2.1.5 CCD Camera

To be able to capture the images on the surface of any subphase, a charge-coupled device (CCD) camera is used. The CCD camera was purchased from Andor Technology. The model number is DV412-BV, which is a back-illuminated-anti reflection (AR) coated CCD used for optimal performance in the visible region. It has active pixels of 512 x 512 with a pixel size of 24 x 24 (WxH) μm and an image viewing area of 12.3 x 12.3 mm. The CCD camera is operated by Andor-Solis software and CCI-010 PCI controller card with 16-bit 1MHz, 500KHz, 62KHz and 31KHz pixel readout rate options.

2.2.1.6 Other Accessories

The BAM instrument is usually operated along with other equipment such as the Langmuir trough experiment (discussed in Chapter 3). In addition, there are a few other optical and non-optical accessories employed in running a BAM. One of which is the black glass plate (BGP Nima black glass plate for MircoBAM, purchased from Biolin Scientific, Inc). The black glass plate with dimensions of 40 mm x 30 mm and 4 mm thickness is laid flat on the trough bed parallel to the incident beam path and the wedge-shaped end faces the imaging optics (Figure 2.6). In this way, the black glass plate prevents the refracted beam from reaching the imaging optics by absorbing this light from the laser source and deflecting the reflected light out of the imaging optic's path. In the same way, the glass plate also prevents diffraction of the laser beam and minimizes the scattering of light, which enhances the images acquired in BAM.⁶⁹

Another optical accessory used in the BAM set-up is a neutral density filter (CVI Melles Griot) used to attenuate the intensity of the incident beam. This filter is placed right after the laser beam exits the laser head and before the Glan-Laser polarizer (Thorlabs). On the opposite side of the goniometer, along the path of the imaging optics, stackable lens tubes are placed in between the objective lens and tube lens and between the tube lens and the CCD camera. These stackable lens tubes are believed to preserve the integrity of the reflected light beam as it travels into the objective towards the CCD camera for processing.

The entirety of Brewster angle microscope set-up and the Langmuir trough instrument are seated on an optical table to isolate vibrations from the surroundings. In

addition, this BAM-Langmuir trough set-up is completely housed inside a black-coated plexi-glass box equipped with sliding doors for easy access of the instruments.

2.2.2 Image Acquisition and Optimization of the BAM

A step-by-step guideline on image acquisition can be found on Appendix B. Image optimization is accomplished when there is a good optical and path of light alignment and this is achieved through the following guidelines.

Optical alignment. Using a gold mirror placed in the sample stage, the light emanating from the source (He-Ne laser) passing through the neutral density filter and polarizer is reflected at an angle set for the Brewster angle of the subphase used. The reflected light is then followed through and the imaging optics are carefully positioned so that reflected light hits the center of the optics. The imaging optics (objective lens and tube lens) are mounted on to separate Vernier micro-calipers to be able to fine-tune their position with respect to the path of reflected light and the CCD camera. The CCD camera is placed, as directed, to approximately 148 mm away from the back of the tube lens. This distance has been optimized and was able to give resolved images. Once the imaging optics are secured into the target positions, an image can be taken to check if the reflected light is indeed hitting the center of the imaging optics. Before taking any image, ensure that only small amount of relatively less intensity light is hitting the CCD as a powerful laser beam could damage the CCD. This can be accomplished by placing neutral density filters on the path of light to attenuate the laser beam.

Image Focusing. Image focusing is accomplished using a glass stage micrometer (purchased from Nikon) with graduated lines separated into 20 μm and 100 μm apart. The stage micrometer is placed in the sample stage holder on top of a black background. With the Brewster angle microscope in operation, images are taken and evaluated as to the clarity and resolution of the pictures. Using the fine tuning micro-caliper which can be adjusted down to 0.1 μm distance, the objective lens can be easily moved closer or farther from the sample as the distance between the tube lens and CCD is kept fixed. Using this technique, the objective lens is fine-tuned, the image is focused and the graduation lines in the stage micrometer are resolved.

2.2.3 Image Quality, Image Artifacts and Resolution of the BAM

Image quality and image artifacts. Brewster angle microscopy images are acquired at an angle because of the tilted position of all the imaging optics with respect to the path of the reflected light which is considered as an innate limitation of the BAM.²³ Owing to the inclined position of the imaging optics makes the image focal plane difficult to coincide with the surface of the subphase which results to focusing only narrow strips of the subphase.²¹ Another limitation that is important to take into consideration in a BAM set-up is the presence of parasitic background contributions that impairs the contrast, resolution and integrity of the images and imparts some artifacts in the acquired BAM images. These parasitic background contributions may result from different sources such

as interference fringes from laser light, scattered and reflected light from other optical components.^{21,23}

The Allen Brewster angle microscope is not exempted from these limitations described above. In this section, the different limitations specific to the instrument at hand will be discussed so that caution can be made especially in the interpretation of the images acquired from the BAM.

Figures 2.7 and 2.8 illustrate some of the drawbacks of the instrument with respect to the images obtained. In Figure 2.7, BAM images of a stage micrometer (the same stage micrometer used in image focusing described in Section 2.2.2) with 20 μm graduation lines and DPPC on water at 24°C (taken at LE-LC phase, 65 \AA^2 /molecule) are shown. In the BAM image of the stage micrometer, it can be seen that either ends of the lines come out to be thicker and unfocused, leaving the middle part of the lines (approximately <60 μm vertical size) focused. In the counterpart DPPC image, severe distortion (fuzziness of image) can be observed in the upper and lower regions. Different areas of the object are at different distances from the lens resulting to focusing of only narrow strips.³

Another distortion in the images acquired using the BAM at Allen Lab, is the presence of interference fringes around the domains. Figure 2.8 illustrates such distortion around the collapse domains of PA molecule in water. These fringes circling the PA domains may be due to their position with respect to the focused area of the image (as described above) and could also be due to scattered and reflected light from some optics in the BAM set-up.

Correction of images can be done digitally^{3,51} to remove some of the distortion due to the limitations mentioned above. These corrections can be done by contraction or expansion as needed of certain areas in the images,^{3,70} image filtration to reduce diffraction fringes from the laser beam and digital elimination of side ratio distortion caused by non-perpendicular line of vision of the microscope.⁷¹ Contrast in the images can also be digitally enhanced using various imaging software available. The greater distorted parts of the images in this study are removed by image cropping, and digital enhancement using the Andor Solis software is applied. Such contrast enhancement technique is also done in another study.⁷² Conversely, additional polarizers are used, which can also serve as analyzer, in improving the contrast of the images.^{54,57,73,74}

Resolution of the Brewster angle microscope. The resolution or resolving power of a microscope is defined as the smallest proximity of two objects clearly seen as two separate regions of the image.^{3,64,68} Resolution is greatly affected by the numerical aperture (NA) of the objective lens.⁶⁵ Basically, the greater the numerical aperture of the objective lens, the greater the light-gathering ability it has, and therefore an increase in resolution.^{64,65,68} The equation used to determine the resolution of the BAM is given in Equation 9.³

$$\mathbf{R = \frac{1.22 \lambda}{N.A.}} \quad \mathbf{(9)}$$

In Equation 9, R refers to the resolution or resolving power, λ is the wavelength of the source or light, and N. A. refers to the numerical aperture of the objective lens. If

Equation 9 is employed in the BAM instrument in the Allen lab and the 20 x objective lens is used with a numerical aperture of 0.35 and the laser source emits 633 nm (0.633 μm) wavelength, the resulting resolving power or the lateral resolution of the microscope is calculated to be approximately equal to 2.2 μm .

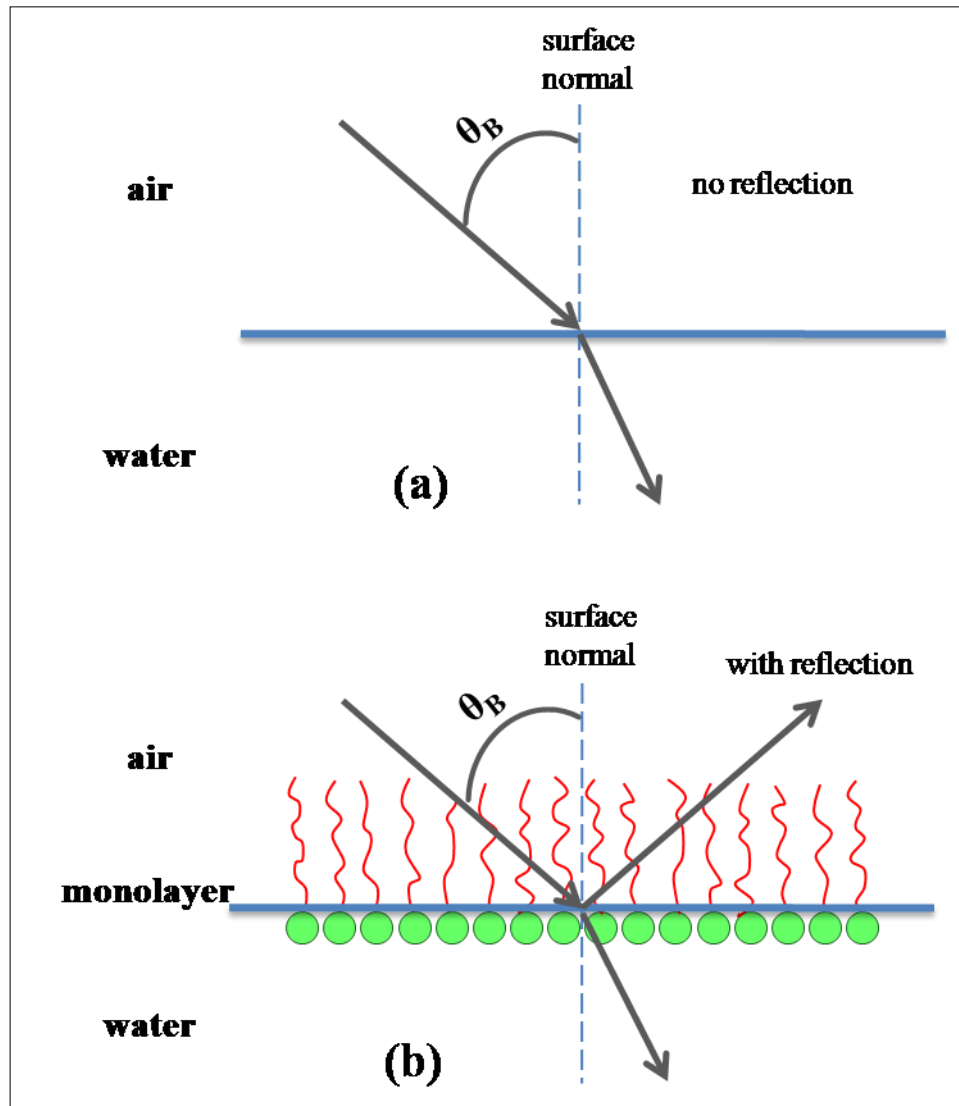


Figure 2.3 Schematic diagram of the BAM principle. In (a), water surface is illuminated with pure vertically linearly polarized light at the Brewster angle ($n_{\text{water}}=1.33$) and no light reflected. In (b), addition of monolayer film and illumination with pure vertically linearly polarized light at the Brewster angle results in reflectivity leading to contrast and image formation.

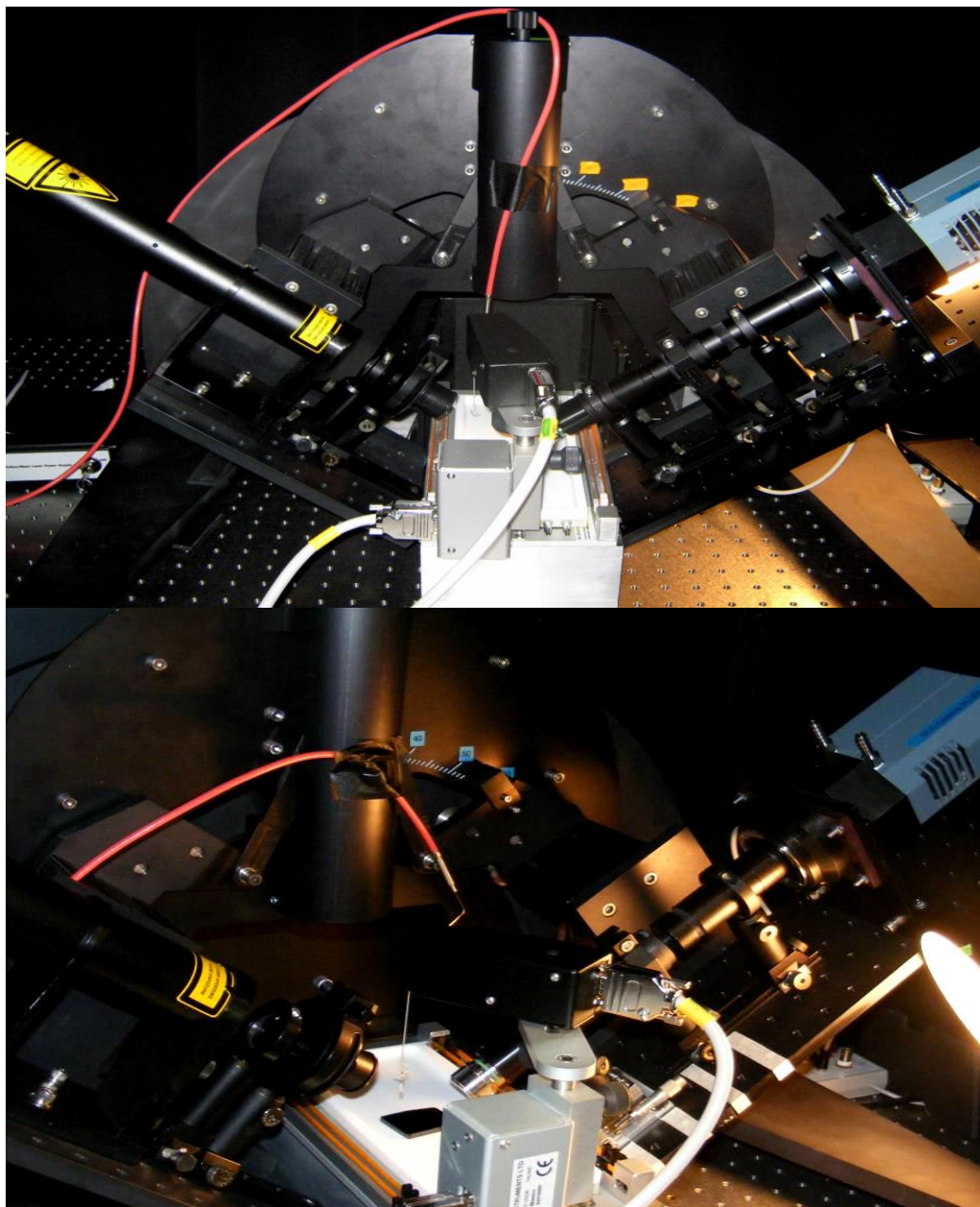


Figure 2.4 The Brewster angle microscope and KSV Langmuir Trough set-up at the Allen laboratory.

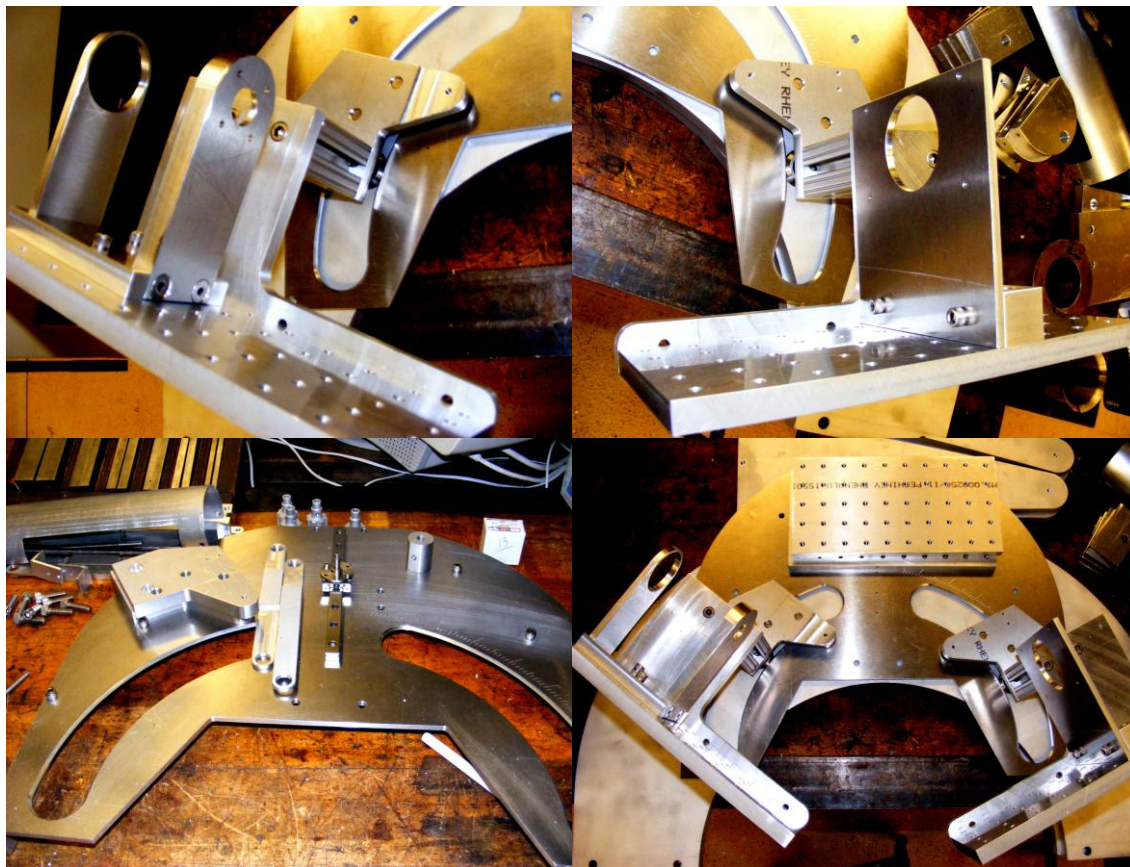


Figure 2.5 Fabrication of goniometer by Larry Antal of the Department of Chemistry Machine Shop.

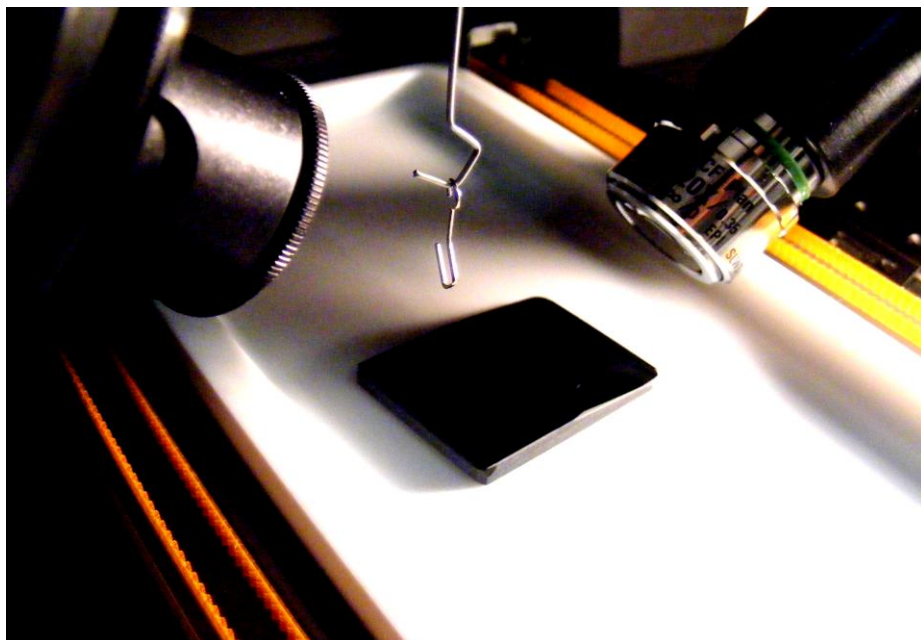


Figure 2.6 Positioning the black glass plate on the Langmuir trough.

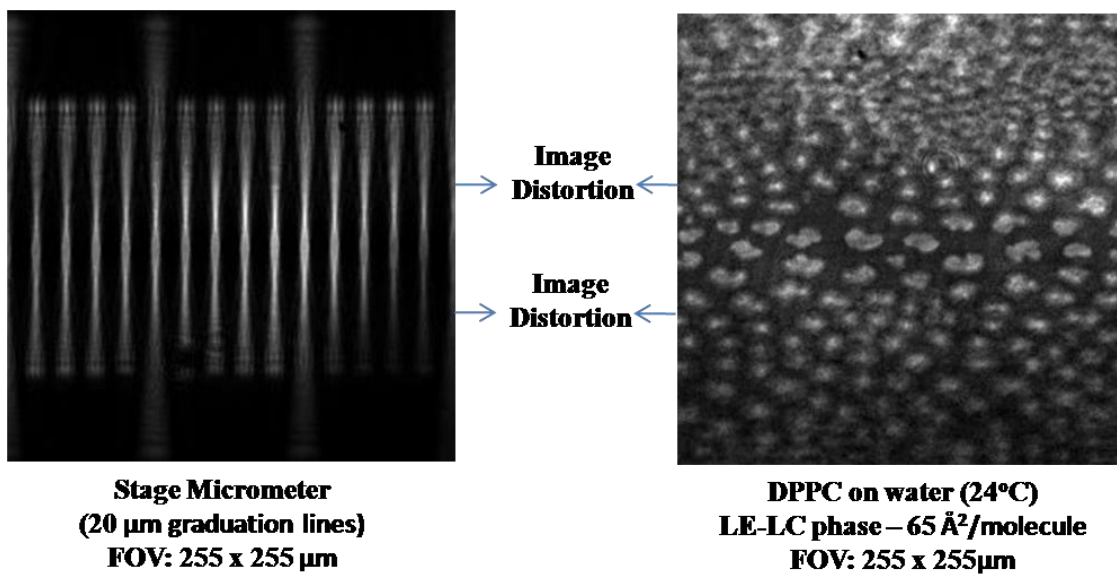


Figure 2.7 Image distortions in BAM images of stage micrometer and DPPC on water using 20x infinity-corrected objective lens.

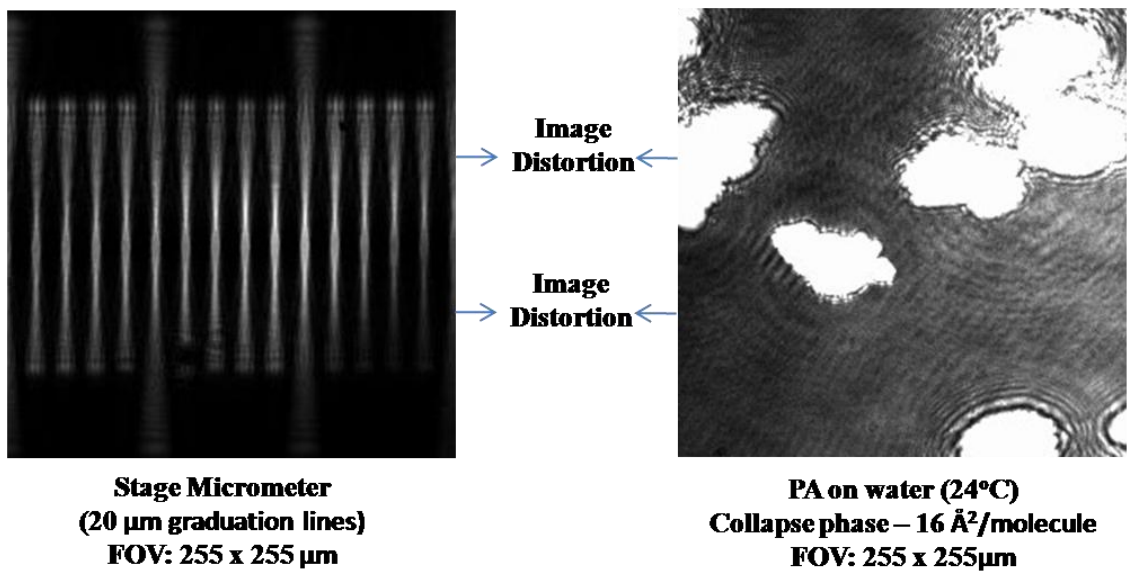


Figure 2.8 Image distortions in BAM images of stage micrometer and PA on water using 20x infinity-corrected objective lens.

CHAPTER 3

BREWSTER ANGLE MICROSCOPY STUDIES OF LUNG SURFACTANTS AT THE AIR-WATER INTERFACE

3.1 Lung Surfactants

The lung is composed of bronchoalveolar units that are lined with a complex substance, known as pulmonary surfactant, which reduces the surface tension at the fluid-gas interface and is therefore very essential for normal lung function.^{1,2} Pulmonary lung surfactant is a complex material made up of mixture of lipids and proteins. This surfactant mixture is produced in the alveolar epithelium by the type II cells and it forms a monolayer at the alveolar-air interface in the mammalian lung.³⁻⁹

The function of this lung surfactant monolayer is to either lower the surface tension at the air/liquid interface such as reducing the work load in breathing hence reducing the risk of collapse at exhalation.^{4,11-13} or reduce the normal air-water surface tension, which is brought about by lowering the interfacial tension at physiological temperature from about 70mN/m to near zero pressure during the expiration phase of the breathing cycle.^{3,10} Simply put, pulmonary surfactant is indispensable for normal lung function since it provides mechanical stability by precluding the collapse of the alveoli, also known as atelectasis, during the expiration.¹ Lung surfactant that contains lipid-rich

substances and key proteins not only functions to minimize surface tension in the alveoli but it also provides a barrier against disease.^{75,76}

3.1.1 Composition of Lung Surfactant

Alveolar type II cells in the lungs produce surfactant, specifically, extracellular surfactant. Lung surfactant is collected for composition analysis and study through bronchoalveolar lavage. Composition analysis established that lung surfactant is composed of lipid fractions and surfactant-specific protein fractions. The bulk of the lipids found in lung surfactants contain phospholipids that account for approximately 90% while the remaining 10% consists of the surfactant-specific proteins.^{2,3,14,15} In recovering surfactant in the lungs, specific lipids and their percent composition were also identified. This includes, but not limited to, cholesterol (which accounts to about 2.4% of the total surfactant composition by weight), triacylglycerol and free fatty acids.² Another identified important component of pulmonary surfactant is the plasmalogen analog of phosphatidylcholine.^{2,77} Veldhuizen and coworkers in a review article focused on the lipid composition of pulmonary surfactants.¹⁵ The most abundant lipid component analyzed in surfactant is in the form of phosphatidylcholine (PC) which makes up to about 70-80% of the total amount of lipid. Of this percentage, about 50-70% is saturated PC mostly in the dipalmitoylated form (i.e., dipalmitoylphosphatidylcholine or DPPC). The remaining percentage is made up of about ~8% anionic phosphatidylglycerol (PG), ~±5% phosphatidylethanolamine (PE), ~±3% phosphatidylinositol (PI) and present in minute quantities, about less than 2%, are phosphatidylserine (PS),

lysophosphatidylcholine and sphingomyelin.² The protein content, as stated above, is just about one-tenth of the total lung surfactant. Johansson, Curstedt and Robertson wrote a comprehensive discussion of the proteins of the surfactant system in a paper published in the European Respiratory Journal in 1994.⁷⁸ Pulmonary surfactants depend on several specific proteins for functional and structural integrity. Four proteins^{2,14,78} have been identified as components of the surfactant-specific proteins: the two large proteins SP-A and SP-D, are both hydrophilic in nature and belong to the collectin (collagen-lectin) family⁸⁰ while, on the other hand, the two other small proteins, SP-B and SP-C are very hydrophobic.^{3,79,80}

SP-A and SP-D surfactant proteins have been shown to be excluded from the monolayer form of the lung surfactant. That is, these two hydrophilic surfactants proteins are not usually mixed in clinically used replacement surfactants although they comprise about 8% of the native lung surfactant.^{3,17} However, as mentioned above, SP-A and SP-D belong structurally to the collectin family of host defense proteins and are thought to play a role in protecting the airways from bacterial or viral infection.^{3,19,83,84}

Moreover, only SP-B and SP-C are said to participate in the biophysically active monolayer form of lung surfactant. These two proteins play essential roles in commencing rapid adsorption and spreading of lung surfactant.^{3,19,83,84}

According to literature, there were recent mice experiments that were genetically modified to lack one of the four-surfactant peptides. They observed that only deficiency in SP-B resulted to a lethal mutation, which is secondary to markedly changing surfactant structure and the mutation prevented the normal development of lung tissues.³

3.1.2 Diseases of Lung Surfactant Deficiency or Dysfunction

As mentioned, because of the critical role that lung surfactant play physiologically, deficiency or even dysfunction of lung surfactants bring about lung disorders that proved to be life threatening.^{3,11,16,17} A significant number of literature exist relating to the bio-physiological importance of lung surfactant and its implications and consequences of its deficiency.^{2,9,85} Due to the vital nature of surfactant in lungs, its absence would build immense surface tension in the alveoli, which is enough to cause flooding of the air spaces by transudation leading to pulmonary edema.¹

Lung surfactant deficiency could result in respiratory distress syndrome (RDS), a disease commonly affecting premature infants. This is due to the poor development of pneumocytes (lung cells) and insufficient supply of surfactant stores among these infants resulting in abnormal surface tension lowering ability of the lungs and subsequent difficulty in respiration. Another disease caused by surfactant deficiency is known as SP-B deficiency. Whitsett and Weaver wrote a careful review article on the mechanism of this disease in 2002.⁸⁶ In this disease, a functional component of lung surfactant is absent due to the lungs' inability to produce it. This rare disease, however, is congenital in nature.

Lung diseases that can occur in both infants and adults are acute respiratory disease syndrome (ARDS) and acute lung injury (ALI). These conditions could result more from surfactant dysfunction rather than deficiency. Surfactant dysfunction in these cases could be brought about by underlying disorders and other complications outside the lungs, such as sepsis, mechanical trauma and gastric aspiration.

Although lung transplant and gene-based therapy are the only options for treatment of SP-B, most other lung diseases such as the more common RDS and ALI make use of surfactant replacement therapies. Research in this area involves the effective use and application of exogenous surfactants, which underscores the significance of better understanding surfactant properties and its interactions with critical treatment components as well as with the physio-chemistry of the lungs.¹⁷

3.1.3 Functional Requirements of Lung surfactant

Fundamental properties of an effective lung surfactant have been identified and established. Table 3.1.3 summarizes the biophysical properties of lung surfactant and the corresponding important physiological action that these properties carry out.³ These requirements, in general, are used as guidelines in supporting research and discovery to medicine and therapies to treat deficiency and repair dysfunction of lung surfactant.

Table 3.1 Biophysical properties of lung surfactant and physiological actions supported³

Biophysical Requirement	Physiological Action
Low minimum surface tension under compression	Decreased work of breathing
Variable surface tension on compression-expansion	Enhanced uniformity of alveolar recruitment
Rapid respreading of surfactant after compression past monolayer collapse	Increased alveolar stability; continuous surface tension control
Rapid adsorption to the air-water interface	Continuous surface tension control throughout breathing cycle

3.1.4 Review of Research and Studies on Lung Surfactant

A vast amount of extensive studies and research have been done and is still on going in trying to elucidate and acquire a better fundamental understanding of the different aspects of lung surfactant.^{1-11,13,16,17,73,75,76,83,85,87-89} Exhaustive but important facets in lung surfactant research include but not limited to: (i) its physiological importance (ii) the major and minor components of lung surfactant, the process by which it is transported and distributed to the alveolar/air interface (iii) the method by which it promotes alveolar stability and the role of individual components, such as the disaturated phospholipid dipalmitoylphosphatidylcholine (DPPC) in lowering the surface tension to protect the alveolus from collapsing and (iv) the numerous attempts to complement the supply of airway surfactants especially in preterm infants having deficiency of alveolar surface-active material.^{16,85,90} This last aspect open the doors in looking for replacement lung surfactant (RLS) to treat lung-related diseases such as neonatal respiratory distress syndrome (NRDS) and acute respiratory distress syndrome (ARDS).⁸⁹ In other areas of advance research, current studies on the physical properties of endogenous, commercial replacement lung surfactants and mixtures of model lung surfactants attempts to bridge the gap of the different biophysical prerequisites of lung surfactants with specific lipid/peptide mixtures, micro-scale and nano-scale structure and rheological characteristics.³ Still, more areas and aspects of lung surfactant need to be explored in different disciplines of science and engineering, medicine and clinical lung physiology.

A remarkable number of fundamental studies and research^{2,3,11,85} in lung surfactant structure and function has been done wherein many of these studies, if not all,

were motivated in establishing medicine, improvements of existing treatments and discovery of novel therapies to treat deficiency and repair dysfunction of lung surfactant that causes diseases such as ARDS and NRDS.

Furthermore, various studies on physicochemical approaches on lung surfactant monolayers have been completed such as in areas of spectroscopy such as infrared reflection-absorption spectroscopy or IRRAS,⁹⁰⁻⁹⁷ sum frequency generation spectroscopy,^{11-13,18} attenuated total reflectance-fourier transform infrared spectroscopy (ATR-FTIR),^{98,99} microscopy, fluorescence microscopy (FM),^{7,8,54,72,74,100-113} Brewster angle microscopy,^{8,72-74,100,106-108,112} atomic force microscopy (AFM),^{7,8,54,104,105,114,115} and other techniques, such as, Langmuir film balance,^{9,116-122} pulsating bubble surfactometer,^{83,123,124} captive bubble apparatus,^{83,98,123,125-129} grazing incidence X-ray diffraction (GIXD)^{73,74,130,131} and computer modeling and simulation experiments.¹³²⁻¹³⁴

3.1.5 Lung Surfactant and Langmuir Monolayers

One area in lung surfactant research that has and is still gaining a lot of interest is the study of the phase behavior of surfactant monolayers. In this aspect, it has been studied that the monolayer phase behavior *in vitro* is greatly influenced and affected by the chain length and the ratio of unsaturated to saturated chains in a surfactant mixture.^{3,135,136} Typically, performing experimental studies of phase behavior involving lung surfactant monolayers are through either employing bubble surfactometer (expanding and compressing a captive bubble) or through Langmuir trough experiments.^{9,11,13} Either technique results in the measurement of the surface tension of

rapidly expanded and compressed available surface area. In most cases, *in vitro* studies make use of Langmuir monolayers of either pure or mixture of lung surfactants.^{9,11,13,17,137} This is because the Langmuir monolayer represents an agreeable experimental model system in mimicking lung surfactant properties such as inhalation and exhalation processes in the lungs via the film's compression (respreading ability) and expansion (surface tension lowering ability) processes, respectively.^{11,13} Utilizing such technique also provides convenience in controlling certain experimental variables such as surface pressure, surface density and pH and ionic strength of the subphase.

Moreover, Langmuir film balance is a useful instrument for model studies (such as amphiphilic monolayers) because surface pressure-area (π -A) isotherms can indicate the intermolecular forces operating in two-dimensional arrangements of molecules which could be a source of information on the packing of these molecules. Characteristic differences in the transitions between the different monolayer states with increasing molecular density could be observed using this technique. These differences are brought about by variation in surface pressure, surface area and temperature.^{18,138}

There has been a large amount of biophysical research and studies with some of the major components of lung surfactant. One pressing reason is to have a better understanding of the means by which it is delivered to the air/liquid interface and promotes alveolar stability. Moreover, in these studies, several lipid components that are considered as some of the key components in exogenous lung surfactants^{13,17-19} were chosen to construct the model lung surfactant monolayers, including DPPC, palmitoyloleoylphosphatidylglycerol (POPG), and palmitic acid (PA).

As mentioned in Section 3.1.1 (Components of lung surfactant) the most abundant lipid component analyzed in native lung surfactant is in the form of saturated phosphatidylcholine (PC) and dipalmitoylated form.² This is the same reason of using DPPC as the major lipid component in synthetic lung surfactants and all replacement surfactants.¹¹ POPG represents anionic phosphatidylglycerol (PG) component in native lung surfactants (which contributes to about 8% of total lipid component). Although found at low concentrations in native surfactant, palmitic acid (PA) is an important additive in exogenous lung surfactant because of its beneficial role in replacement surfactant preparations.

This thesis focuses on the discussion of lung surfactant images obtained using the Allen-lab Brewster angle microscope and comparison of these images to BAM images and other imaging techniques, such as fluorescence microscopy studies, obtained by other researchers.^{7,9,54,73,74,100,112,139,140} Interpretation and data analysis of the lung surfactant images are discussed alongside surface-pressure area isotherm highlighting differences in sizes, shapes and phases of individual surfactant and mixtures of surfactants.

3.2 Experimental

3.2.1 Materials

The lipids used in this study were 1,2-dipalmitoyl-sn-glycero-3-phosphocholine (DPPC), 1-palmitoyl-2-oleoyl-sn-glycerol-3-phosphatidyl-glycerol (POPG) were purchased from Avanti Polar Lipids (Alabaster, AL) with >99% purity. Palmitic acid (99% purity) was purchased from Sigma-Aldrich. The molecular structures of DPPC, POPG and PA are

shown in Figure 3.1. Methanol and chloroform (spectrophotometric grades) were purchased from Fisher Scientific. Nanopure water was obtained from a Barnstead Nanopure filtration system with a resistivity of 18.3 M Ω •cm. All experiments were conducted at room temperature (23°C \pm 1°C) and at atmospheric pressure.

3.2.2 Sample Preparation

Stock solutions of DPPC and PA each with 1mM concentration were made in chloroform. Stock solution of POPG with 1mM concentration was made using chloroform/methanol mixture with 3:1 vol/vol ratio. These solutions were mixed in appropriate ratios to form model lung surfactant mixtures. The subphase used in the monolayer measurements was pure water with pH measurement of 5.5.

3.3.3 Methods

Langmuir Film Balance. Surface pressure-area isotherm studies were done in a Langmuir film balance that is equipped with a KSV minitrough (KSV, Finland, 176.5 mm x 85 mm, teflon), two barriers (coated with Delrin) to provide symmetric film compression, balance and a controller unit. Monitoring of the surface pressure and mean molecular area during film compression were done using the Wilhelmy plate method (filter paper was used to serve as the plate). Once the trough was filled with water as subphase, the barriers were closed so as to check that there is nothing in the surface that could increase the surface pressure and could make each experiment inaccurate. After this checking was done, a known amount of the sample was spread in a drop-wise manner on the water surface

using a Hamilton micro-syringe. A waiting period of ten minutes was made prior to the compression to let the organic solvent evaporate completely. Each of the barriers was compressing at a speed rate of 2.5 mm/min or 5 mm/min total compression speed rate for both barriers. All isotherms (at least before the collapsed phase region) presented were ensured to be generated reproducibly. Reproducibility was ascertained by running multiple Langmuir film balance and BAM microscopy experiments of each individual and mixed component and ensuring generated isotherms for each compound to be on top of each other (error bars are within the lines).

Brewster Angle Microscopy. The KSV Langmuir trough was equipped with the home-built Brewster angle microscope. The details of the microscope, calibration and image acquisition are written in Chapter 2 of this thesis. The BAM set-up is resting on an optical table completely enclosed in a black-coated plexiglass housing with sliding windows for easy access of the microscope (designed and assembled in the OSU Chemistry Department Machine Shop). For every Brewster angle microscopy experiment, a black glass plate (BGP Nima black glass plate for MircoBAM) was placed inside the trough before filling it with water subphase. The black glass serves to absorb the refracted beam, prevents this light from reaching the detector and enhances the captured images. The final images taken were cropped from a 512 x 512 pixel size to a 250 x 250 pixel size to show the most resolved regions of the images and were scaled using a BAM captured image of an actual stage micrometer. No other additional image processing was done with the images.

3.3 RESULTS & DISCUSSION

3.3.1 BAM Images and Compression Isotherms of Individual Lipids and Fatty Acid

The surface pressure-area isotherms (π -A or Langmuir isotherm) of DPPC, POPG, PA on pure water subphase are shown in Figures 3.2, 3.4 and 3.6 respectively at 24°C. Isotherms of surface pressure-area measurements are considered one of the usual ways to characterize the phase behavior of Langmuir monolayers. Distinct regions are noticeable in these isotherms and each region is regarded as separate phase brought about by differences in surface pressure, surface area and temperature.^{18,138} These phospholipid single-phase regions in Langmuir monolayers (as the monolayer is compressed) are described as either gaseous (G) phase, followed by a disordered liquid expanded (LE), a phase of hexatic order tilted condensed (TC, or liquid condensed, LC) and an ordered phase solid condensed (SC). Transitions from one phase to the other include the coexistence of G and LE (G-LE) and the coexistence of liquid expanded and liquid condensed (LE-LC). The characteristic plateau in these isotherms normally represents first-order transition between LE and LC phases.^{18,138,141}

Variation in morphology of monolayers corresponding to the changes in the isotherms can be imaged using the Brewster angle microscope. Local differences in the monolayer's refractive index brought about by differences in local molecular density or packing gives the contrast in the images acquired by the BAM.⁷⁴ These variations in local molecular densities or packing gives rise to changes in the refractive index of the monolayer because altogether, they contribute to the changes in the structure and

properties of the interfacial zone and therefore to the contrast of the images that the BAM can capture as explained in Section 2.1.3.

3.3.1.1 DPPC

Surface pressure-area Isotherm. The phase behavior of DPPC using Langmuir isotherms on water subphase has been well documented.^{18,135,139} The following regions have been identified upon compression (decreasing surface area) of a DPPC monolayer: a gas phase, LE phase, characteristic plateau LE-LC coexistence and pure LC phase. These regions are consistent with the DPPC isotherm result in Figure 3.2 that shows five different labeled phase regions. In this isotherm, as the monolayer is compressed the G-LE transition occurs in the first plateau in the far right of the isotherm. This G-LE transition is followed by a lift in the isotherm termed as the liquid expanded phase (occurring from 0 to about 5 mN/m surface pressure). LE phase molecules are not as free to move about as gas phase molecules and they are characterized as two-dimensional liquids.¹⁸ The characteristic plateau for DPPC, which represents the LE-LC coexistence, occurs upon further compression and around 5 to 8mN/m and between 50 Å²/molecule and 80 Å²/molecule. These results are consistent with previous studies.^{112,140,142-144} An abrupt increase in surface pressure is then observed in the isotherm, representing the liquid condensed phase where molecules are said to be in a two-dimensional semicrystalline phase.¹⁸ Upon further compression, the film collapses and this occurs around 70 mN/m surface pressure. Collapse phase structure is now in a three-dimensional form resulting from the rupture of the two-dimensional phase.¹¹

BAM Images. Phosphatidylcholines (PCs) are the primary phospholipids in the mammalian cell membrane and they are essential components of the alveolar fluid. For this reason, DPPC, being a natural PC and a focus of study, is frequently the phospholipid of choice for many monolayer studies.¹¹²

A detailed study of the domain formation in DPPC monolayers can be found in the paper of McConlogue and Vanderlick in 1997.¹¹² In their study, fluorescence microscopy was utilized primarily in probing the phase transitions in the DPPC monolayer with Brewster angle microscopy as a complimentary technique.

Figure 3.3 shows the BAM images of DPPC on the subphase of pure water at 24°C. The phase transitions of the DPPC monolayer as it progress into different stages of increasing surface pressure and decreasing mean molecular area can be observed. In the gas phase (represented by Figure 3.3 a) and at about 115 Å²/molecule, it can be seen that the surface of the water subphase is inhomogeneous with little patches of dark circular domain that have diameters from >10 µm to <100 µm in sizes. These dark circular “holes” in the monolayer are considered as disordered regions of the monolayer.⁶⁹ This observation is consistent in that the current state of the molecules as they are in the two-dimensional gas phase and are characterized by a very dilute monolayer with an area per molecule in the range of hundreds of square angstrom.¹³⁵

On compression of the monolayer, it can be observed that the water subphase has smoother, homogeneous surface characteristics observed by the disappearance of the dark circular domains. The homogeneous surface extends from the gas liquid expanded to the liquid expanded phase of DPPC as represented by Figures 3.3 b and c, respectively. This

homogeneous surface is replaced by the appearance of small white dots (Figure 3.3 d) as the isotherm approaches the phase transition LE-LC phase. In this heterogeneous surface, the LC phase appears as domains in a field of LE phase.¹¹² This domain nucleation occurs at the kink in the isotherm at around $80 \text{ \AA}^2/\text{molecule}$. Initially, the domains appear rounded and it is only as they grow that they take on their fundamental shape.¹¹² Figures 3.3 e to g shows the progression of shape formation of the DPPC through the coexistence region. In particular, Figure 3.3 f depicts some of the “bean shape” formation of the domains, which is regarded as the fundamental shape of DPPC.¹¹² The estimated sizes of these beans are about 20 \mu m lengthwise. It can be seen in this figure that these “bean shaped” domains have a distinct cavity. In McConlogue and Vandelick’s paper, it has been stated that, at higher pressure, larger beans contain larger cavities and thus accommodate a nub, which is a growth from the inside out. On the other hand, smaller beans carry with them smaller cavities where, instead of growing a nub from the inside out, the flattened edge of the bean grows into the cavity. Moving to a smaller area, represented by Figure 3.3 g, a different scenario can be seen in terms of the shape and sizes of the domains. Although the actual shapes cannot be clearly seen in this image which could be due to the limits in the resolution of the microscope, it is obvious that the domains have transitioned from the bean shape to a more spread out, multilobed domain shapes. It is interesting to note, although we will not go into deeper analysis and discussion, that a number of studies^{136,145-149} have predicted and shown through calculations and model simulations supporting the theory of shape transitions of two-dimensional monolayer domains. One model^{145,146} takes into account that the variation in

shapes of domains are established in some measure by a competition between the line tension that prefers compact and more circularly-shaped domains and the long-range electrostatic dipole-dipole repulsions of lipid molecules that favors other shapes such as elongated domains. Moreover, the shapes that could be seen in Figure 3.3 g, may or may not contain the different shapes previously named by McConlogue and Vanderlick which include mirrored S shape or mature bilobe shape, bilobe with projection, projection maturing and mature trilobed domain. In addition, the domains in this figure are approximately bigger in size than the previous, bean-shaped domains and are $> 20 \mu\text{m}$ in size. Upon compression, the LE-LC transition phase where the lipid domains are visibly changed to a homogeneous light-colored film (as represented by Figures 3.3 h to j) as opposed to the LE phase of a dark colored, homogeneous film. These BAM images along with the surface pressure-area isotherm confirm that the monolayer is now in the condensed phase and is less compressible than in the liquid expanded phase. In this phase, the hydrocarbon chains of the domains exhibit an oblique lattice with molecules tilted in a nonsymmetrical direction⁷⁴ or simply put, the condensed phase is the state of monolayer with the hydrocarbon chains aligned in contrast with the expanded state where the chains are conformationally disordered.¹³⁵ Upon further compression, the monolayer reaches a state where it cannot be compressed further without subverting its two-dimensional nature and yielding structures in the third dimensions.¹⁵⁰ Figures 3.3 k and l illustrate this state known as the collapse phase. The collapse phase is characterized by the surface pressure at the collapse, which determines the minimum surface tension for a monolayer and the collapse mechanism that establishes the respreading capability of the

monolayer upon film expansion or what is known as its reversibility. In the collapse phase, a surge in the intensity is usually observed in the images, which is secondary to the formation of multilayered aggregates at the air side of the interface.¹⁵⁰

3.3.1.2 POPG

Surface pressure-area Isotherm. Phosphatidylglycerol (PG) is one unique component of lung surfactant because this class of phospholipids is not common in mammalian cells but more typical of bacteria. Previous studies have pointed out that as a biochemical marker, PG proved to be an essential component for the maturity of the surfactant system in the developing fetus in a number of species.^{17,54}

Figure 3.4 shows the surface pressure-area isotherm of POPG. The Langmuir isotherm of POPG is very different from the surface pressure-area isotherm of DPPC. It can be observed that there is not much noticeable feature in the isotherm. It can also be noted that the signature coexistence of LE-LC in DPPC at about 5mN/m is not present in the POPG isotherm, but only a continuous curve around that surface pressure area. Although, when the surface pressure of about 42 mN/m or 43 mN/m to about 45 mN/m is reached, a relatively short plateau is observed. This plateau is interesting in that a phase transition within POPG molecules occur when they reached this certain surface pressure. Moving up to higher pressure and smaller area, small kinks can be observed (around 45-46 mN/m) and a short steady increase in surface pressure (around 47-48 mN/m) and until it reached the collapse phase (>48 mN/m).

BAM Images. Figure 3.5 a to i reveal the BAM images of POPG on water subphase at 24°C. There is no distinctive structures observable (Figures 3.5 a to e) within the resolution of the BAM during the compression of POPG monolayer from the gas phase up to about 36 Å²/molecule (represented by Figure 3.5 f). At this point, small white round patches in the surface of the monolayer appear that are about > 5 μm in sizes. Upon further compression, the sizes of these domains become bigger (Figure 3.5 g) in the plateau region of the isotherm mentioned above (isotherm of POPG). Moving up in the isotherm in the kink area, beyond the plateau region (about 45 mN/m surface pressure) we can see in the BAM image (Figure 3.5 h) that these domains are about to get closer to each other to form a homogeneous surface in the surface pressure of about 47 mN/m. In the surface pressure higher than 47 mN/m, a surge in the intensity of brightness in the image is observed which is consistent with the collapse phase seen in DPPC and other lipids and lipid mixtures.

3.3.1.3 PA

Surface pressure-area Isotherm. Palmitic acid (PA), although present at a low concentration in native surfactants, has been identified as an important additive in a number of exogenous surfactants (Survanta, Surfaxin, and recombinant SP-C surfactant) because of its beneficial role and improvement of its performance.^{12,19,54,151}

The different beneficial roles of PA have been demonstrated from various studies^{12,19} Some of these benefits have been summarized in a journal article of Ma and Allen¹² which includes: (i) the improvement of surface activity and adsorption rates of

surfactants with PA; (ii) improvement of surface activity of lung surfactant preparations; and (iii) the resistance of PA-containing surfactants to inhibitors like fibrinogen, albumin, α -globulin and lyso-PC.

PA is an essential component added to exogenous lung surfactant because for one, addition of PA results to higher solid-phase fractions and higher transition temperatures, which is secondary to the increase in the order of the DPPC-rich solid domains in monolayers.^{54,74} In addition, increase in monolayer viscosity at low surface tension^{54,74} and modification of the SP-C function⁷ are observed when PA is added to DPPC/POPG mixtures.

The observed phase transition behavior of PA in a Langmuir isotherm is shown in Figure 3.6. The isotherm trend of PA under compression follows this order of transition (going from higher molecular area to lower molecular area): gas phase (G), tilted condensed phase (TC), untilted condensed phase (UC) and then the collapse phase. This trend is consistent with previous studies. The lift in the isotherm happens at around 26 $\text{\AA}^2/\text{molecule}$ and as it traverse the TC phase, the isotherm shows a kink between the transition from TC to UC phase and this transition is said to be a second-order phase transition.^{152,153} A steep UC phase curve immediately follows this kink until it reaches a peak at about 40 mN/m which signifies that the isotherm has reached the collapse phase of the monolayer.

BAM Images. The BAM images of the PA monolayer upon compression from the gas to collapse phase are shown in Figure 3.7 a to l. Indeed, we can observe from these images

that PA molecules behave differently from DPPC and POPG monolayers as described above. The progression of the variation in sizes and shape of the PA monolayer are vivid from the gas-tilted condense (G-TC) phase up until the condense phase. At the start of compression, around $80 \text{ \AA}^2/\text{molecule}$ mean molecular area (Figure 3.7 a), small circular domains in dark background with sizes ranging from about 5 \mu m to 20 \mu m can be observed. Upon compression on smaller mean molecular area, in the G-TC phase (Figure 3.7 b and c) bigger homogeneous domains are developed. It has been described that the existence of these domains indicates two-dimensional aggregation of the monolayer thus the coexistence of the gas phase and tilted condensed in this region of the monolayer.¹⁵³ When the isotherm approached the “lift-off” region of the monolayer, at about $26 \text{ \AA}^2/\text{molecule}$, represented by Figure 3.7 d, the domains are closer and the background becomes lighter in color. Soon after further compression, homogeneous film of the PA monolayer is observed (Figures 3.7 e and f) which is consistent with the TC phase assignment in the surface pressure-area isotherms of PA (Figure 3.6). In the next succeeding images (Figure 3.7 g to l), a different darker background contrast can be observed relative to the lighter colored background in the TC phase. As mentioned above, traversing the isotherm in the TC to untilted condense (UC) phase, a kink in the curve is observed and this happens around 22 mN/m (represented by Figure 3.7 g). This kink was treated as a second-order phase transition between the two condensed regions, TC and UC, of the isotherm possessing different compressibility. In this region, the monolayer possess the same degree of translational order in both regions of the isotherm which can either be short range in the mesophases or long range in the crystalline phases depending

on the temperature. It was depicted using x-ray diffraction studies that in both phases, the hydrocarbon chains of the molecules are aligned parallel to each other in both sections of the isotherm. What makes the difference between the lower regions of the kink from the region beyond it is that the orientation of the chains in the former are either tilted with respect to the water surface or perpendicular to it. In the TC state, the monolayer is said to be relatively easily compressible and decreasing the tilt angle can be achieved through decreasing the surface area. On the other hand, in the UC state, such phases are much less compressible because there is a closed-packing between vertical molecules in which the areal density is determined.¹³⁵ Looking at the BAM images in Figures 3.7 g to i, and as what have been mentioned above, a homogeneous surface with relatively darker background contrast than the TC phase can be observed. Upon further compression, fracture collapse is observed. Fracture collapse is defined as an abrupt fracture of the monolayer and appearance of three-dimensional structure in the end of a constant rate-compression of monolayer.¹³⁵ The collapse phase BAM images of PA are shown in Figure 3.7 j to l. It can be observed that there is localization of the appearance of intensely bright patches in the images unlike the previous collapse images of DPPC and POPG where much bigger areas are involved in the collapse region.

3.3.2 BAM Images and Langmuir Isotherms of Mixed Lipids and Fatty Acid

Endogenous lung surfactant is a complex mixture of lipids and proteins. Some of the key components that serve as essential ingredients in the human lung surfactants have been identified and have become key components as well in exogenous lung surfactants. While it is very important to study the biophysical, chemical and physiological aspects of these individual components, it is of equal importance to study their behavior in mixtures to be able to gain understanding of the functions, relationship and entirety of these surfactants as a whole. As what have been pointed out by Ding et al,⁷ individual components of lung surfactant are either good at fluidizing the monolayer by proteins and unsaturated PG and PC or lowering the surface tension by DPPC particularly when mixed with PA but nonetheless, no single protein or lipid demonstrate both properties.

Monolayers of uniform mixtures in the whole concentration range are possible and this is secondary to the miscibility of various amphiphiles. Characterization of the phases of one substance to the other can be done by gradually changing the concentration of the components and studying the phase diagram of mixtures.¹³⁵

Monomolecular films containing more than one film-forming chemical component are termed as mixed Langmuir monolayers. Such monolayers are used as excellent model systems in elucidating the intermolecular interactions in a definite two-dimensional environment.¹² Mixtures of the individual lipids of DPPC, PA and POPG, lung surfactant proteins and other lipids and proteins have been done in past studies^{11-13,54,74,100,130} employing different techniques. A similar mixture of the three different lipids, DPPC, POPG and PA is done in this study using Brewster angle microscopy

coupled with surface-pressure area isotherms. Each of these lipids is mixed in appropriate ratios of 3:1 DPPC-POPG and 9:3:1 DPPC-POPG-PA combination. These formula mixtures (in smaller ratios) are close functional mimic to natural lung surfactants both in vitro and in vivo and are abstracted from the lung surfactant mixture with a formula of 66/22/7/5 DPPC-POPG-PA-KL₄ by weight used in previous studies.^{11,13,76,154} This formula mixture of lung surfactant with KL₄ peptide, along with the mixtures of lipids and fatty acid, is studied in chapter 4.

Due to extraction difficulties and in the number and type of additives used, the makeup of native surfactants changes significantly from one species to another species and consequently, the structure and composition of replacement surfactants vary particularly.^{7,54,151} In essence, no universally accepted surfactant composition has been formulated.⁷

3.3.2.1 DPPC – POPG mixture

Unsaturated and anionic component in endogenous and exogenous lung surfactants, such as POPG, improve the respreading and adsorption properties of DPPC.^{11,15,17} One of the requirements to a suitable and functional lung surfactant is to have a balance between the saturated rigid components such as DPPC and PA and the unsaturated and anionic components such as POPG.^{11,17} POPG forms fluid films at room and body temperature and has fluidizing effect on DPPC because of its own fluid nature that is contrary to the condensing effect of PA.^{11,74} This fluidizing effect of POPG is an interfacial disordering effect on the molecules within the film or a conformational

disordering influence on the DPPC chains when DPPC is in the LE phase. Also, it is said that when DPPC is in the LC phase, POPG has no effect on the conformational ordering of the DPPC chains.¹¹

Surface pressure-area Isotherm. Figure 3.8 shows the surface pressure area-isotherm of 3:1 DPPC-POPG on water subphase. Looking at this isotherm and comparing it to the DPPC and POPG isotherms as previously described (section 3.3.1.1 and 3.3.1.2 respectively), the lower half of the isotherm behaves like POPG (with no features but plain looking curve with a gradual increase in surface pressure upon compression) and the upper half behaves like DPPC in that it reaches <70 mN/m on collapse. As can be observed, the isotherm of this mixture lacks the pronounced plateau in the 5 mN/m surface pressure as observed in DPPC isotherm and the short plateau observed in POPG isotherm (42mN/m). Nevertheless, a careful examination of this mixture's isotherm, the isotherm shows a "lift-off" at around 100 mN/m . Also, a kink or plateau-like curve which happens around 13 mN/m or $70 \text{ \AA}^2/\text{molecule}$ to around 21 mN/m or $55 \text{ \AA}^2/\text{molecule}$ can be observed although indistinctly. This kink is also observed by Bringezu et al⁷⁴ and they referred to it as "smeared-out plateau". The curve, after this "smeared-out" plateau, in the high surface pressure region, above 30 mN/m, the curve is relatively steeper up to a collapse pressure of 66 mN/m to 71 mN/m.

BAM Images. The BAM images of the mixed DPPC-POPG monolayer (with 3:1 DPPC-POPG mixture ratio) starts with dark circular domains with sizes to about $>20 \mu\text{m}$ and

<50 μm in a white homogeneous background (Figure 3.9 a and b). These dark circular domains decrease in size upon further compression and the white homogeneous background dominates the area of the image as appeared in Figure 3.9 c. This figure also corresponds to the lift-off region of the isotherm in Figure 3.8 at 100 $\text{\AA}^2/\text{molecule}$. At about 5 mN/m to 13 mN/m surface pressure (depicted by Figure 3.9 d), the BAM image appears as dark gray without any contrast and observable shapes or domains present indicating a homogeneous liquid expanded phase. On compression at lower mean molecular area (Figure 3.9 e, 70 $\text{\AA}^2/\text{molecule}$ and 13 mN/m), very minute white spots can be observed and as compression progresses, the monolayer demonstrates appearance of bright condensed phase domains in a continuous background of darker liquid expanded phase (Figure 3.9 f to g). In these figures, taken at 19 mN/m to about 21 mN/m, the sizes of the bright condensed phase domains increases from about 1 μm at the onset of these domains to about 10 μm . As the monolayer is further compressed in Figure 3.9 h, i and j, a decrease in contrast of the images and increase in intensity of brightness of the monolayer are observed. The same outcomes were observed in previous study⁷⁴ and it was reported that this loss in contrast in these regions of surface pressure indicates an almost complete conversion to a condense phase with uniform molecular orientation. Upon reaching higher surface pressure (> 65 mN/m), it can be seen that a much more increase in the contrast is noticed accompanied by formation of very intense, small (approximately 10 μm) domains. The shape of these domains is indistinguishable as the resolution of the BAM is limited for the image to be resolved.

3.3.2.2 DPPC – POPG – PA mixture

Surface pressure-area Isotherm. In a study made by Bringezu et al⁷⁴ in 2001, they followed the changes in behavior of the surface pressure-area isotherm of DPPC-POPG (with a constant ratio of 77/23 w/w) with additions of PA from 0 %-80% additions BAM images. In this study, it was observed that the addition of PA considerably changed the isotherm. Specifically, the following observations were made: (i) addition of PA shifts the lift-off pressure toward lower areas per chain; (ii) increasing the PA fractions up to 40% systematically lowers the collapse pressures; (iii) systematic increase of the slope of the isotherm (increase in slope is proportional to the compressibility of the monolayer) with increasing PA fraction; (iv) shift of the plateau region toward higher pressure (with 10% PA) corresponding to an increase of the transition temperature of the monolayer; (v) at higher PA fractions (>20% PA), the “smear-out” plateau in the isotherm completely disappear; and; (vi) adding PA at constant surface pressure leads to a more condensed monolayer packing at low surface pressure.

In 2003, Ding et al⁵⁴ studied the same set of lipid and fatty acid component. This time, the concentration of PA was held constant at varying DPPC-POPG mixing ratio. The mixing ratio started from a 1:1 (45:45 w/w) concentration of DPPC-POPG and the succeeding mixtures were made by increasing the concentration of DPPC by 11% by weight while decreasing the concentration of POPG by the same amount. The following summarizes their results: (i) lower fractions of POPG (13%-38% POPG relative to DPPC) gave higher collapse pressures of about 68 mN/m while at higher POPG concentrations, reduction of collapse pressure is observed (at 100% POPG, collapse

pressure is about 62 mN/m) and; (ii) appearance of short-lived kink at the highest POPG concentration (48 mN/m) and likely corresponds to partial removal or squeeze out of POPG.

Figure 3.10 illustrates the surface pressure-area isotherm of 9:3:1 DPPC-POPG-PA mixture ratio on water subphase at 24°C. In this figure, it can be deduced that the isotherms lifts off at around 90 Å²/molecule and the curve continues to rise up with increasing surface pressure and upon compression (decreasing area). From the lift-off point upon further compression, a kink in the isotherm can be observed and it occurs at around 82 Å²/molecule or about 2.8 mN/m pressure. This kink smears out gradually as the surface pressure increases steadily with small increments. The isotherm steadily rises relatively steeply after this kink and reaches a collapse pressure above 67 mN/m. This observation is consistent with Bringezu et al⁷⁴ result in that increasing the PA fractions up to 40% systematically lowers the collapse pressure and Ding et al⁵⁴ result where lower fractions of POPG (13%-38% POPG relative to DPPC) gave higher collapse pressures of about 68 mN/m. In this study, the mixture of DPPC-POPG-PA has about 23% POPG and 7.7 % PA. Also, in comparing the isotherm of 3:1DPPC-POPG (Figure 3.58) versus 9:3:1 DPPC-POPG-PA (Figure 3.6) mixtures, it can be observed that there is a shift in the “lift-off” pressure toward lower molecular area upon addition of PA which is also consistent with Bringezu et al results.

BAM Images. At the onset of the isotherm of DPPC-POPG-PA mixture, at around 120 Å²/molecule and 100 Å²/molecule (Figure 3.11 a and b), it can be observed that circular

domains can be noticed having diameters ranging from 30 μm to 70 μm . Like the circular holes describe in the monolayer of DPPC, these holes can be also considered as disordered regions of the mixed monolayer.⁶⁹ Further compression of the mixture's isotherm (Figure 3.10), in the lift-off point at around 90 $\text{\AA}^2/\text{molecule}$ and towards the slope at 85 $\text{\AA}^2/\text{molecule}$, the BAM images reveal a homogeneous surface of dark background contrast (Figure 3.11 c and d) which is consistent with the characteristics in liquid expanded phases. In this mixture, it can be observed that the coexistence region is shifted toward lower pressures when PA is added in DPPC-POPG mixture as opposed to the DPPC-POPG mixture alone. This result, which is consistent with other studies,⁷⁴ is demonstrated through Figure 3.12 and the BAM images of the lipid-fatty acid mixture in Figure 3.11. In the BAM image (Figure 3.11 e) as early as about 2.8 mN/m surface pressure, small domains of about 10 μm in sizes already appear. These domains grow in size to about >40 μm as the area is decreased and surface pressure is increased (Figure 3.11 f to j). The domain shapes are interesting as they develop in size because they are no longer circular but transformed into branched domains. These branched domains are termed as fractal-like shape domains that are also seen in DPME monolayers.^{31,155} In this fractal-like shape growth pattern, the growing tips are not associated to the crystallographic directions of the two-dimensional lattice; hence, these domain shapes do not reflect the chirality of the crystal lattice.¹⁵⁵ Further compression results in the loss of contrast in the BAM images (Figure 3.11 k to l) and an intense brightness is observed consistent with the collapse phase BAM images of previous samples. This transition towards loss of contrast indicates uniform orientation of the molecules in the monolayer

and can be observed earlier in the monolayer if a higher concentration of PA is added in the DPPC-POPG mixtures.⁷⁴ These BAM observations along with the surface pressure-area isotherm and other studies indeed show PA induces a condensing effect of the monolayer.

In summary, the surface pressure-area and Brewster angle microscopy images of individual and mixed model lung surfactant systems of containing DPPC, POPG and PA were presented and discussed above. For the individual lipid at fatty acids, the surface pressure-area isotherm and BAM images of DPPC agree with what has been reported in other literature.^{112,140,142-144} The generally agreed various phase transitions of DPPC were demonstrated in Figure 3.2. Likewise, the signature LE-LC phase coexistence of DPPC isotherms, that occurs around 5 mN/m to 8 mN/m also agreed with previous studies. The bean-shaped characteristics of DPPC were also clearly seen in the BAM images presented along with their distinct cavity that accommodates either a nub or a growth from inside out as discussed by McConlogue and Vanderlick.¹¹² Multi-lobed domains can be also be observed but their shapes are indistinguishable due to the limitation in the resolution of the BAM.

POPG demonstrated features in the isotherm only in the higher surface pressure and it showed a short plateau at surface pressures of about 42 mN/m to 45 mN/m and kink at about 46 mN/m. The plateau and kink formed by POPG in higher surface pressure are interesting because it is in these surface pressures that the short-lived POPG domains were seen in the BAM images.

The resulting PA isotherm is also agreeable with the previous studies.^{152,153} Unlike DPPC and POPG, the observed BAM images of PA domains are vivid as the isotherm progresses from spreading to the collapse phase. The different phases in the isotherm of PA are represented correspondingly with the BAM images. Localization of the intensely bright domains is observed in the fracture collapse of PA.

Individual components of lung surfactant are either good at fluidizing the monolayer by proteins and unsaturated PG and PC or lowering the surface tension by DPPC particularly when mixed with PA but nonetheless, no single protein or lipid demonstrate both properties.⁷

The surface pressure area-isotherm of 3:1 DPPC-POPG behaves like POPG in the lower half of the isotherm and the upper half behaves like DPPC in that it reaches <70 mN/m on collapse. A kink or plateau-like curve, called smeared-out plateau occurs at around 13 mN/m where appearance of small white spots later turning to bright-condensed phase domains in a continuous background of darker LE phase is seen. As the monolayer is further compressed a decrease in contrast of the images as the brightness of the monolayer intensifies indicative of complete conversion to a condense phase with uniform molecular orientation. Bringezu et al⁷⁴ observe the same phenomenon.

In the case of the ternary mixture of 9:3:1 DPPC-POPG-PA, it was observed that a kink in the isotherm ($82 \text{ \AA}^2/\text{molecule}$) that smears out gradually upon compression occurs. The isotherm steadily rises and reaches a collapse pressure above 67 mN/m. These results are consistent with Bringezu et al⁷⁴ and Ding et al data. In the former, increasing the PA fractions up to 40% lowers the collapse surface pressure where as in

the latter, lower fractions of POPG (13%-38% POPG relative to DPPC) gave higher collapse pressures of about 68 mN/m. In this mixture, it can be observed that the coexistence region is shifted toward lower pressures when PA is added in DPPC-POPG mixture as opposed to the DPPC-POPG mixture alone. BAM images showed interesting development of domains from circular to fractal-like branches also seen in DPME monolayer.^{31,155} Further compression results in the loss of contrast in the BAM images indicating uniform orientation of the molecules in the monolayer.

The surface pressure-area isotherms and BAM experiments not only showed the behavior of individual representative lipid and fatty acid component found in endogenous and exogenous lung surfactants but also their effect in when mixed to form model lung surfactant monolayers. The data above showed consistent results as with other studies.^{54,74} Although native surfactants contain multifaceted components, these simple mixtures of lipids can be used to study the lipid-lipid and other important interactions and physicochemical properties (i. e., surface tension) found in natural and replacement lung surfactants.^{74,83,151} The physic-chemical behavior of individual lipids are important to study since they are the structural basis of these endogenous and exogenous lung surfactant but equally important to study is the multiple lipid and protein mixtures because of the complex requirements of lung surfactants mentioned above. In the case of DPPC, although found to be the most abundant lipid in natural lung surfactants² and can solely provide high surface pressure (> 70 mN/m, as suggested in the results above) on compression or in the context of the function of the lungs, the necessary low surface tension upon exhalation, DPPC on its own suffers difficulty in rapid re-spreading or

adsorption after expansion (or inhalation) to cover the new interface for re-compression-expansion cycle (dynamic cycle of exhalation and inhalation).^{54,74}

On the other hand, POPG, which represents, the unsaturated phospholipids and hydrophobic proteins in native surfactants, is thought to augment some limitations of the DPPC for improved lung surfactant. In the BAM study at hand, analysis of the POPG images in Figure 3.5 implies that POPG molecules relatively remains as liquid expanded phase in a quite an extended span of mean molecular area until about $36 \text{ \AA}^2/\text{molecule}$ where the liquid condensed domains are first seen to form. Likewise, the BAM images of DPPC-POPG mixture suggests that the emergence of the condensed domains are delayed ($\sim 60 \text{ \AA}^2/\text{molecule}$), which would normally form at around $80 \text{ \AA}^2/\text{molecule}$ in the DPPC monolayer seen in Figure 3.3. This is not surprising, as POPG is believed to impart fluidizing effect (as opposed to the condensing of PA) to lung surfactant mixtures^{11,54} and thus non-condensable fluid phase at all surface pressure and temperatures.⁷⁴ This fluidizing effect of POPG is an interfacial disordering effect on the molecules within the film or a conformational disordering influence on the DPPC chains when DPPC is in the LE phase.¹¹ Ding and co-workers also observed such fluidizing effect where the condensed-phase domain size generally decreases as the POPG fraction increases on several DPPC-POPG-PA and DPPC-POPG-PA-dSP-B₁₋₂₅ mixtures.⁷⁴

Opposite to the effect of POPG, it is generally agreed that PA has condensing effect on monolayer mixtures.^{11,12,74} The same observation is seen in the results of this study because of the shifting of the isotherm of DPPC-POPG when PA is added and as seen in the BAM, the onset of condensed phase domains that occur earlier in the ternary

mixture than the mixture of DPPC-POPG alone. This condensing effect is also observed in other binary studies of DPPC and hexadecanol.⁵⁶ This condensing effect of PA is viewed as a positive effect in the physicochemical characteristics of DPPC-POPG mixed films at the air-water interface in such a way that the PA facilitates the close-packing, upright orientation. It is suggested by Brinquez and co-workers⁷⁴ that this PA effect, which imparts changes in the short-range ordering of condensed domains, contributes to the enhanced performance of lung surfactant replacements.

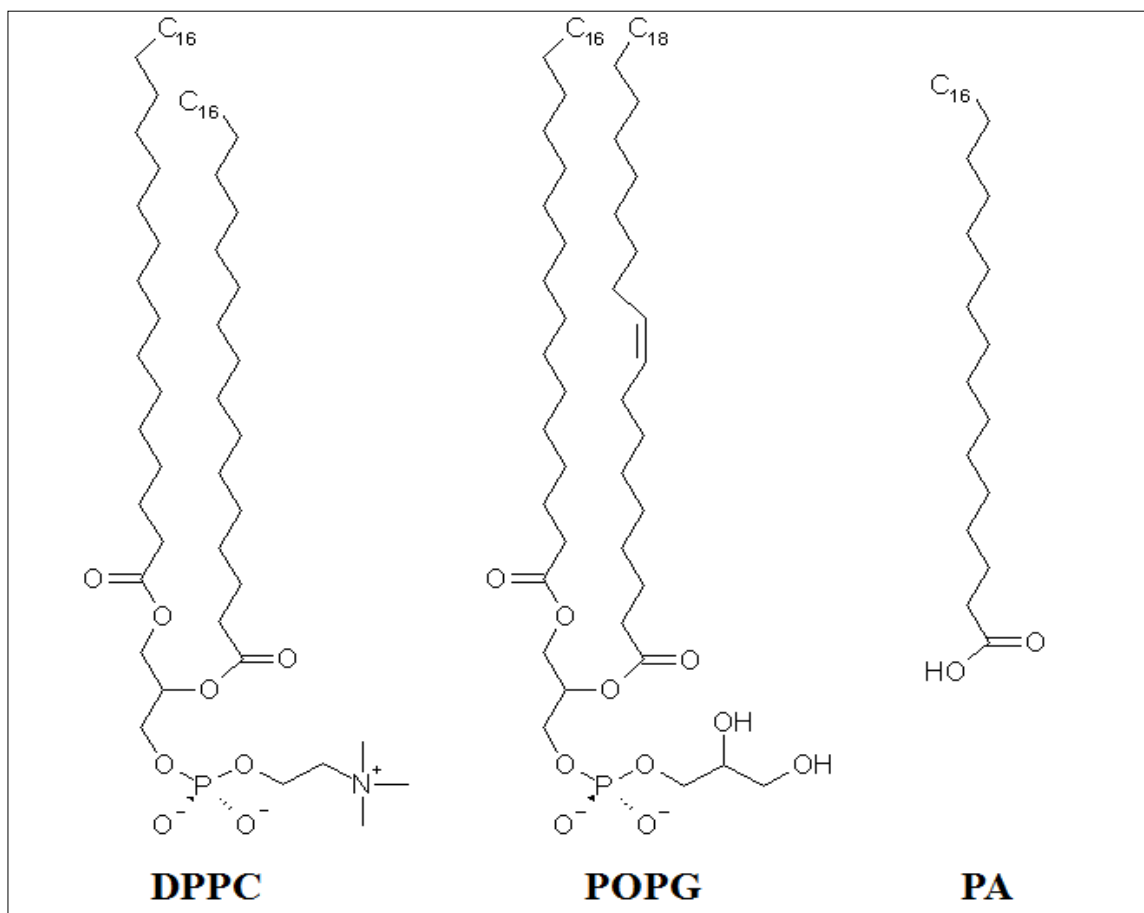


Figure 3.1 The molecular structures of DPPC, POPG and PA.

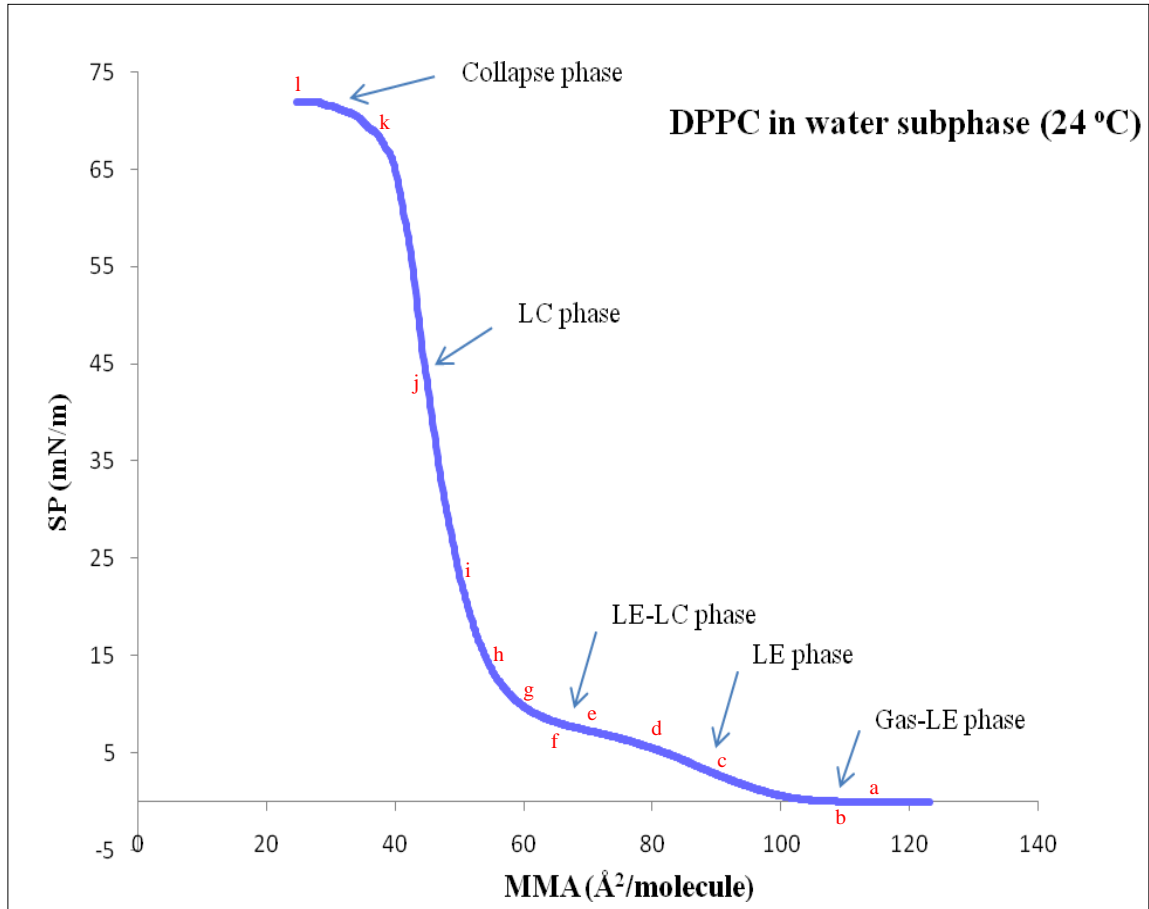


Figure 3.2 Surface pressure-area isotherm of DPPC on water subphase.

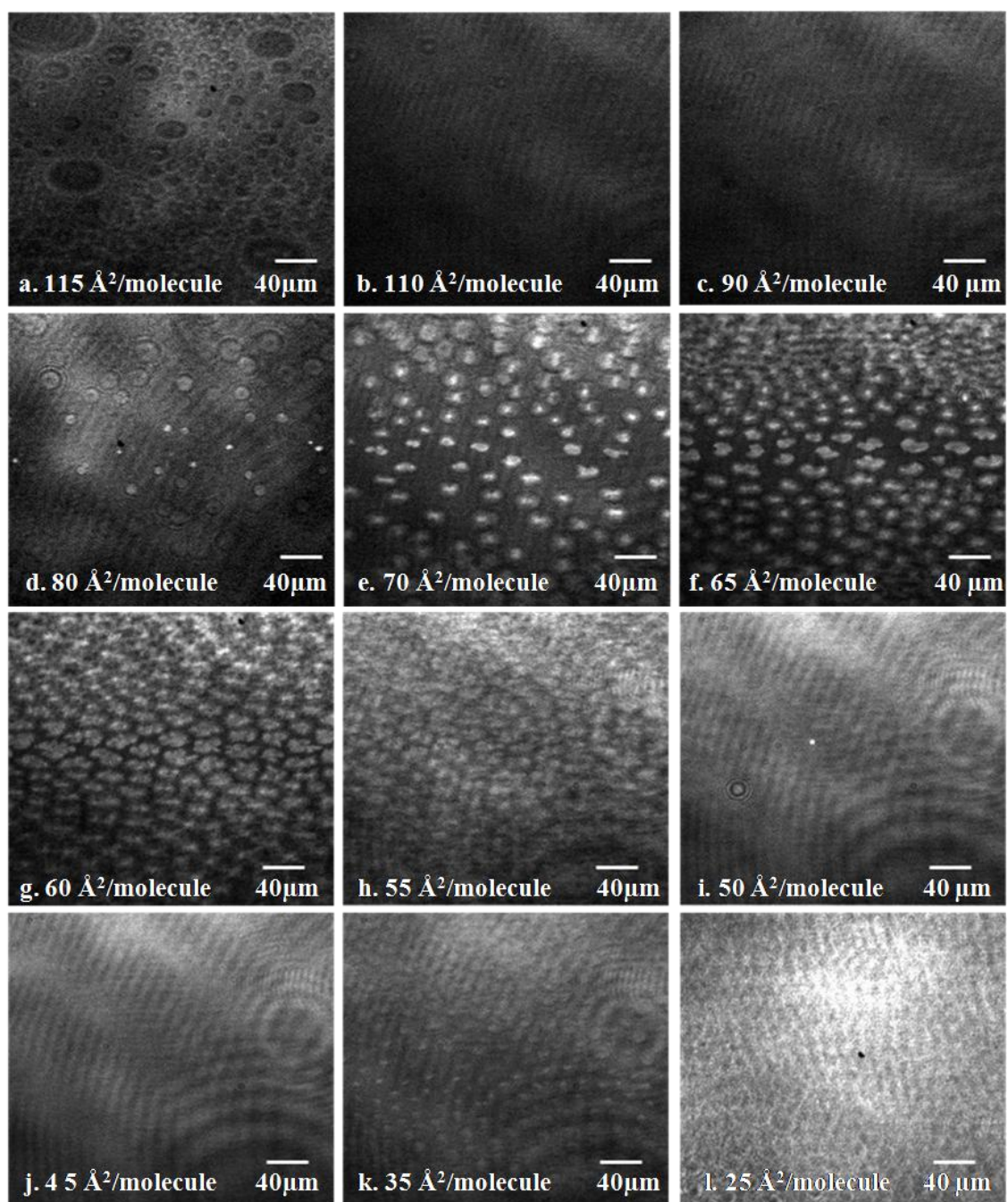


Figure 3.3 BAM Images of DPPC on water subphase at 24°C and total barrier compression speed rate of 5 mm/min.

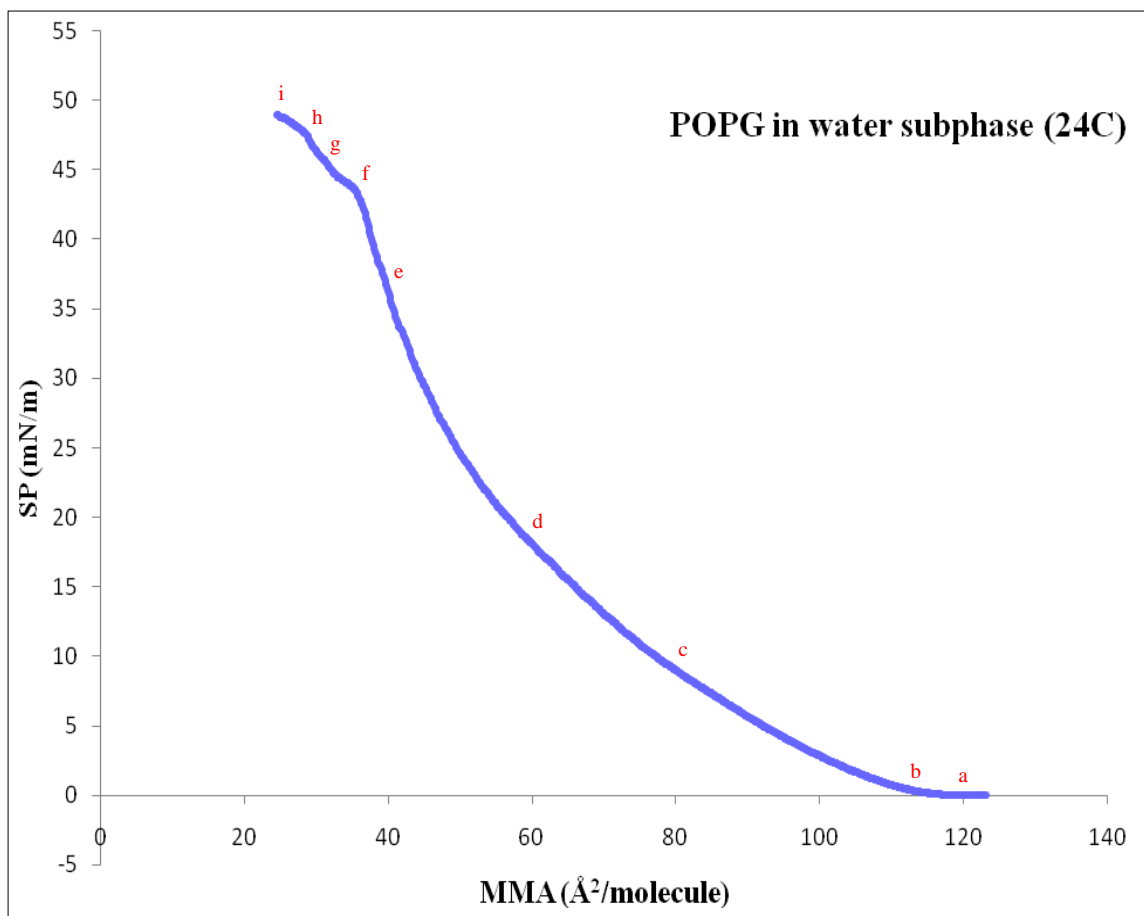


Figure 3.4 Surface pressure-area isotherm of POPG on water subphase.

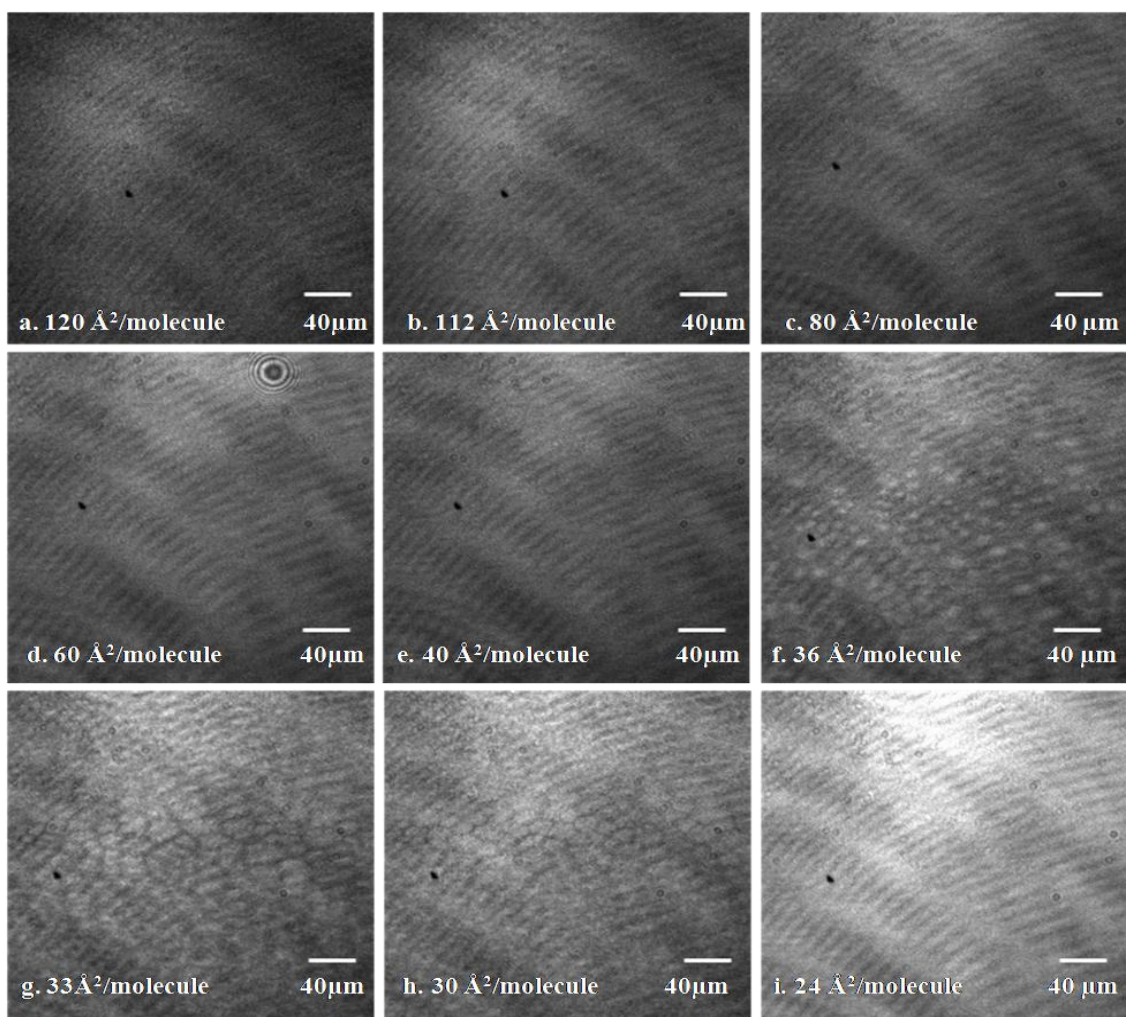


Figure 3.5 BAM Images of POPG on water subphase at 24°C and total barrier compression speed rate of 5 mm/min.

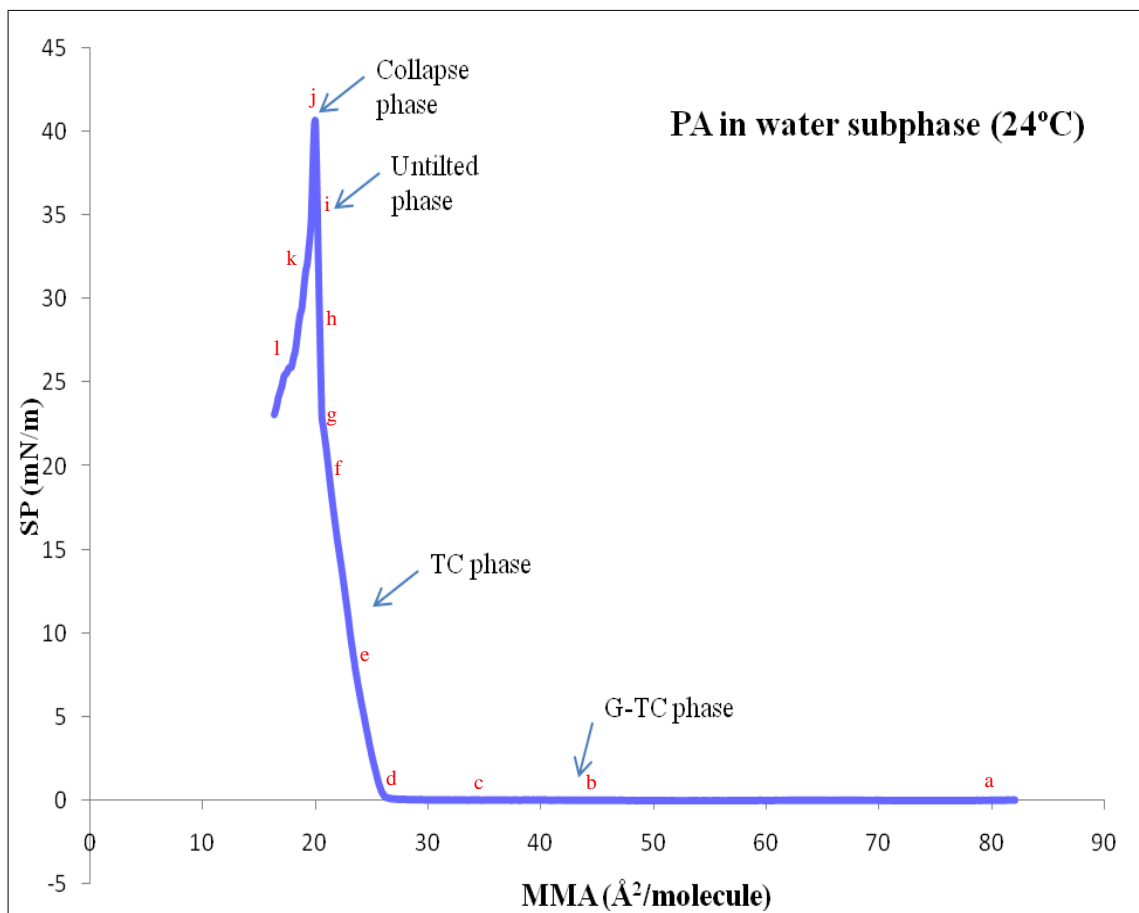


Figure 3.6 Surface pressure-area isotherm of PA on water subphase.

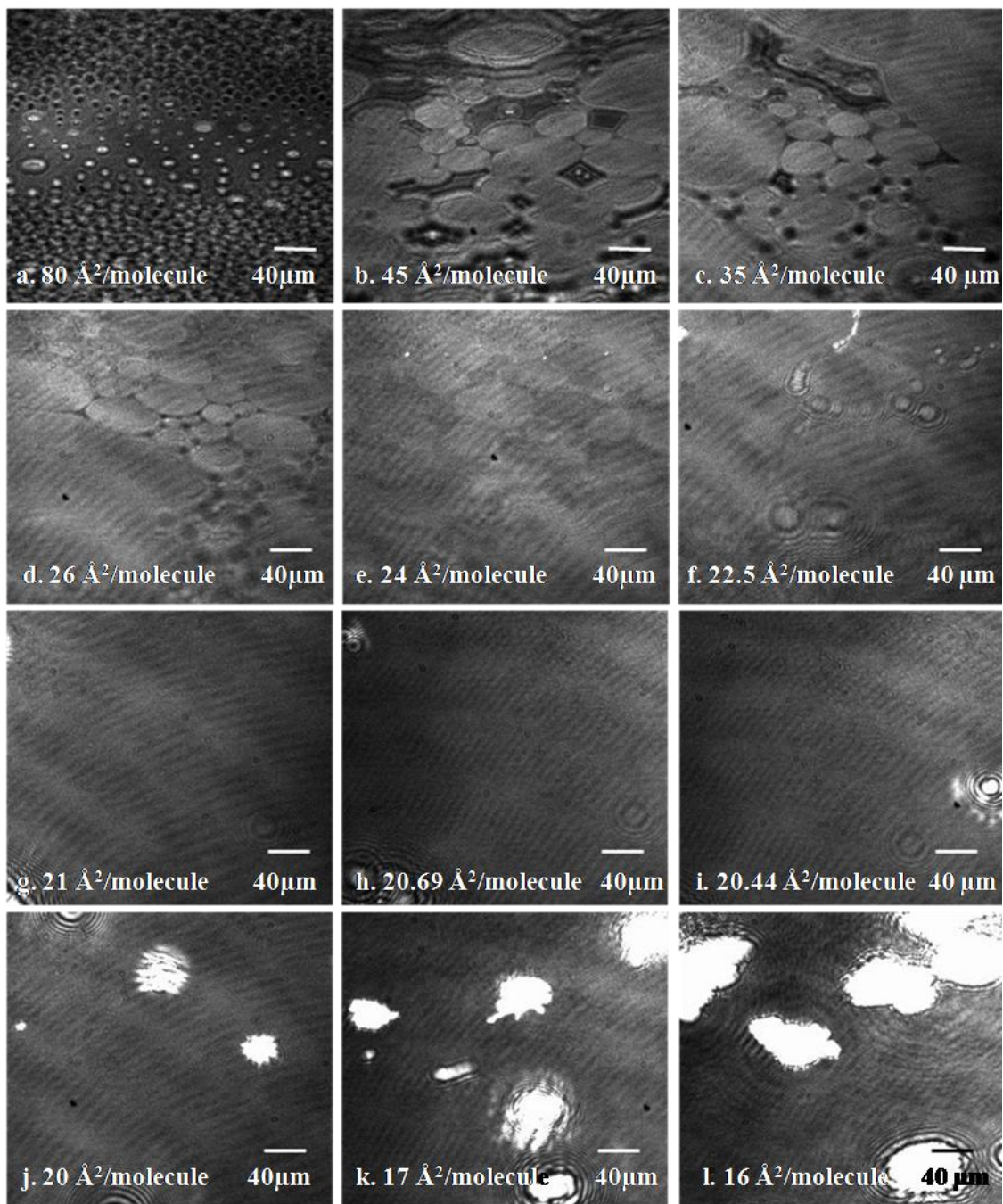


Figure 3.7 BAM Images of PA on water subphase at 24°C and total barrier compression speed rate of 5 mm/min .

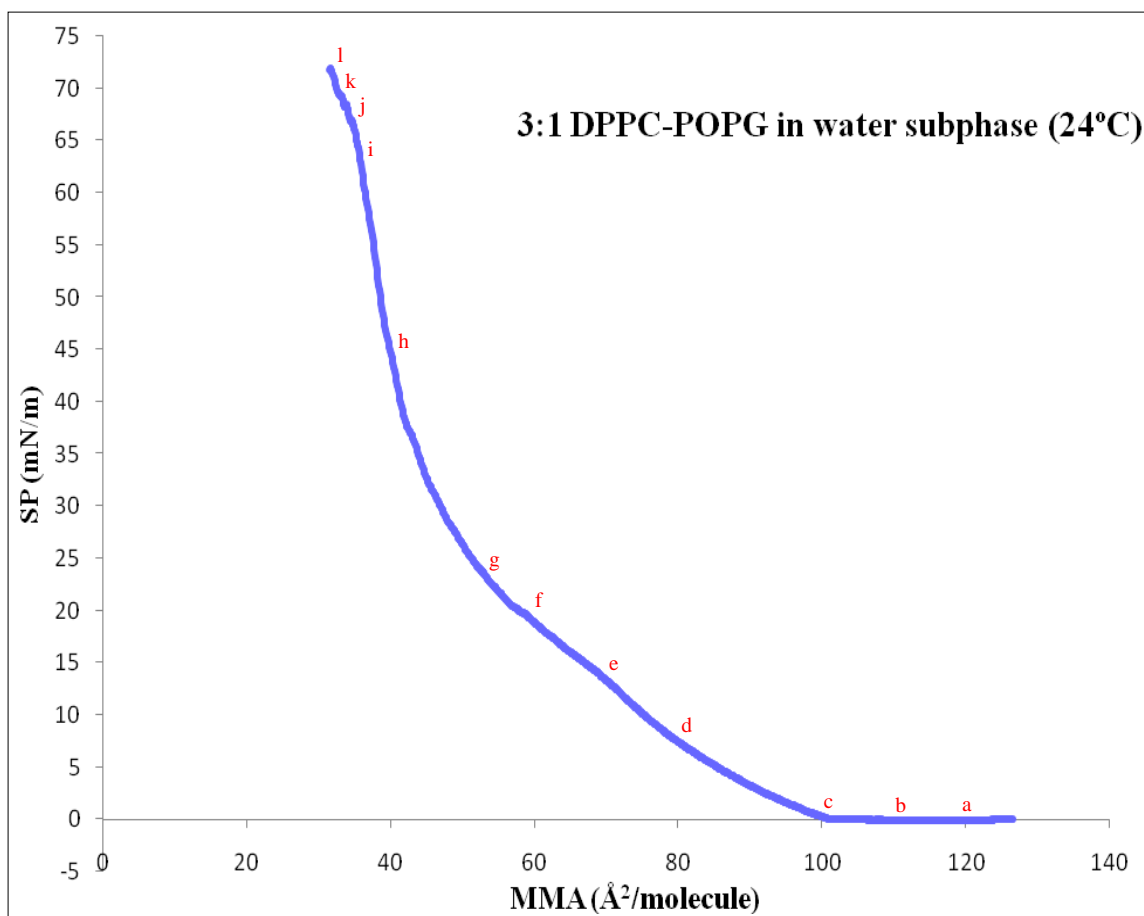


Figure 3.8 Surface pressure-area isotherm of 3:1 DPPC-POPG on water subphase.

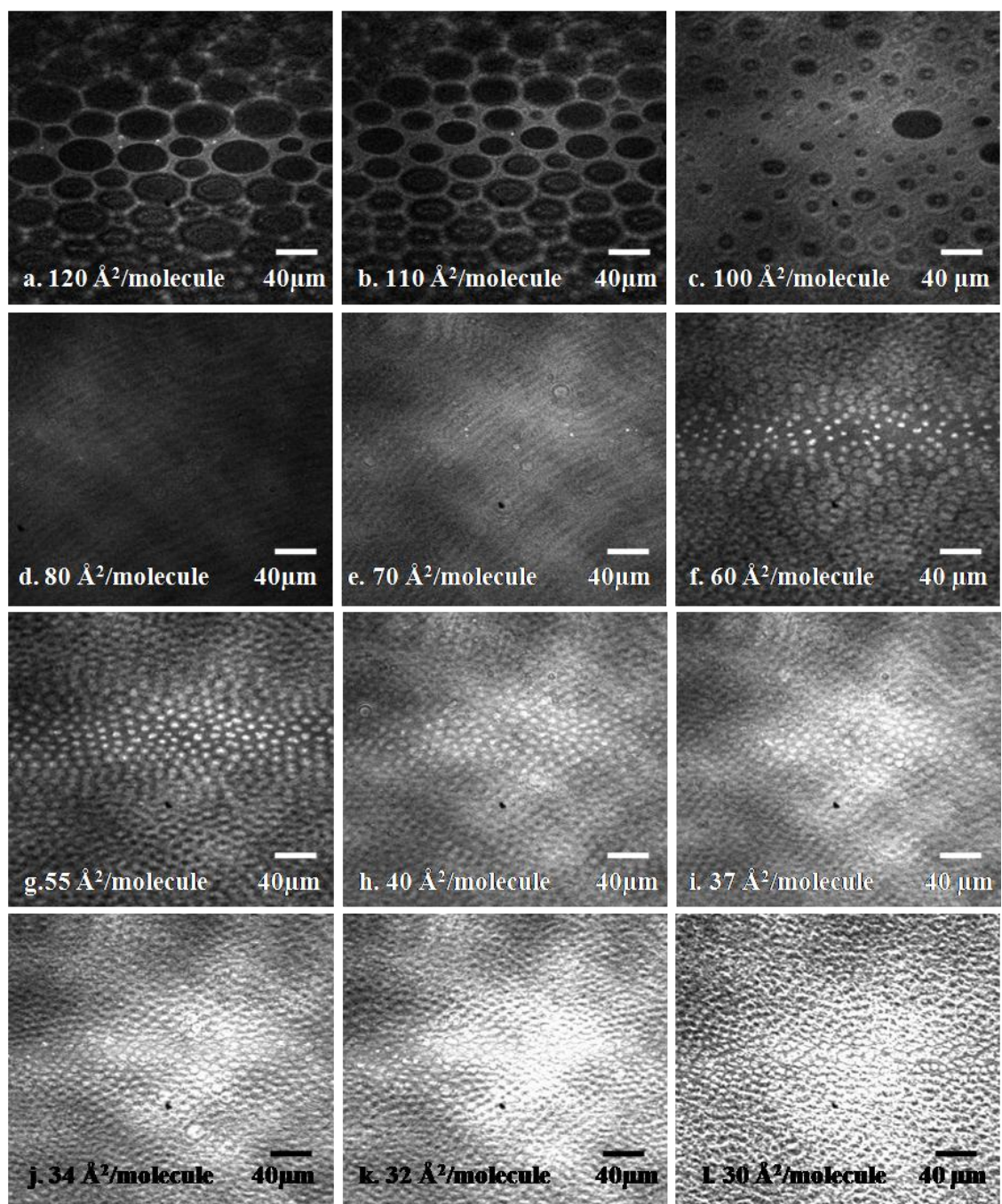


Figure 3.9 BAM Images of 3:1 DPPC-POPG on water subphase at 24°C and total barrier compression speed rate of 5 mm/min.

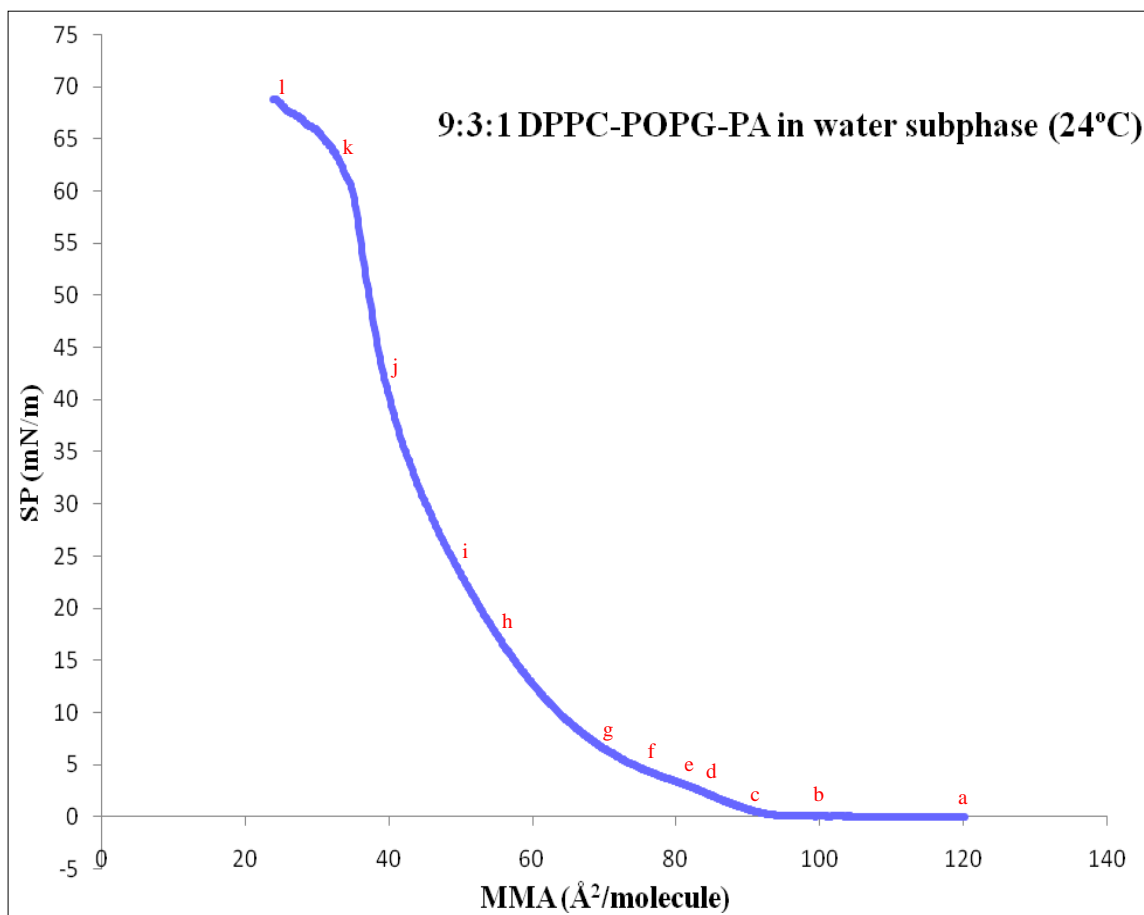


Figure 3.10 Surface pressure-area isotherm of 9:3:1 DPPC-POPG-PA on water subphase.

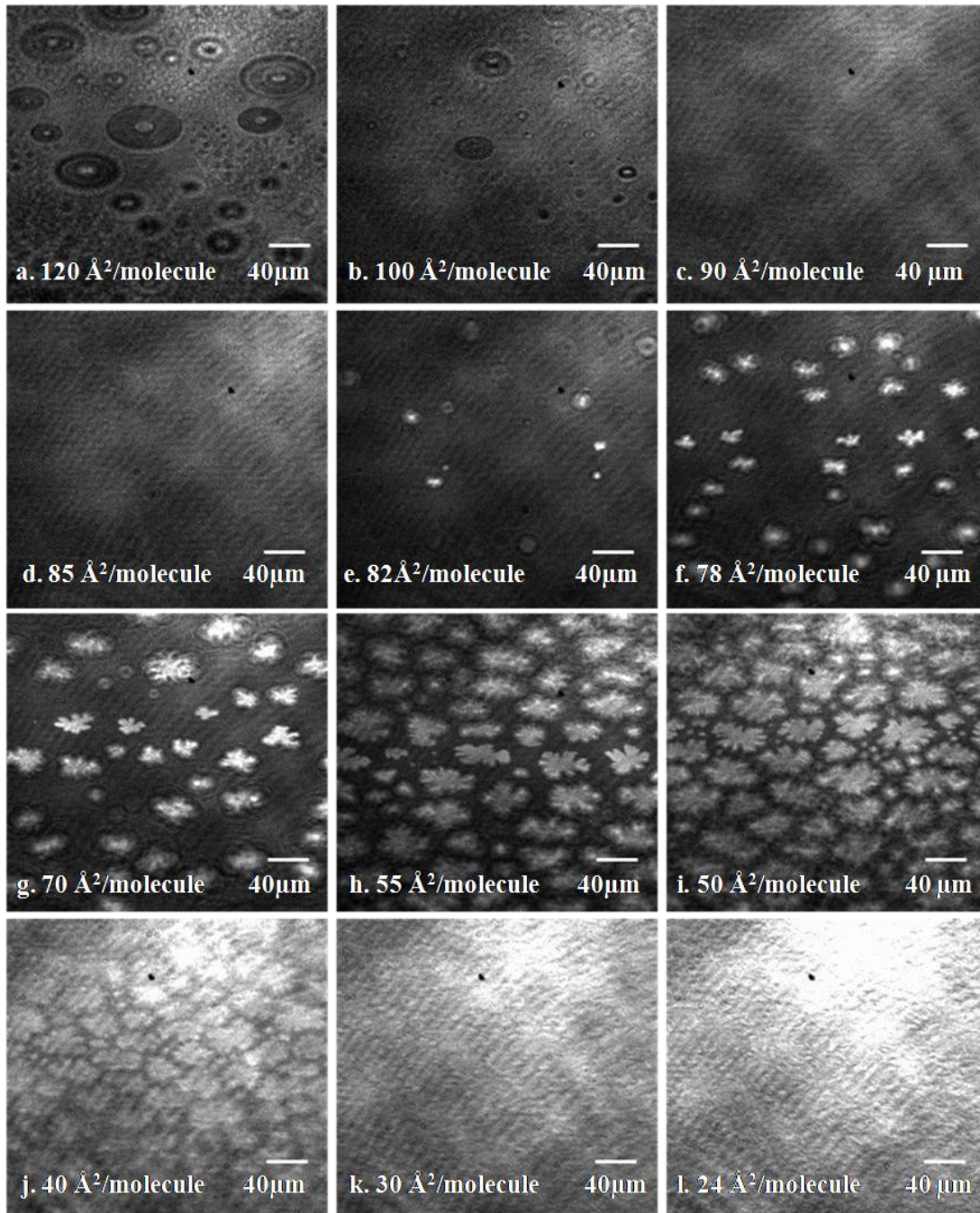


Figure 3.11 BAM Images of 9:3:1 DPPC-POPG-PA on water subphase at 24°C and total barrier compression speed rate of 5 mm/min.

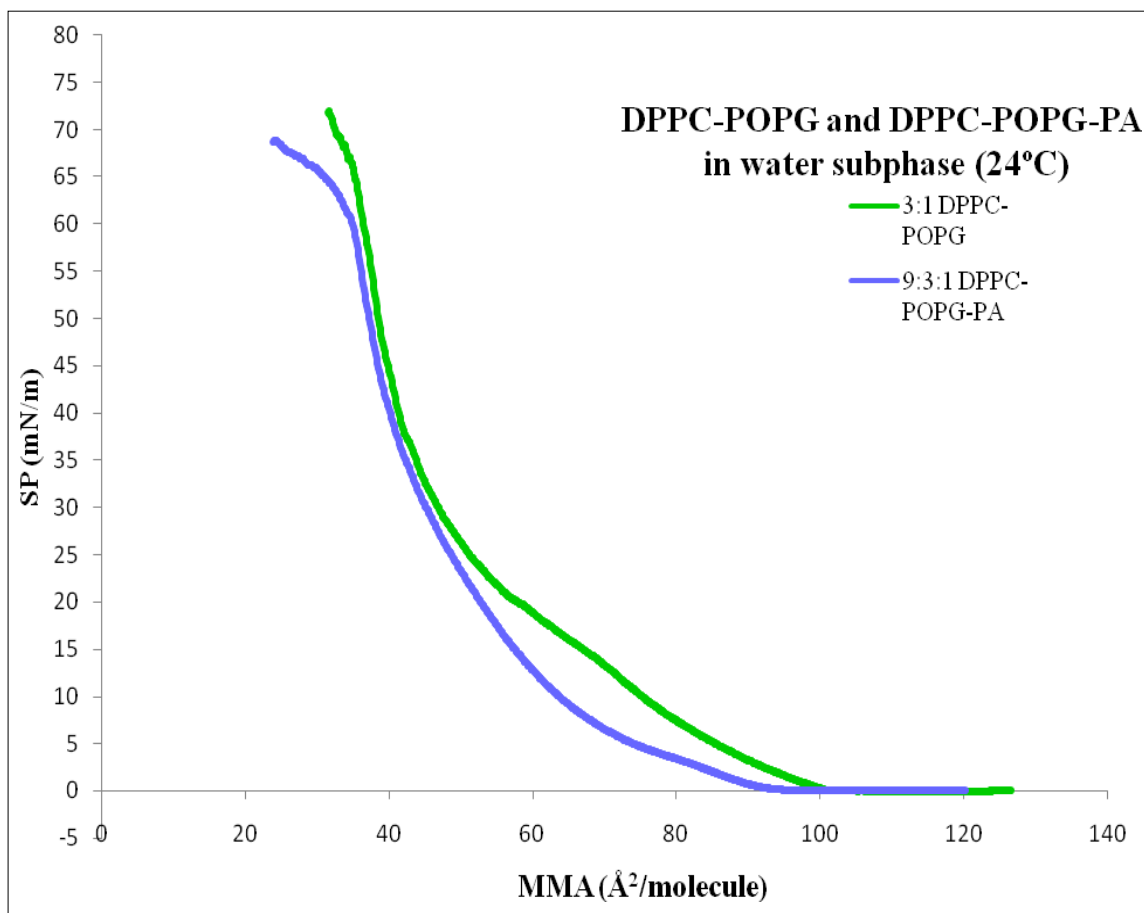


Figure 3.12 Surface pressure-area isotherm of 9:3:1 DPPC-POPG-PA and 3:1 DPPC-POPG on water subphase at 24°C.

CHAPTER 4

BREWSTER ANGLE MICROSCOPY STUDIES OF LUNG SURFACTANT ON PHYSIOLOGICAL BUFFER SOLUTION

4.1 Introduction

The discovery of pulmonary surfactant goes back to 1955 when Pattle demonstrated the presence of surface active molecules in the mammalian lungs. Pattle studied the lifetime and stability of air bubbles in foam squeezed from lung slices and from his investigations, he was able to illustrate the presence of surfactant capable of achieving very low surface tension. The stability and relative ease of inflation in normal lungs is made possible because of the existence of these pulmonary surfactants.¹⁷ In Chapter 3, the composition of these lung surfactants were fairly established. To reiterate, composition analysis of lung surfactant reveal that it is composed of lipid and phospholipid (about 90%) fractions and surfactant-specific protein fractions (about 10%).^{2,3,14,15} Three of the key components in exogenous lung surfactants^{13,17-19} were chosen to construct the model lung surfactant monolayers, including DPPC, palmitoyloleoylphosphatidylglycerol (POPG), and palmitic acid (PA).

The presence of a high relative amount of DPPC in both the natural and artificial lung surfactants is generally agreed to be the chief reason in attaining a low lung surface

tension and prevents the alveolus from collapsing.^{9,15,85} The presence of other components such as phosphatidylglycerols, unsaturated phospholipids and the hydrophobic proteins SP-B and SP-C, on the other hand, help the spreading characteristics of DPPC.^{9,85} It was pointed out in the study of Ma et al⁹ that the ternary mixture of DPPC, POPG and PA is not enough to achieve as high a static surface pressure upon compression as do DPPC alone and thus, the simple mixture of these compounds is not enough to provide proper properties to a successful replacement lung surfactant. Four proteins named as SP-A, SP-B, SP-C and SP-D, have been identified to associate with lung surfactant besides phospholipids.^{80,85,156} As discussed in Chapter 3, the hydrophilic proteins SP-A and SP-D are thought to be involved in the transport and storage of lung surfactants and play an important role in host defense. The proteins SP-B and SP-C, on the other hand, are both hydrophobic proteins and are strongly believed to be significant factors in the adsorption and spreading of monolayers having DPPC, which is thought to slowly adsorb and poorly respreads on its own at the air/liquid interface.^{9,85,157} In a study made by Revak et al in 1991,¹⁵⁸ they have reported that their data have demonstrated a series of peptides identical to the carboxy-terminal of the SP-B protein capable of producing a synthetic surfactant when appropriately combined with DPPC and PG in a 3:1 ratio. According to their study, the peptide is a 17 to 45 residues in length and together with the phospholipids, can act like the amniotic fluid-derived human surfactant in terms of its biophysical behavior. In 1996, Cochrane et al (119) made a study, reporting that a synthetic surfactant containing DPPC, POPG, PA and KL4 created

a strong and durable surfactant activity and that is very effective in the clinical treatment of animal and human respiratory distress syndrome.^{9,85}

KL₄ is a 21 amino acid synthetic peptide containing repeating subunits of one lysine (K) and four leucine (L) residues.^{17,159} KL₄, which is based on SP-B structure and sometimes referred to as the hydrophobic peptide, is the major component of Surfaxin, which is a potential therapeutic agent for RDS in preterm infants.^{14,85} Since the discovery of KL₄, numerous studies^{9,11,13,14,75,85,88,90,159} have been made to be able to know the biophysical and clinical aspects of this peptide and its mixtures.

In this thesis, different lung surfactant components and their mixtures were studied using surface pressure-area (Langmuir) isotherms and Brewster angle microscopy (BAM) using 0.15M NaCl solution and at the physiological pH of 7.0. The main interest in this study is to observe the behavior of the different samples of lung surfactant components in a more physiological environment other than water. To mimic the physiological environment subphase, a buffered (pH 7) saline solution containing sodium chloride (NaCl), EDTA and tris buffer is used. Also, the results in this study are contrasted with the results of the Langmuir isotherms and BAM images of the same lipid and lipid mixture samples in water (pH 5.5) subphase from Chapter 3.

4.2 Experimental

4.2.1 Materials

The lipids used in this study were 1,2-dipalmitoyl-sn-glycero-3-phosphocholine (DPPC), 1-palmitoyl-2-oleoyl-sn-glycerol-3-phosphatidyl-glycerol (POPG) were

purchased from Avanti Polar Lipids (Alabaster, AL) with >99% purity. Palmitic acid (99% purity) was purchased from Sigma-Aldrich. The KL₄ peptide was custom-synthesized by Biopeptide CO., LLC (San Diego, CA) with a purity of 98% by HPLC. The KL₄ peptide has an amino acid sequence of KLLLLKLLLLKLLLLKLLLLK where K represents the amino acid lysine while L represents the amino acid leucine. Methanol, chloroform (spectrophotometric grades), ethylenediaminetetraacetic acid (EDTA) disodium salt, tris(hydroxymethyl) aminomethane base (Trizma), sodium chloride (NaCl) and hydrochloric acid were purchased from Fisher Scientific. Nanopure water was obtained from a Barnstead Nanopure filtration system with a resistivity of 18.3 MΩ•cm. The subphase used in the monolayer is an aqueous solution which consists of 150 mM sodium chloride and 0.1 mM EDTA in 5 mM Tris buffer at pH of 7.0. All experiments were conducted at room temperature (23°C ± 1°C) and at atmospheric pressure.

4.2.2 Sample Preparation

Stock solutions of DPPC and PA each with 1mM concentration were made in chloroform. Stock solution of POPG with 1mM concentration and a stock solution of KL₄ with 0.65 mg/mL concentration were made using chloroform/methanol mixture in a 3:1 vol/vol ratio. These solutions were mixed in appropriate ratios to form model lung surfactant mixtures containing 3:1 DPPC-POPG, 9:3:1 DPPC-POPG-PA and 66/22/7/5 by weight DPPC-POPG-PA-KL₄. This formula has been used in previous lung surfactant studies.^{11,13} As mentioned in Chapter 3, these formula mixtures prepared in smaller ratios are close functional mimic to natural lung surfactants both in vitro and in vivo and are

used in previous studies.^{11,13,76,154} The subphase used in the monolayer measurements was the physiological buffer solution with pH of 7.0.

4.2.3 Methods

Langmuir Film Balance. Surface pressure-area isotherm studies were done in a Langmuir film balance that is equipped with a KSV minitrough (KSV, Finland, 176.5 mm x 85 mm, teflon), two barriers (coated with Delrin) to provide symmetric film compression, balance and a controller unit. Monitoring of the surface pressure and mean molecular area during film compression were done using the Wilhelmy plate method (filter paper was used to serve as the plate). Once the trough was filled with buffer solution as subphase, the barriers were closed so as to check that there is nothing in the surface that could increase the surface pressure and could make each experiment inaccurate. After this checking was done, a known amount of the sample was spread in a drop-wise manner on the water surface using a Hamilton micro-syringe. A waiting period of ten minutes was allowed prior to the compression to allow the organic solvent evaporate completely. Each of the barriers was compressing at a speed rate of 2.5 mm/min 5 mm/min total compression speed rate for both barriers. All isotherms (at least before the collapsed phase region) presented were ensured to be generated reproducibly. Reproducibility was ascertained by running multiple Langmuir film balance and BAM microscopy experiments of each individual and mixed component and ensuring generated isotherms for each compound to be on top of each other (error bars are within the lines).

Brewster Angle Microscopy. The KSV Langmuir trough was equipped with the home-built Brewster angle microscope as described in Chapter 2 and Chapter 3. The Brewster angle for the buffer subphase has the same angle as the water subphase (53.1°) although the subphase incorporates some saline component (0.15 M sodium chloride, about 0.88%). The refractive index of sodium chloride in its crystalline form (as salt) is about 1.544¹⁶⁰ but the refractive index of a saline solution, which has a concentration of less than 2.5 %, is nearly the same as that of pure water (about 1.333).¹⁶¹ Therefore, calculations of the Brewster angle ($\arctan(1.333/1)$) will give the same angle as with water (53.1°). Physically, reflection of light is not observed or more appropriately, at the minimum in the 53.1° angle position of the goniometer of the BAM. In addition, the BAM images acquired at this angle on the surface of the pure buffer were dark and the counts given by the CCD camera are at minimum like the BAM images of water subphase. With these, all the Langmuir and BAM experiments on the buffer subphase were made using this angle. The final images taken were cropped from a 512 x 512 pixel size to a 250 x 250 pixel size to show the most resolved regions of the images and the images were scaled using a BAM captured image of an actual stage micrometer. No more additional processing was done with the images.

4.3 Results and Discussion

4.3.1 BAM Images and Compression Isotherms of Individual Lipids and Fatty Acid

4.3.1.1 DPPC

Surface pressure-area Isotherm. Figure 4.1 presents the surface pressure-area isotherm of DPPC on physiological buffer solution subphase and compares it to the surface pressure-area isotherm of DPPC on water subphase. It can be seen in this figure that the “lift-off” point ($\sim 113 \text{ \AA}^2/\text{molecule}$) of DPPC on physiological buffer solution with 0.15 M NaCl is shifted to a higher mean molecular area as well as the LE ($\sim 113 \text{ \AA}^2/\text{molecule}$) and LE-LC ($\sim 90 \text{ \AA}^2/\text{molecule}$) phase regions with respect to the isotherm of DPPC on pure water subphase. Also, it can be noted that there is an increase in the surface pressure at a fixed area per molecule in the coexistence regions. The same results have been reported from different studies^{139,144,162} where the compression isotherm for DPPC shifts to slightly higher pressures in the LE and LE-LC phase regions when sodium ions are present in the subphase. The reason provided for these shifts is that the ions bind to the LE phase causing disorder of the lipid chains¹³⁹ or more specifically, the sodium ions interacts with the headgroup of the phospholipids and this interaction brings disorder in the lipids chains.¹⁴⁴ After the LE-LC phase transition, the isotherm of DPPC on buffer subphase steadily increase in terms of the surface pressure and collapses at a lower pressure of about 59 mN/m) which is about 10 mN/m lower than the collapse pressure of DPPC on water subphase. Apart from these differences, no additional kinks or plateaus were observed present in the isotherm.

BAM Images. Figure 4.2 shows the BAM images that depicts the behavior of DPPC on physiological buffer solution. At the beginning, as the monolayer is started compressing, in the G-LE phase of the isotherm in Figure 4.1, it can be seen that the monolayer has dark homogeneous background without any contrast (Figure 4.2 a). This is different from the DPPC spread on water subphase in that there were no dark circular “holes” observed. These dark circular holes are considered as disordered regions of the monolayer.⁶⁹ This dark and homogeneous background surface is continuously seen during the lift-off point of the isotherm at about $110 \text{ \AA}^2/\text{molecule}$ (Figure 4.2 b) and a relatively lighter (dark to gray colored) but still homogeneous background is observed in the LE phase of the isotherm (Figure 4.2 c). Such absence of contrast is well-matched with the uniform LE phase.¹⁴³ As the isotherm approaches the LE-LC phase transition, small white dots starts to appear, indicating the nucleation of the domains typically seen as the transition phase of DPPC commences. The appearance of these small white circular domains at $90 \text{ \AA}^2/\text{molecule}$, indeed demonstrate and confirm the shift in the isotherm of DPPC in the buffer subphase relative to the DPPC molecules spread on the water subphase where the white spots come into view at a smaller mean molecular area (about $80 \text{ \AA}^2/\text{molecule}$). The sizes of these white spots are between $2.5 \mu\text{m}$ and $10 \mu\text{m}$. Upon further compression, these domains progress into bigger sizes ($> 50 \mu\text{m}$), more explicit multilobed domain shapes and sometimes fractal-like shapes^{155,163,164} as can be seen in Figures 4.2 d to h. In comparison with the DPPC in water subphase, these distinct, full-sized domains appear on a much longer stretch of mean molecular area although started to form in a much larger area, earlier in the isotherm. This behavior in the BAM should have made the

plateau in the isotherm longer but is not obviously seen in Figure 4.1. On further decrease of the mean molecular area accompanied by increase of surface pressure, a much lighter homogeneous surface (Figures 4.2 i and j), relative to the G-LE and LE phase, is observed. These BAM images are consistent with the condensed phase in the isotherm. The BAM images after more compression (Figure 4.1 k and l) shows increase in the intensity of brightness without any distinguishable domains. This increase in light intensity is consistent with the characteristic of collapse phase in BAM images. The isotherm behavior in these mean molecular areas confirms that the monolayer undergoes collapse.

4.3.1.2 POPG

Surface pressure-area Isotherm. The surface pressure-area isotherm of POPG on physiological buffer subphase is shown in Figure 4.3 together with the isotherm of POPG on water subphase. Similar to the isotherm of DPPC on buffer subphase, the isotherm of POPG on buffer subphase is also shifted to the right (larger mean molecular area) relative to the isotherm of the same compound spread on water subphase. The curve, upon compression, does not show any signs of kinks or plateaus, but a continuous typical isotherm curve as the surface pressure increases on decreasing mean molecular area at least before the collapse phase. The plateau at higher surface pressure (about 39.5 mN/m) signifies that the monolayer has approached the collapse phase. Moreover, this surface pressure at the collapse phase is lower than the observed collapse pressure of POPG on water subphase (about 48 mN/m).

BAM Images. The BAM images in Figure 4.4 illustrates the behavior of POPG monolayer spread on buffer subphase at 24°C in different compression stages.

The only feature that varies in all the images is the background contrast from dark (Figures 4.4 a to c) to gray (Figures 4.4 d to f) to bright-colored background (Figures g to h). Apart from these observations, the images are featureless in terms of domain formation all throughout the compression.

4.3.1.3 PA

Surface pressure-area Isotherm. The behavior of the surface pressure-area isotherm of PA on buffer subphase at 24°C is shown in Figure 4.5. The surface pressure-area isotherm of PA on water subphase is also shown in the figure. Consistent with the observations in DPPC and POPG's isotherm on buffer subphase, the surface pressure area-isotherm of PA spread on buffer subphase also follows the same trend where the lift-off point is displaced to higher mean molecular area ($\sim 51 \text{ \AA}^2/\text{molecule}$) relative to the lift-off point of the isotherm of PA on water subphase ($\sim 26 \text{ \AA}^2/\text{molecule}$). Next to this lift-off point, according to the phases of PA (on water subphase) is the tilted condensed (TC) phase. The TC phase in this isotherm is characterized by a curve and a gradual increase in the surface pressure upon compression as opposed to the abrupt curve observed in PA on water subphase. A less defined kink can also be observed in the isotherm which, in the isotherm of PA on water subphase, indicates a second order transition from TC to UC (untilted condensed) phase. After this kink, a relatively steeper slope is observed in the graph that soars as high as about 55 mN/m and then the isotherm

becomes unstable signaling the collapse phase of the monolayer. After the kink region, two differences can be observed between the PA spread on buffer subphase and the PA spread on water subphase. The first is that the UC phase of the PA on water subphase is much steeper than the UC phase of PA on the buffer subphase. The second is that, the UC phase on water subphase only went up to a surface pressure of about 40 mN/m before the collapse region which is about 15 mN/m lower than the isotherm of PA on buffer subphase. In the collapse region, the curve of PA on buffer subphase either plateaus or continuously ascends as oppose to the steep descent of the collapse phase of PA on water subphase.

BAM Images. Figure 4.6 represents the BAM images of PA spread on buffer subphase at 24°C. On the onset of compression at about 80 Å²/molecule, white elliptical domains in dark background can be observed (Figure 4.6 a). These domains have varied sizes of about >10 μm for the small domains to 70 μm for the bigger domains. These domains are much bigger with much more varied sizes as oppose to the small circular domains (5-20μm) seen on the BAM images of PA on water subphase at the same molecular area. Moving to smaller mean molecular areas upon compression, the domains remain in their sizes, that is a mixture of small (10 μm) to large (70 μm) domain sizes can still be observed as represented by Figures 4.6 b and c. Upon further compression (Figures 4.6 d and e), the domains are observed to come closer after the lift-off point of approximately 50 Å²/molecule. At about 25 Å²/molecule or 15 mN/m surface pressure, the domains are observed to fuse and form bigger domains as the isotherm approaches the kink at about

23 Å²/molecule. At this kink (Figure 4.6 g) we can observe that the monolayer forms a homogeneous film with very few small and bright spots. Beyond the kink (Figure 4.6 h to k), the same homogenous film is observed but there is an increase in the quantity and size of the bright spots. As the surface pressure is increased, a more intense brightness in the succeeding images is observed, as represented by Figure 4.6 l that is consistent with the surface pressure and mean molecular area of the collapse phase in the isotherm.

4.3.2 BAM Images and Compression Isotherms of Mixed Lipids, Fatty Acid and Peptide

4.3.2.1 DPPC-POPG

Surface pressure-area Isotherm. Figure 4.7 shows the surface pressure-area isotherm of 3:1 DPPC-POPG mixture spread on buffer subphase at 24°C. The lift-off point in this isotherm occurs at around 118 Å²/molecule. The isotherm continues to rise gradually upon compression without any kinks or plateau features as seen in the LE-LC phase transition in DPPC isotherms. The isotherm ascends up to about 61 mN/m surface pressure before the monolayer collapses. In comparison to the isotherm of 3:1 DPPC-POPG on water subphase, the lift-off point of the isotherm occurs earlier at a higher mean molecular area, consistent with the behavior of the isotherms of individual lipids and fatty acid spread on buffer subphase relative to their isotherms spread on water subphase. Also, the smeared-out plateau in the isotherm of the same mixture on water subphase is totally eliminated and replaced by a plain curve in the isotherm on buffer subphase. A kink or bump in the isotherm that occurs at around 43 Å²/molecule and 46 mN/m can be observed but there are no corresponding remarkable changes noticed in the BAM images.

Another difference between the mixture spread on water subphase and on the buffer subphase is that the collapse point of the later occurs at a much lower surface pressure than the former by about more than 5 mN/m surface pressure.

BAM Images. The BAM images in Figure 4.8 represent the progression of the 3:1 DPPC-POPG mixture as the monolayer is compressed. As the isotherm progresses from the gas-LC phase to the lift-off point, no corresponding changes in the dark background contrast is observed (Figure 4.8 a to d). The first change in the contrast occurs at about $78 \text{ \AA}^2/\text{molecule}$ (Figure 4.8 e) when small white spots having an average size of about $2.5 \mu\text{m}$ start to appear in the monolayer. These small white spots get bigger (Figures 4.8 f and g) as the monolayer is compressed to an average size of $10 \mu\text{m}$. Upon further compression, these domains shrink in size (Figure 4.8 h) and as the isotherm approaches the kink or bump in the isotherm that occurs at around $43 \text{ \AA}^2/\text{molecule}$ and 46 mN/m , as mentioned above, there are no corresponding remarkable changes noticed in the BAM images (Figure 4.8 i). These small white domains are continuously seen in the succeeding BAM images and upon further compression and as the isotherm rise up to the collapse point. At the collapse, and an intense, bright background contrast is observed. In comparison to the mixture spread on water subphase, there is no inversion of contrast of the domain and background observed at the onset of the compression. The homogeneous dark background is seen from the beginning of compression whereas in the mixture on water subphase, it is observed at a later compression of about $80 \text{ \AA}^2/\text{molecule}$. Although in the appearance of the small white domains, there is no significant delay in the mean

molecular area or surface pressure observed in both experimental set-ups. The presence of the domains is also continuously seen from their onset up to the collapse in either scenario with the shrinking of the domain size in the mixture spread on buffer subphase.

4.3.2.2 DPPC-POPG-PA

Surface pressure-area Isotherm. When PA is added to the mixture of DPPC and POPG in a 9:3:1 DPPC-POPG-PA ratio mixture and spread on a buffer subphase of pH 7.0 at 24°C, the resulting surface pressure-area isotherm upon compression can be seen in Figure 4.9 along side the isotherm of the same mixture spread on a water subphase. The lift-off point of the mixture on the buffer solution occurs around 105 Å²/molecule, the isotherm gradually rises up, and then it starts to shortly plateau at a mean molecular area of 84 Å²/molecule and about 4 mN/m surface pressure. This lift-off point of the isotherm occurs to about 15 Å²/molecule earlier than the mixture on water subphase but the plateau occurs at about the same area but about 2 mN/m surface pressure higher. The isotherm plateaus very subtly, which behaves similarly to the mixture on water subphase, and it continues to steadily ascends to which another kink or bump in the isotherm is observed that happens around 40 Å²/molecule and 43 mN/m. After which, the isotherm incessantly goes up until the monolayer collapses and the isotherm plateaus at about 29 Å²/molecule and 59 mN/m. In the mixture spread on water subphase, there is no second bump observed in the isotherm and the collapse point occurs at a higher surface pressure, which is about 7 mN/m higher than the monolayer spread on buffer subphase.

BAM Images. In looking at the BAM images of 9:3:1 DPPC-POPG-PA in Figure 4.10, a homogeneous dark background without any contrast can be observed starting from the onset of the isotherm, moving up to the lift-off point and as the isotherm continues to rise up as represented by Figures 4.10 a to d. The same behavior is seen in the BAM images of 3:1 DPPC-POPG as described above. The first appearance of any feature in the BAM images is small white spots having an average of $5\mu\text{m}$ in size. As the monolayer is compressed, these spots start to grow to an average size of $7.5\mu\text{m}$ in Figure 4.10 f and then reaching an average full size of $15\mu\text{m}$ (Figure 4.10 g and h). These domains also become more apparent as the contrast in the background becomes darker and the domains brighter. The appearance of the small white spots in the BAM images well corresponds to the smeared-out plateau region of the mixture's isotherm. Upon further compression, the contrast of the images declines but their shapes and sizes are retained and the domains come closer together. These observations happen at the second bump in the isotherm around $40\text{ \AA}^2/\text{molecule}$ and 43mN/m as described in the isotherm above. In Figure 4.10 k, an almost homogeneous surface is observed and as the isotherm advances toward the collapse point, the intensity of the brightness of the image starts to build up and the BAM image represents a very intense bright surface (Figure 4.10 l). However, it can be observed that even if the contrast of the background is bright, the re-appearance of the full-sized domains is dimly seen in the image. It is of notable observation that the domains developed on the buffer subphase are significantly different from the shapes of the domain on water subphase. The full sized domains on buffer subphase are circular

and other domains resemble some bean-shaped like structure while the domains on water subphase develop as fractal-like shape pattern.

4.3.2.2 DPPC-POPG-PA-KL₄

Surface pressure-area Isotherm. Figure 4.11 shows the surface pressure-area isotherm of the 66/22/7/5 by weight DPPC-POPG-PA-KL₄ mixture. The isotherms of the binary mixture DPPC-POPG and the ternary mixture of DPPC-POPG-PA are also shown in this figure. The isotherm of the quaternary mixture has a lift-off point approximately around 136 Å²/molecule mean molecular area. This lift-off point, as can be seen from the figure occurs relatively farther to the right of the binary and ternary mixtures. This shifting of the isotherm to the right is consistent with the results of Ma et al⁹ where KL₄, although present in small quantity (~2.5% by weight), made some significant effect in shifting the surface pressure-area isotherm of DPPC and POPG to the right. In addition, this shifting brings with it a higher surface pressure for a given area than the phospholipids alone. This shifting of the isotherm also agrees with the constructed isotherm of DPPC-POPG-PA-KL₄ mixture in Ma et al's paper.⁹ It was construed that shifting of isotherms to the left means a more condensed, miscible mixture and a strong inter-component interactions (interactions between different components) hence a negative deviation from ideality. On the other hand, a shift to the right means a more expanded mixture and a positive deviation from ideality, indicating a tendency of unlike compounds to de-mix (weak interaction between different components) but a stronger interaction between like components.⁹

As the isotherm of the quaternary mixture progresses upon compression, a smooth curve rises up without any kinks or plateaus observed. The isotherm then encounters a plateau at around $48 \text{ \AA}^2/\text{molecule}$ and 42.6 mN/m . This plateau or kink is said to likely be due to the collapse of the less stable component.¹³ Upon further compression, the plateau smears out as the isotherm gradually rises up and upon close examination of the isotherm, the curve appears to change its slope to a steeper curve starting to about $32 \text{ \AA}^2/\text{molecule}$ and 46 mN/m and then the curve continues to rise up. In Ma and Allen's paper in 2006,¹³ they have reported two collapse kinks in the compression-expansion isotherm of DPPC₆₂-POPG-PA-KL₄ on buffer (pH 7) subphase containing 100 mM NaCl . These kinks occur at approximately around 49 mN/m and $47 \text{ \AA}^2/\text{molecule}$ for the first kink and 72 mN/m and $29 \text{ \AA}^2/\text{molecule}$ for the second kink. These two kinks were attributed to the collapse of the less stable component (such as POPG and KL₄) and the collapse of DPPC molecules respectively. The isotherm of the quaternary mixture in the present study is different from Ma and Allen's paper¹³ in terms of the behavior of the curve at higher surface pressures which could be due to the difference in the subphase and composition, specifically, between the deuterated DPPC₆₂ used in the Ma's paper. However the resulting isotherm in Figure 4.11 behaves about similarly with the isotherm of the same quaternary mixture from Ma, Koppenol, Yu and Zografí paper⁹ with respect to the collapse phase reaching only less than 50 mN/m collapse surface pressures. Moreover, in this study, the first kink/plateau at $48 \text{ \AA}^2/\text{molecule}$ and the second change of slope at $32 \text{ \AA}^2/\text{molecule}$ closely agrees with Ma and Allen's paper with respect to the mean molecular areas of $47 \text{ \AA}^2/\text{molecule}$ and $29 \text{ \AA}^2/\text{molecule}$, respectively.

BAM Images. The BAM images of the mixture DPPC-POPG-PA-KL₄ in Figure 4.12 presents some interesting observations upon careful examination. It is not until the isotherm reaches about 82 Å²/molecule that the presence of small white spots is observed. Prior to these appearances of minute domains having an average size of 2.5 μm, a homogeneous dark (Figure 4.12 a to c) and then gray (Figure 4.12 d and e) background can be observed upon compression. The small white spots develop in to relatively larger domains (approximately 5 μm) and become brighter (Figure 4.12 g). Upon further compression, these domains lose some of their intensity (Figure 4.12 h and i) but become bigger in size (about 10 μm). The shapes of these domains are indistinguishable which could be due to the resolution of the microscope although it can be noticed that the domains are not circular in shape. At the onset of the first collapse, small (approximately 2.5 μm in size), and bright spots starts to appear (Figure 4.12 j and k) alongside the bigger, less intense domains. These white spots tend to adhere on the edges of the bigger domains. As the isotherm is further compressed in a much smaller mean molecular area (30 Å²/molecule) and so thus higher surface pressure (~47 mN/m), even the bigger domains intensify in brightness. This is illustrated in Figure 4.12 l and additionally, we can see that the domains are much bigger in size (about 15 μm). In this image, the overall brightness has increased leading to the loss of contrast which is consistent with other collapse images. All these observations at 30 Å²/molecule occur after the change of slope in the isotherm (32 Å²/molecule) as discussed above which could infer the occurrence of collapse phase of the DPPC molecules as suggested by Ma and Allen.¹³

It was reported in Ma et al's paper⁹ that the surface phase separation of mixture of DPPC-POPG-PA is increased when KL₄ is added to the ternary system. In addition, analysis of the fluorescence images of ternary mixture of DPPC-POPG-KL₄ and the quaternary mixture of DPPC-POPG-PA-KL₄ in this study reveals that there is an increase in the fraction of liquid condensed (LC) phase domains (as represented by darker domains over the lighter background of liquid expanded phase) at very low surface pressure values and much more LC phase domains are formed at higher surface pressure upon compression.⁹ The early presence and increase of LC phase domains are interpreted as having greater surface phase separation of DPPC from the other components of the mixtures resulting in the addition of KL₄ in the systems. Such interpretation is made with the presumption that the liquid condensed domains (darker regions in Fluorescence images) are principally DPPC-rich while the lighter background of expanded phase is POPG-rich or POPG/PA-rich. While these observations were made based on the images acquired using a fluorescence microscope, the same remarks and inferences can be construed from the BAM images acquired in this study.

Furthermore, it has been deduced from Ma et al's results⁹ that the PA provides an even greater tendency toward the phase separation of DPPC from other components through the addition of KL₄ — a situation highly favored for enhanced lung activity. In Ma et al's paper, this enhanced lung activity is believed to have resulted from the addition of KL₄ in the DPPC-POPG and DPPC-POPG-PA systems as manifested by the improvement or increase in the ability of these mixtures to attain high surface pressure (> 40 mN/m) and to re-spread as opposed to their KL₄ deficient mixture counterparts that

only reach about 20 mN/m brought about by an enhancement of any factor in the phase separation of DPPC from POPG, or to any other compound in the mixture.

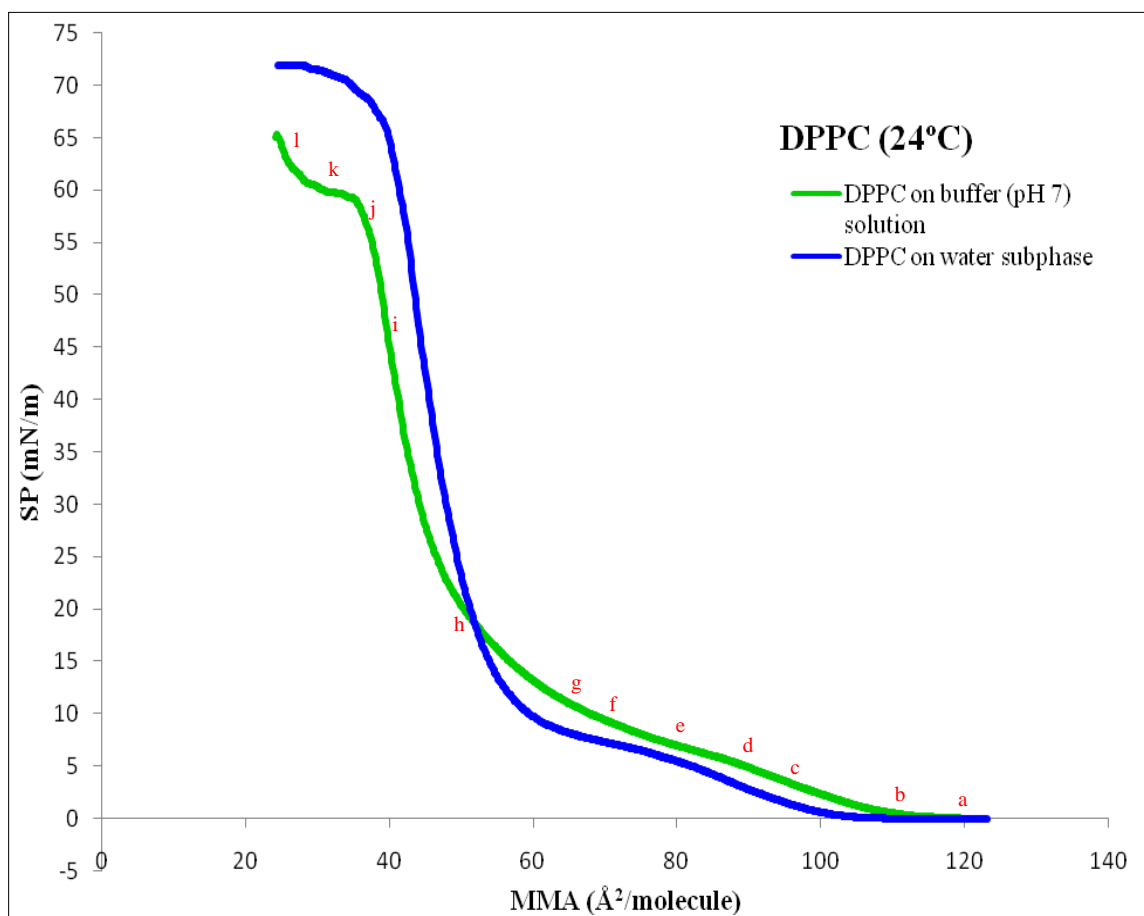


Figure 4.1 Surface pressure-area isotherm of DPPC on water subphase and on physiological buffer solution at 24°C.

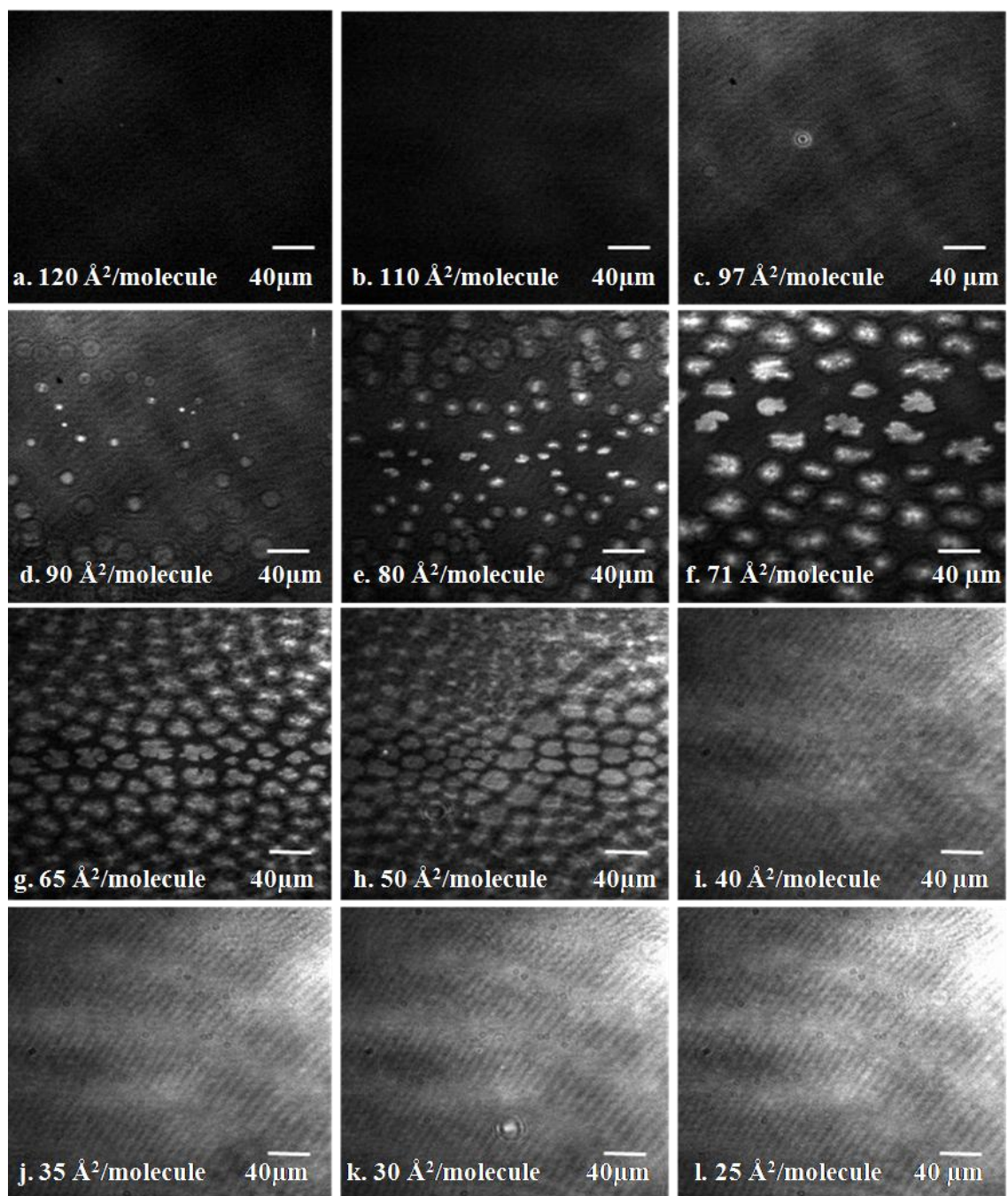


Figure 4.2 BAM Images of DPPC on physiological buffer subphase at 24°C and total barrier compression speed rate of 5 mm/min .

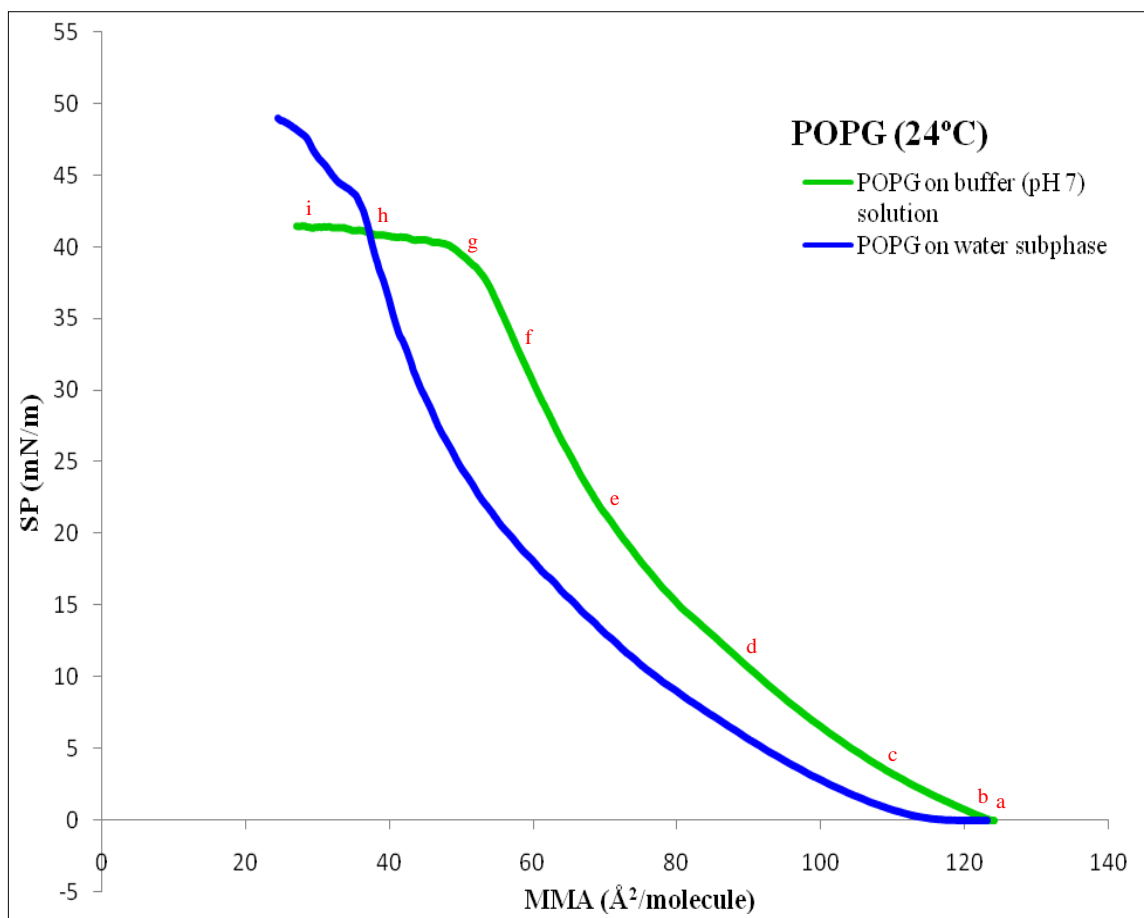


Figure 4.3 Surface pressure-area isotherm of POPG on water subphase and on physiological buffer solution at 24°C.

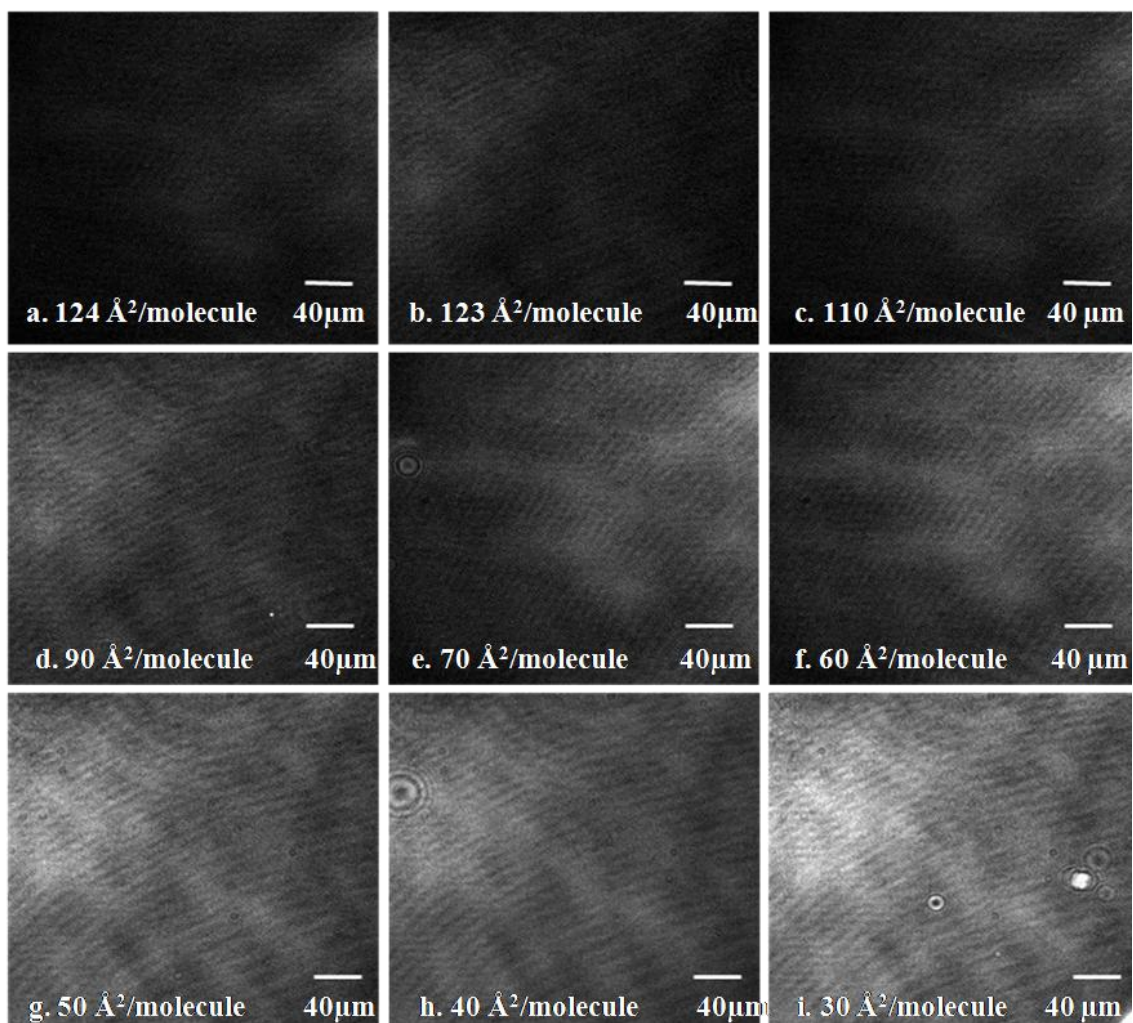


Figure 4.4 BAM Images of POPG on physiological buffer subphase at 24°C and total barrier compression speed rate of 5 mm/min.

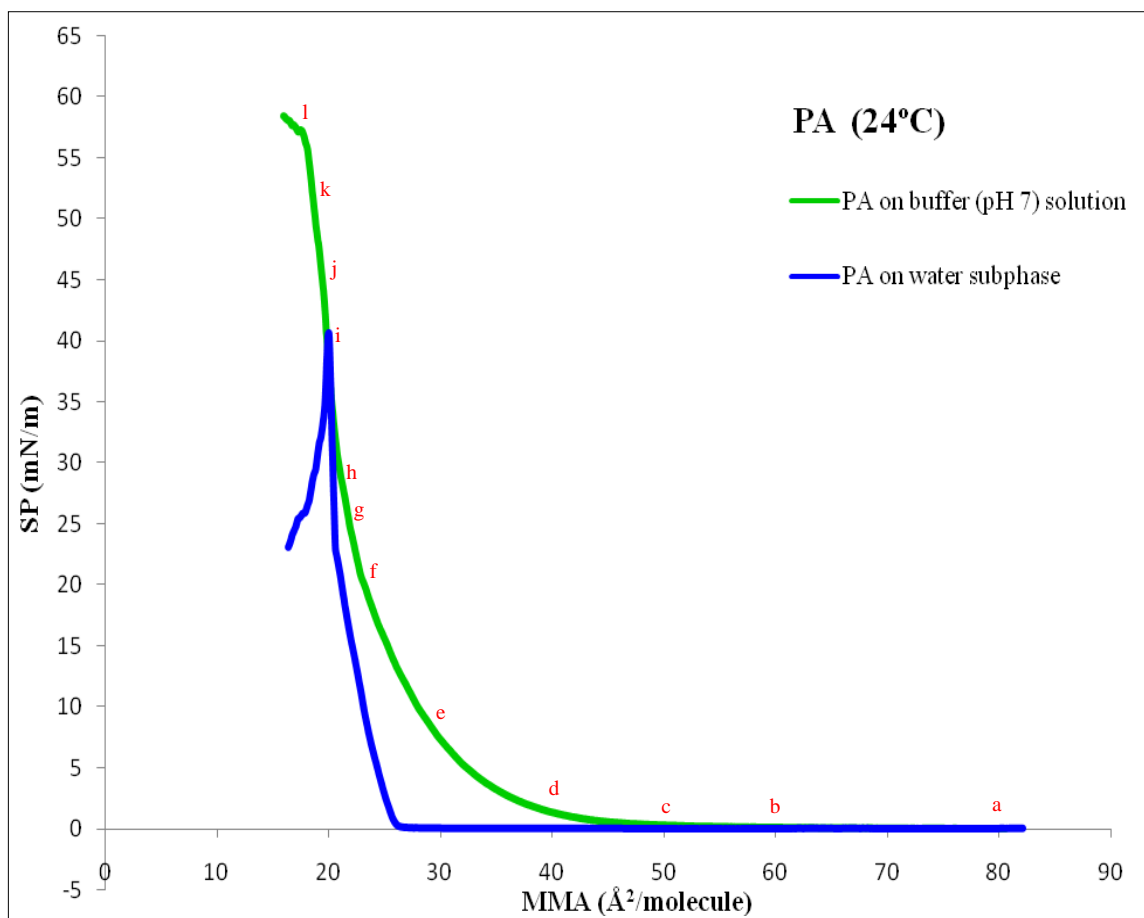


Figure 4.5 Surface pressure-area isotherm of PA on water subphase and on physiological buffer solution at 24°C.

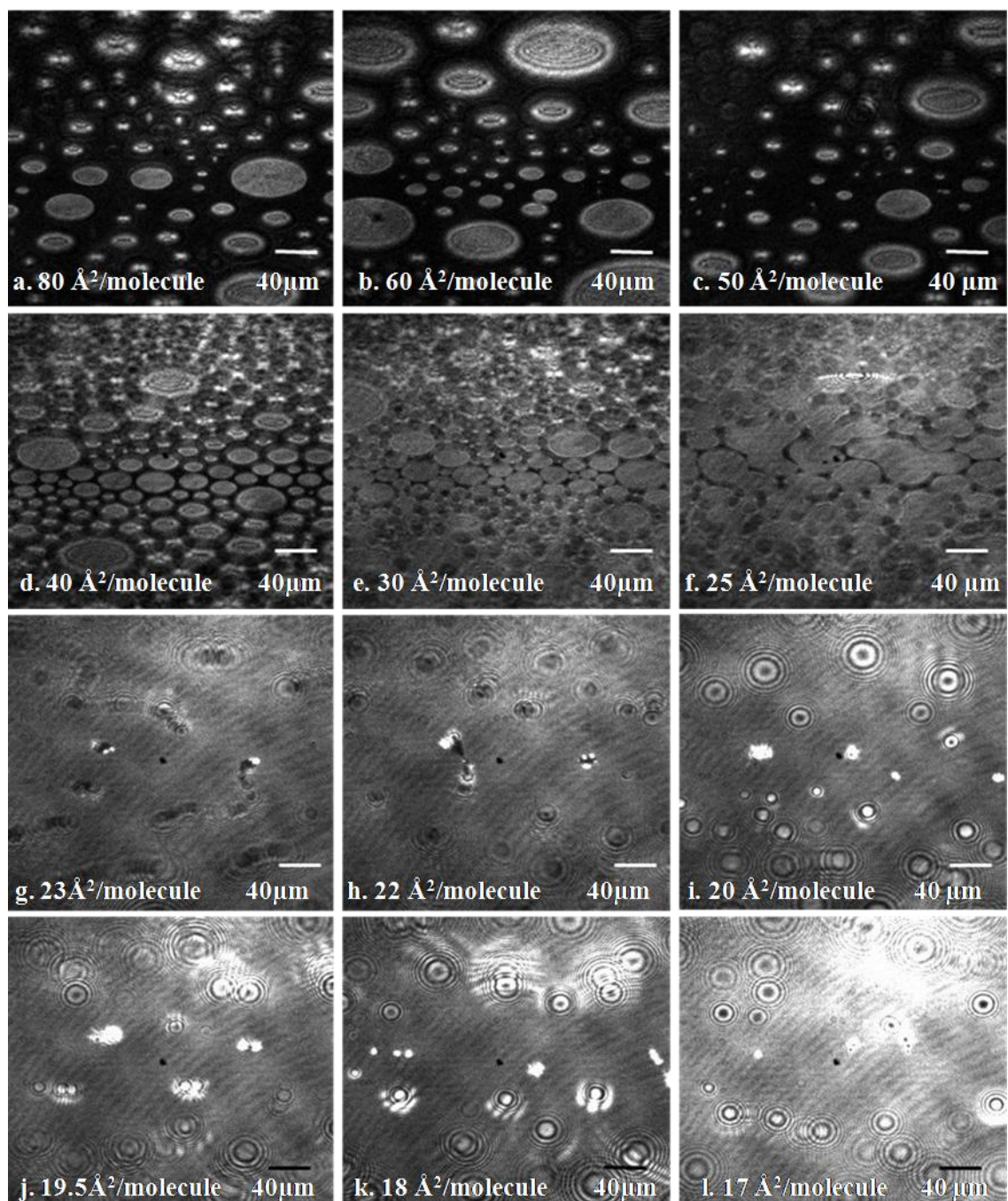


Figure 4.6 BAM Images of PA on physiological buffer subphase at 24°C and total barrier compression speed rate of $5 \text{ mm}/\text{min}$.

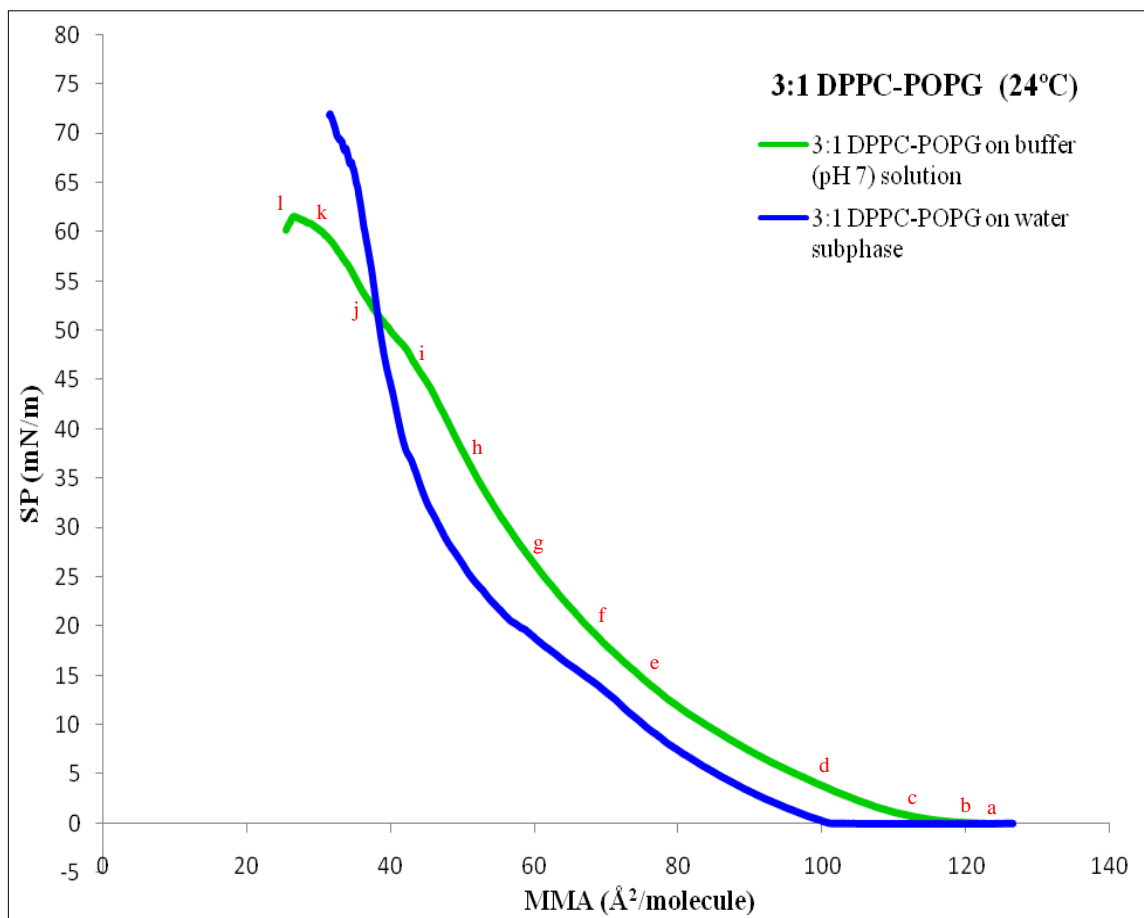


Figure 4.7 Surface pressure-area isotherm of DPPC-POPG on water subphase and on physiological buffer solution at 24°C.

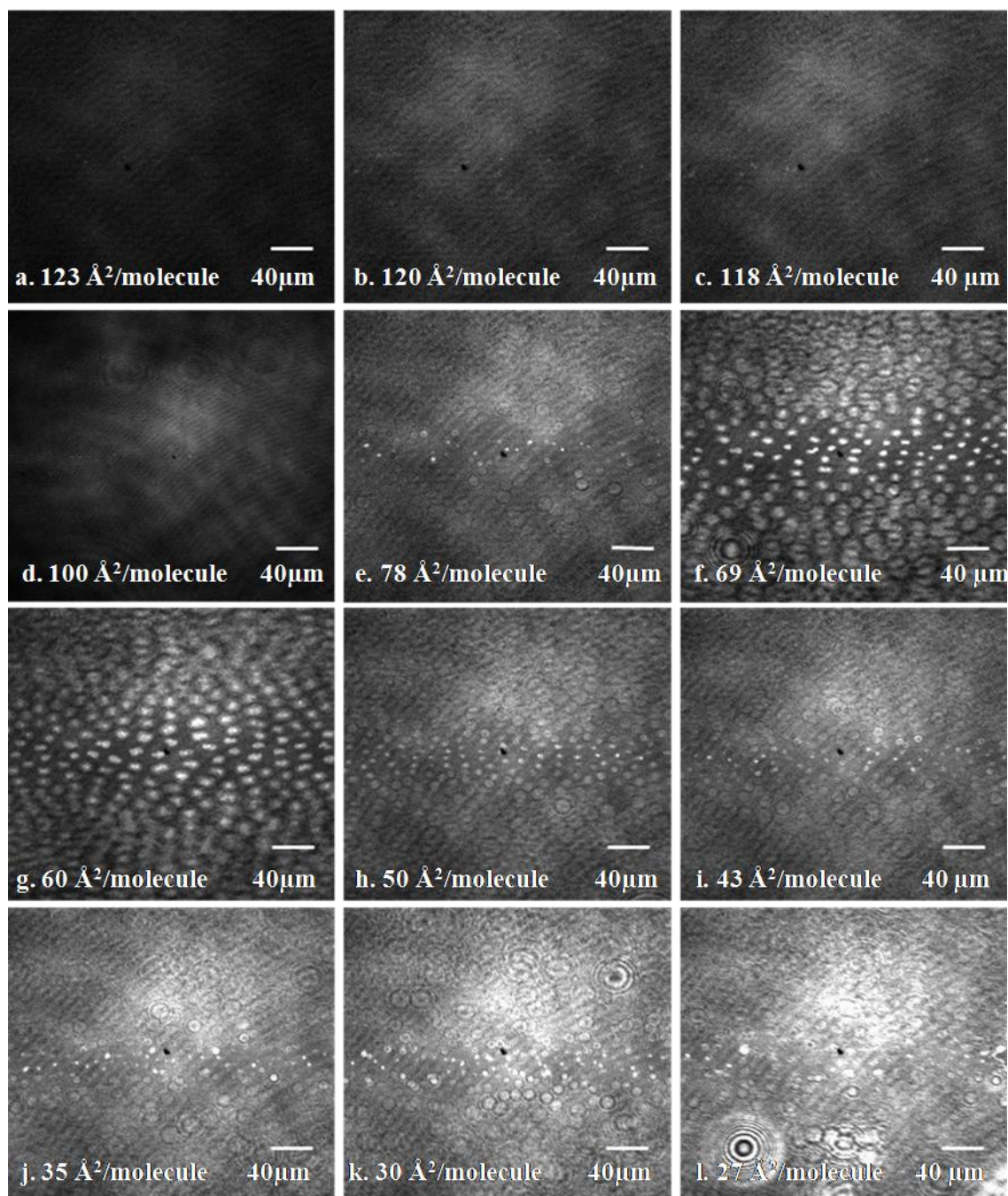


Figure 4.8 BAM Images of 3:1 DPPC-POPG on physiological buffer subphase at 24°C and total barrier compression speed rate of 5 mm/min.

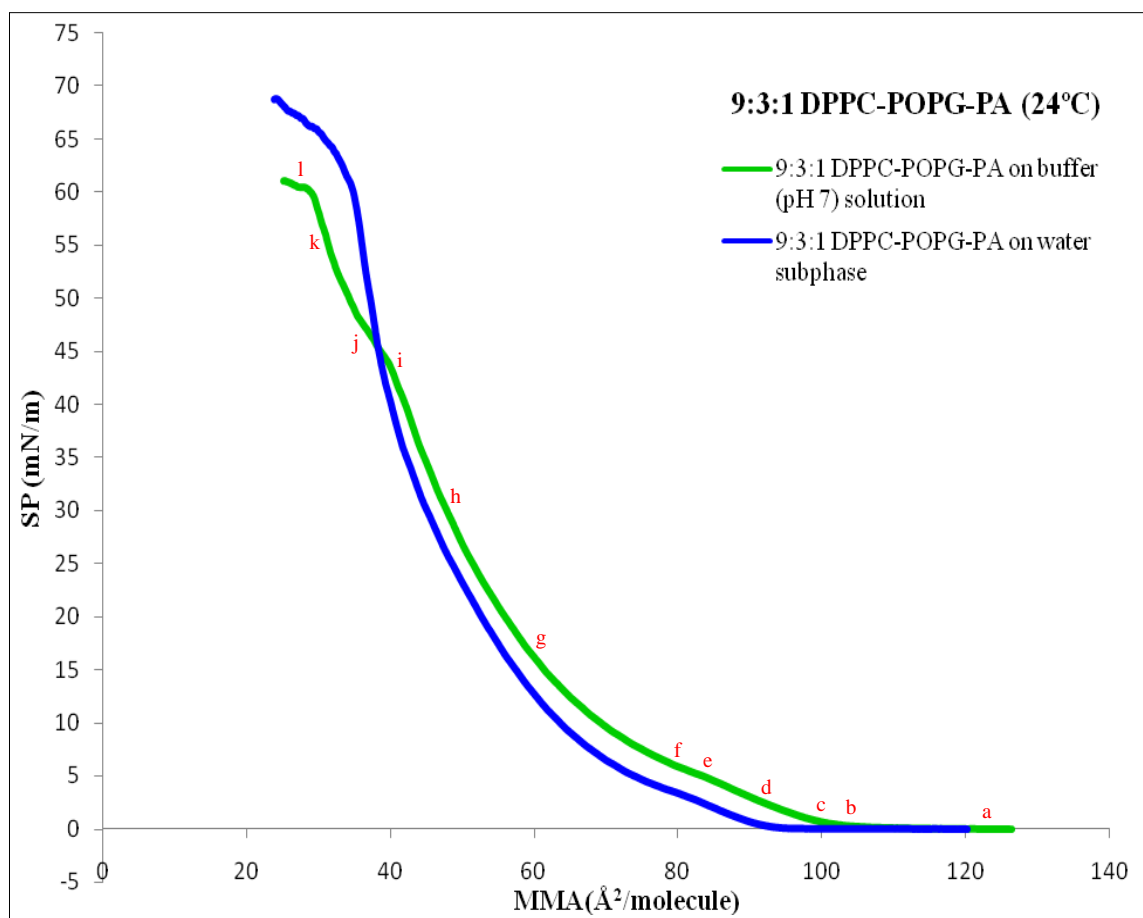


Figure 4.9 Surface pressure-area isotherm of DPPC-POPG-PA on water subphase and on physiological buffer solution at 24°C.

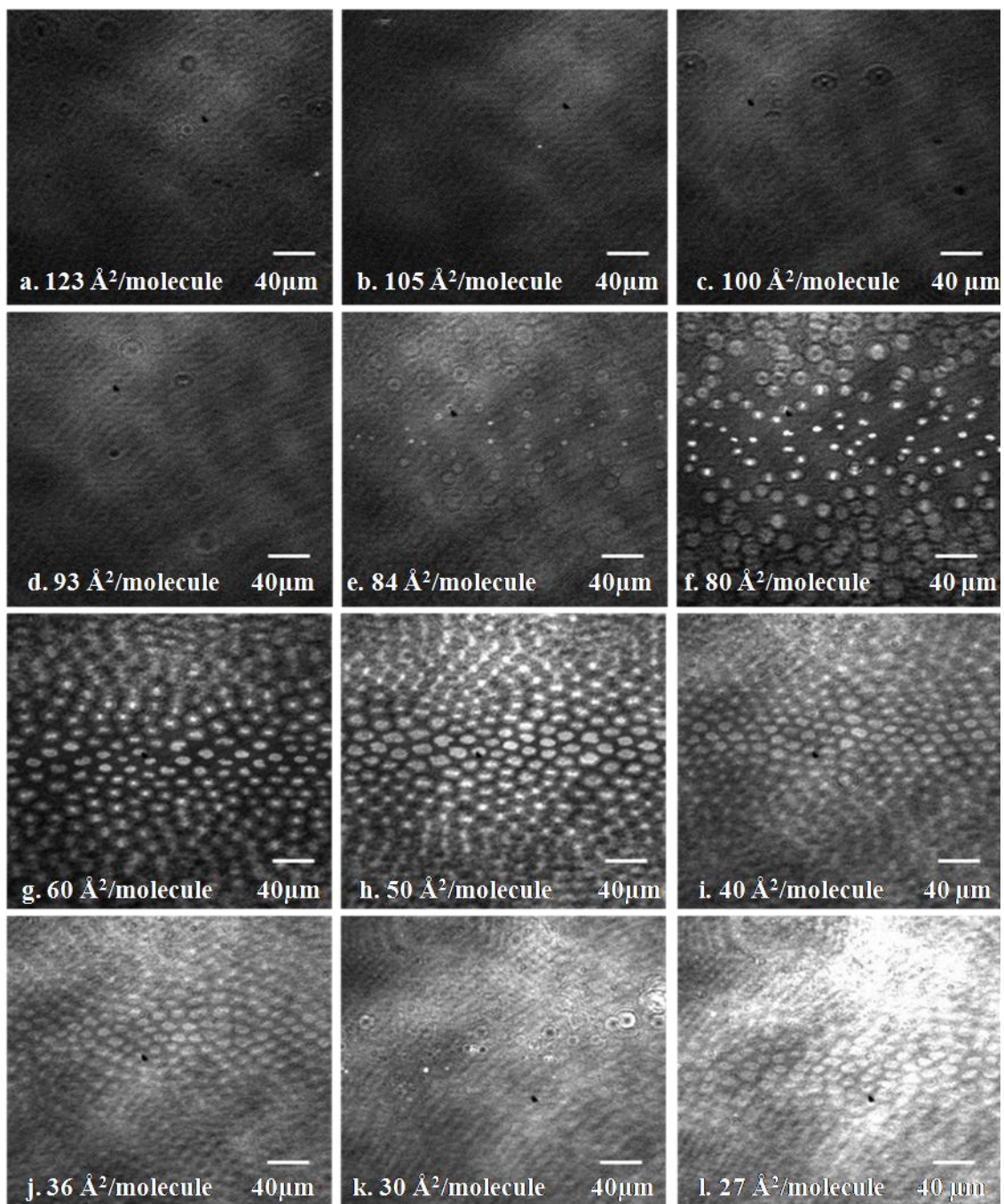


Figure 4.10 BAM Images of 9:3:1 DPPC-POPG-PA on physiological buffer subphase at 24°C and total barrier compression speed rate of 5 mm/min.

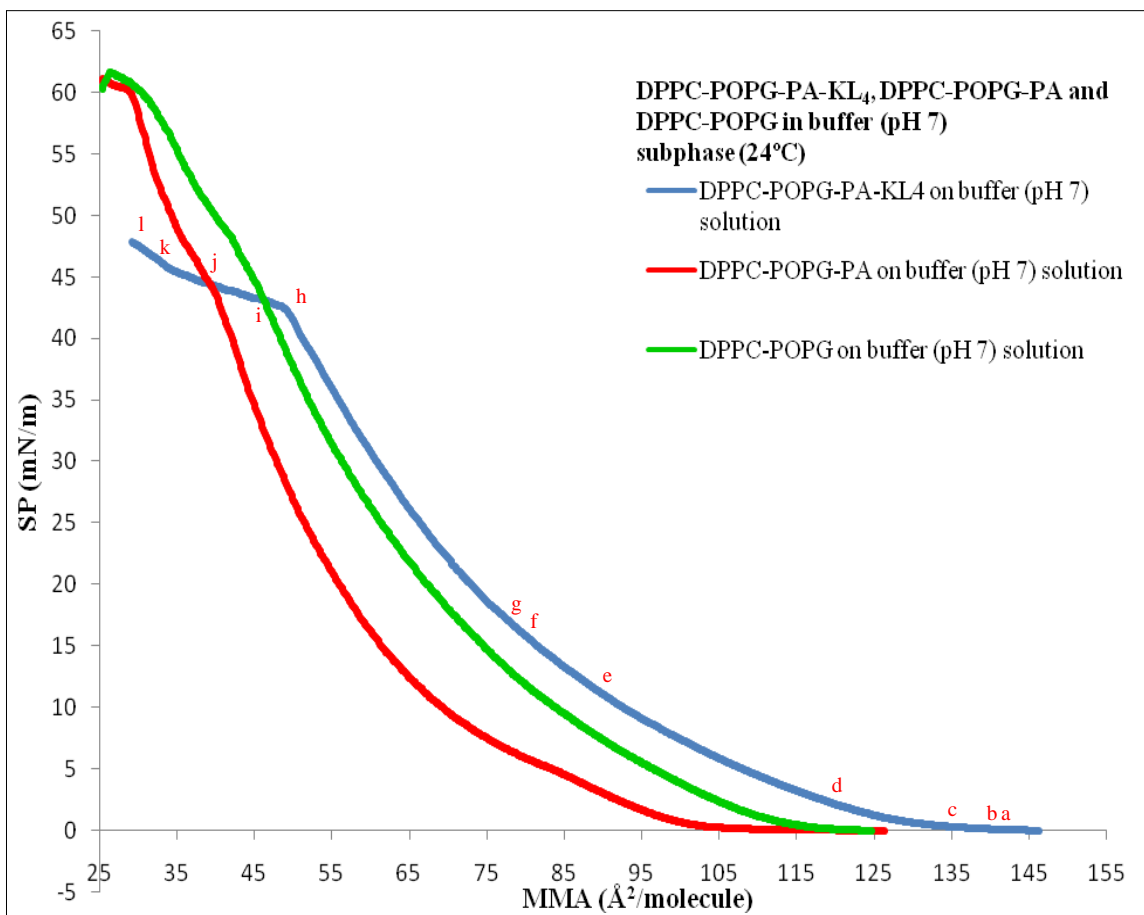


Figure 4.11 Surface pressure-area isotherms of DPPC-POPG-PA-KL₄ (66/22/7/5 by weight ratio), DPPC-POPG-PA and DPPC-POPG on physiological buffer solution at 24°C.

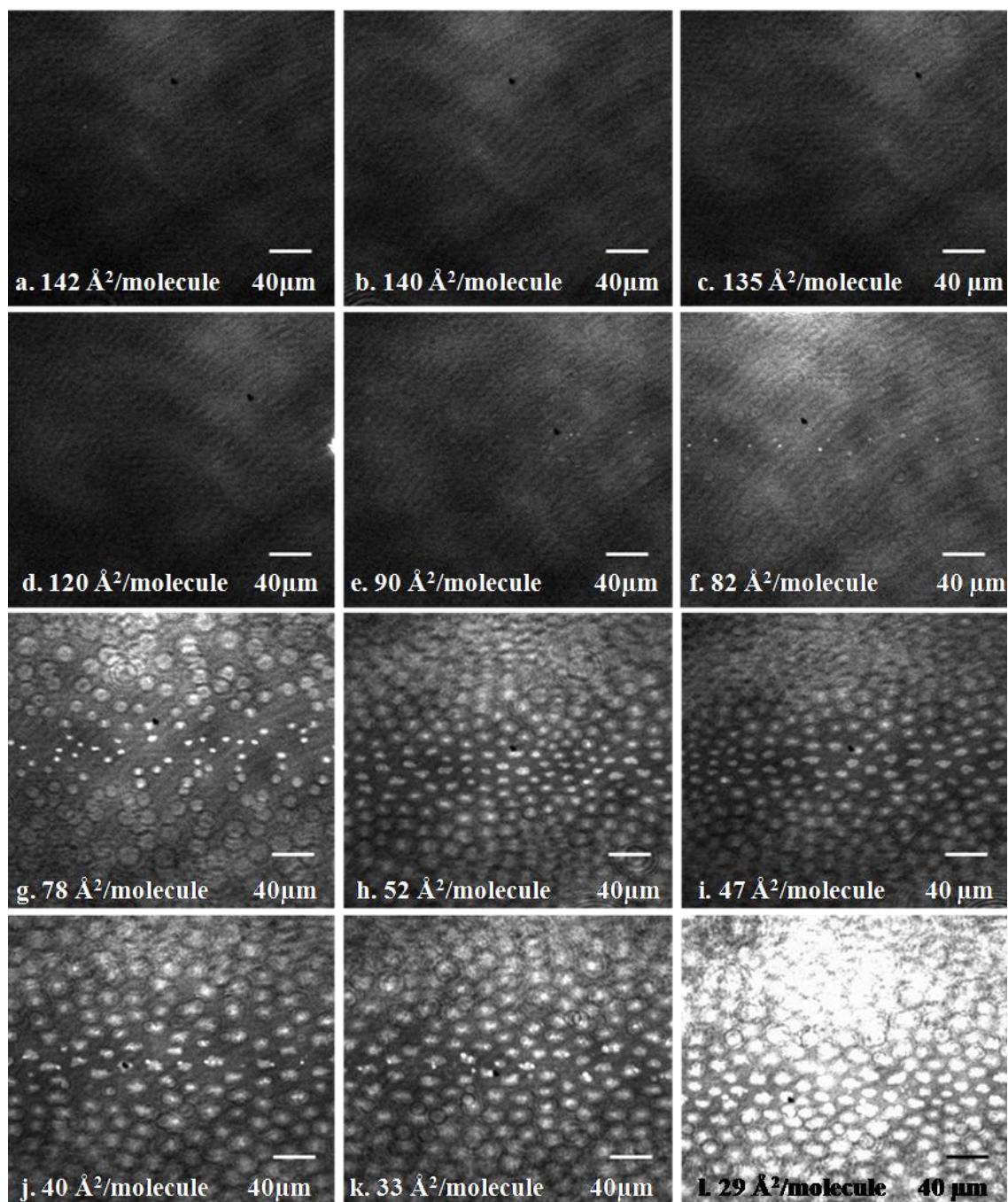


Figure 4.12 BAM Images of DPPC-POPG-PA-KL₄ on physiological buffer subphase at 24°C and total barrier compression speed rate of 5 mm/min.

CHAPTER 5

CONCLUSION AND RECOMMENDATIONS

The ability of the lungs to function normally as an organ for respiration can be rooted back to the physiological and molecular aspects of the lungs. Natural lung surfactants reduce the surface tension in the alveoli preventing their collapse and maintaining a large surface area for an easy access of oxygen to enter the bloodstream. Without these surfactants, surface tension builds up which causes the alveoli to collapse and consequently prompts the lungs to become stiff. This situation would entail a huge amount of pressure to enable easy exchange of oxygen and carbon dioxide.^{166,167}

The attainment of low surface tension in the lungs is caused by the presence of a high quantity of DPPC (41-70%) in endogenous lung surfactants. The presence of other components such as unsaturated phospholipids and hydrophobic proteins, promote and sustain the poor adsorption and spreading of DPPC in the dynamic cycle of inhalation and exhalation.^{9,83}

The results presented in this work demonstrate the behavior of the different lung surfactant model systems on water and physiological buffer subphase acquired through surface pressure-area isotherm and Brewster angle microscopy. The monolayers formed by various individual and mixed lipids and fatty acid behave differently at different

subphase at room temperature of $23 \pm 1^\circ\text{C}$. Romao and co-workers¹⁴³ have pointed out that it is expected for the morphology of the mixed monolayers to vary with the surface pressure and composition as the morphology and texture of single-chained components of lung surfactants significantly vary from that of DPPC monolayers. Even more, no universally accepted surfactant composition has been formulated since the make-up of native surfactants changes significantly from one species to another subsequently leading to the disparity in the structure and composition of replacement lung surfactants.^{7,54,151}

In spite of such variations, difficulties and complex nature of native lung surfactants, worthy studies of model lung surfactant mixtures can be made as these simple mixtures of lung surfactants proved to be beneficial^{158,165} especially in life threatening lung-related diseases such as neonatal and adult respiratory distress syndromes. Several replacement surfactants are in current use worldwide, such as Infasurf, Survanta, Curosurf, Exosurf, ALEC among others and each has specific lipid and protein composition and formulation depending on the source. Such heterogeneity of replacement lung surfactant compositions are brought about by the urge to develop an optimum formulation and although current available lung surfactant perform effectively their long-standing drawbacks induce calls for improvement.³

The experimental findings in this thesis generally agreed with other studies cited in Chapters 3 and 4 that have used different formulations of lung surfactant model systems and have employed fluorescence microscopy. The BAM images and surface pressure-area isotherms rather illustrate the behavior of individual and mixed lung surfactant components in vitro. Interesting shapes and domain formation of BAM images

were correlated and interpreted alongside their corresponding surface pressure-area isotherms. General phenomena, such as condensation and fluidization of lung surfactant components and effects of other variables such as subphase composition in the behavior of lung surfactant components have been successfully observed and accounted for.

Further development in the design, imaging component and optical requirements of the Brewster angle microscope will be beneficial in the analysis of valuable interfacial parameters and monolayer information such as thickness, density, anisotropy and molecular tilt angle. Particularly, an analyzer (essentially a polarizer) can be added in the path of the imaging optics to help eliminate stray reflections and improve the contrast of images.^{21,22,33,34,57} Also, a CCD camera with a high speed video frequency scanning mode and better infinity-corrected industrial objective lens with higher numerical aperture are recommended.

A more quantitative approach in elucidating the structure-function relationships of the shapes and domain formation in the images acquired through Brewster angle microscopy is hereby recommended. Understanding the functions and physicochemical properties of lung surfactant compositions through structural analysis in the BAM images could shed insights in the elucidation of the mechanism of lung surfactant component and ultimately, in designing optimum formulation of replacement lung surfactants.

APPENDIX A

BREWSTER ANGLE MICROSCOPY IMAGES AND SURFACE PRESSURE- AREA ISOTHERMS OF OTHER LUNG SURFACTANT MODEL SYSTEMS ON WATER SUBPHASE

The following data are BAM and surface pressure-area isotherms of other lung surfactant model systems on water subphase at 24°C. The first mixture presented below is 1:1 DPPC-PA. The different phase transitions assigned for PA's isotherm in water are also observed in this mixture which are namely G-TC (tilted condense) phase, TC (tilted condense) phase, UC, and Collapse phase.

The DPPC-Tripalmitin mixed monolayer system was studied by Ma and Allen¹¹ to better understand film metastability. It is said that lung surfactant maintains a metastable state during breathing since *in vivo*, lung surfactant monolayers can sustain high surface pressure environment for extended period without collapsing in static lungs. It was shown that film metastability through intermolecular interaction of DPPC with Tripalmitin is enhanced. The behavior of individual Tripalmitin in Langmuir monolayer is also observed and presented.

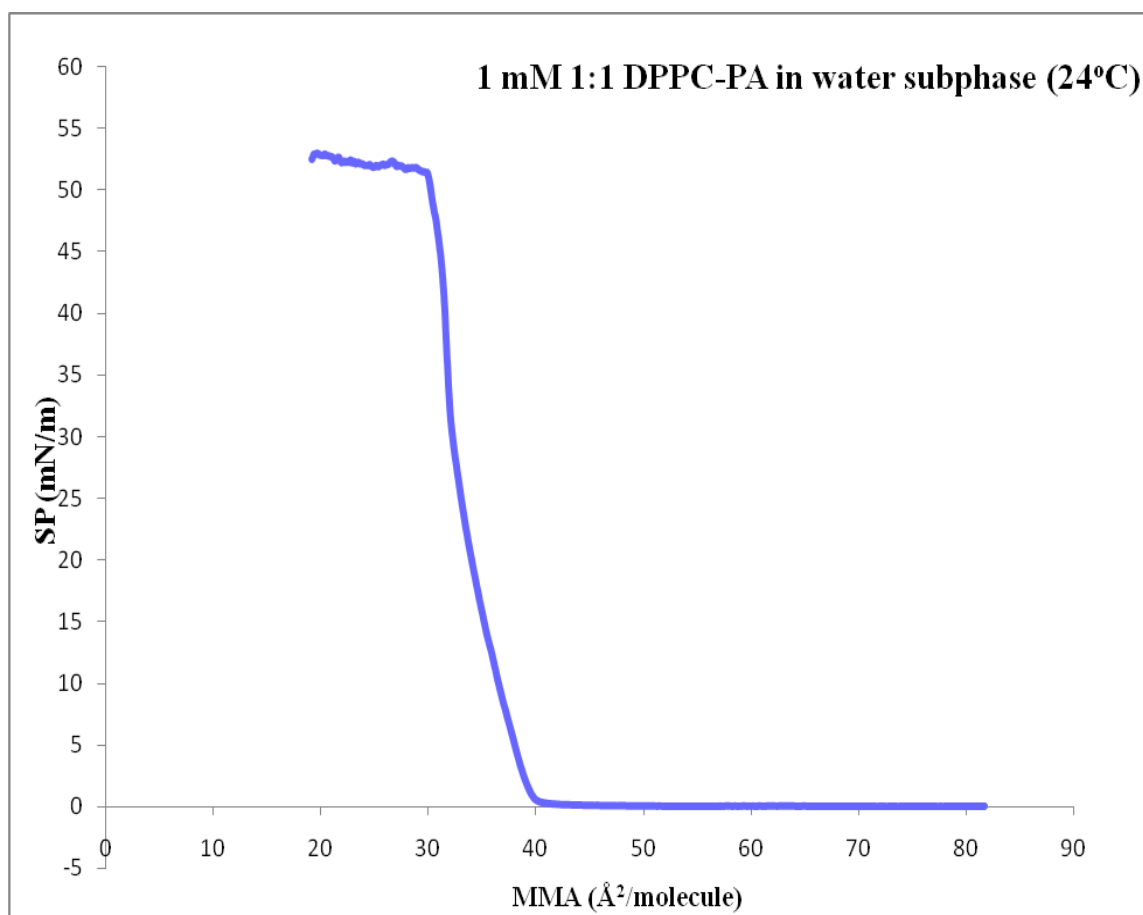


Figure A.1 Surface pressure-area isotherm of 1:1 DPPC-PA on water subphase.

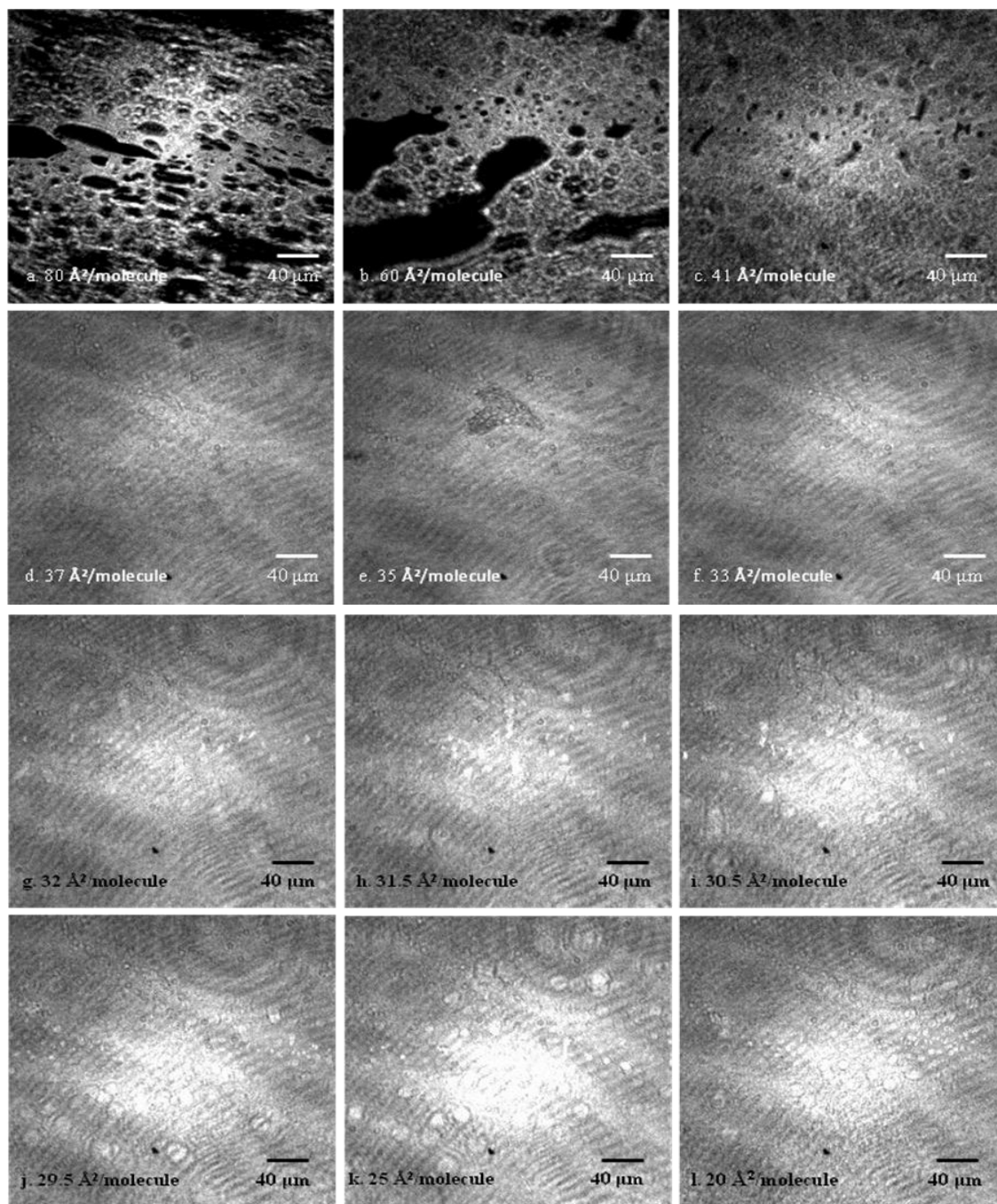


Figure A.2 BAM Images of 1:1 DPPC-PA on water subphase at 24°C and total barrier compression speed rate of 5 mm/min .

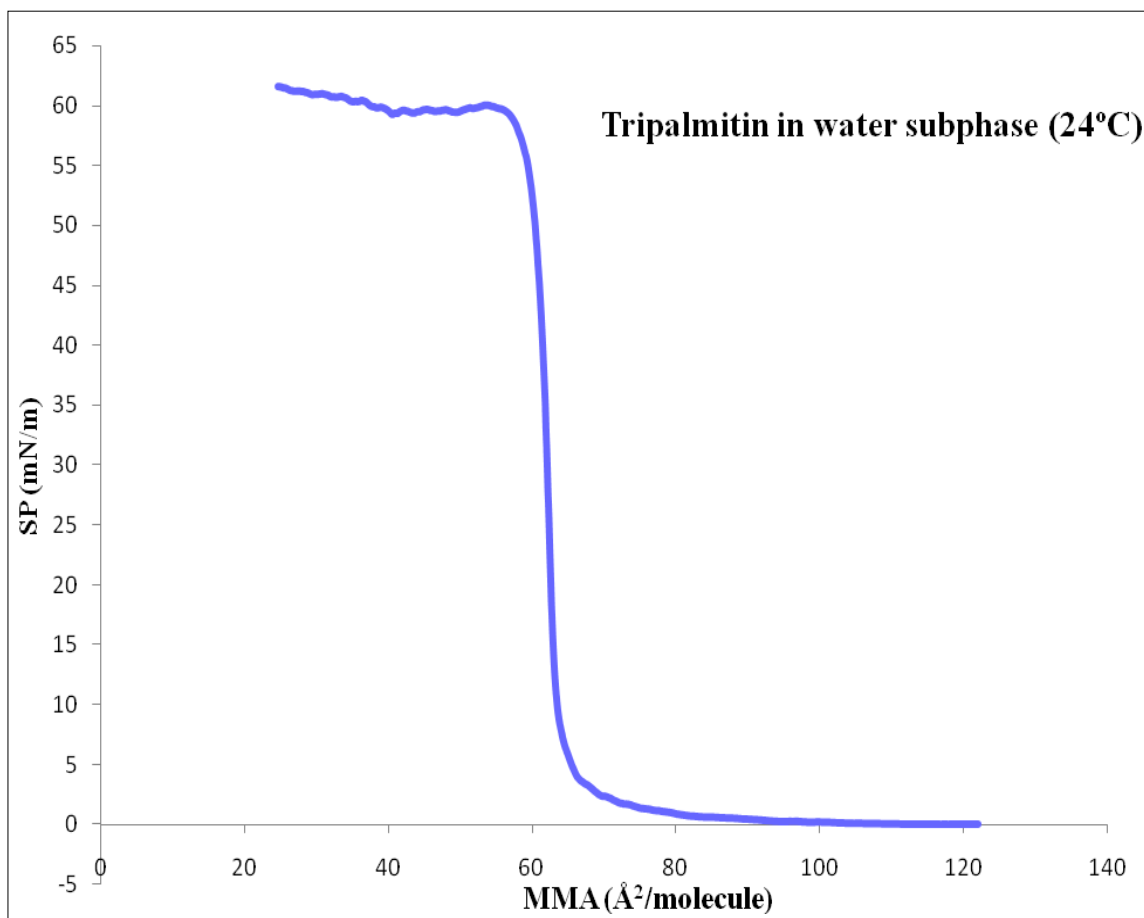


Figure A.3 Surface pressure-area isotherm of Tripalmitin on water subphase.

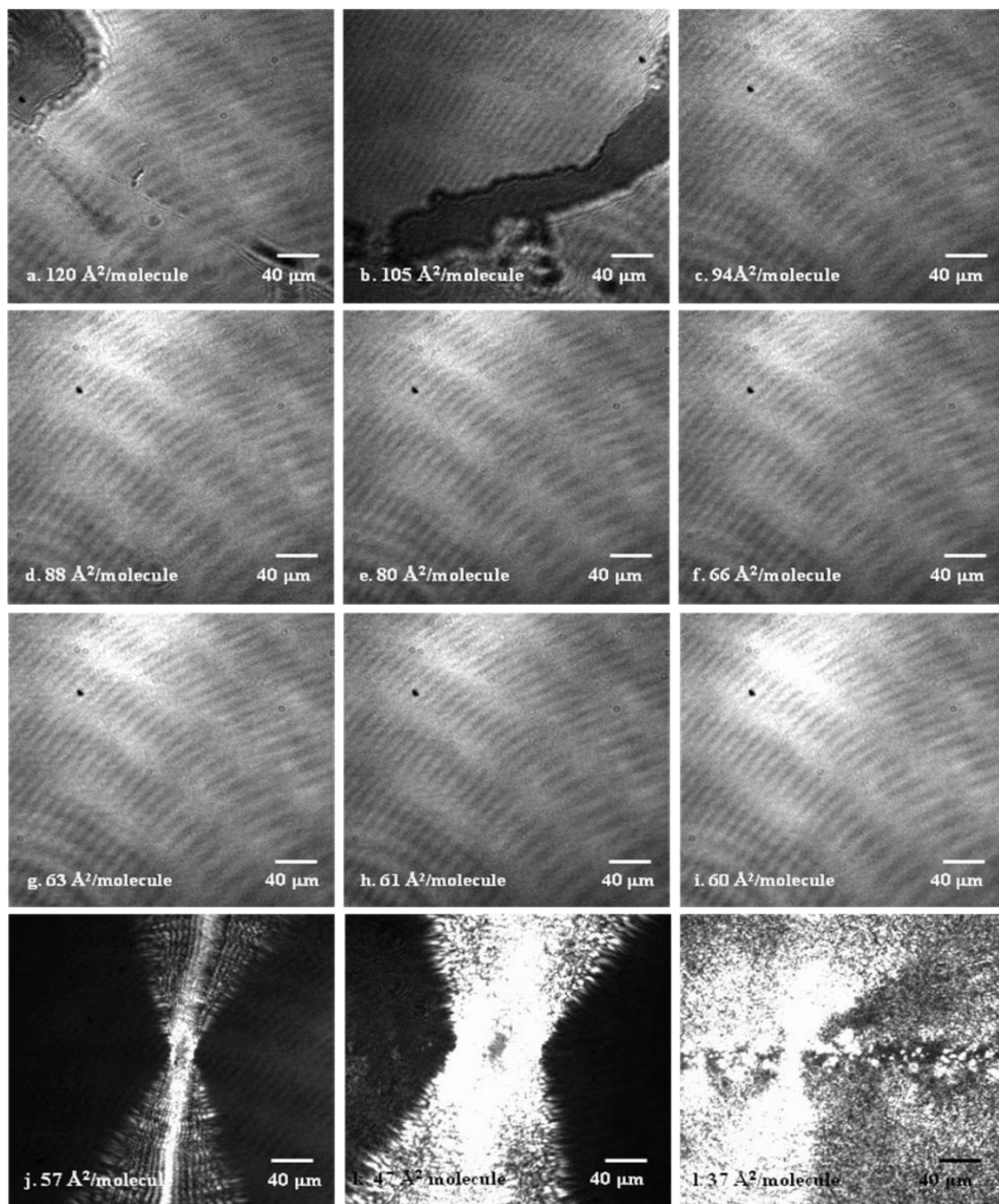


Figure A.4 BAM Images of Tripalmitin on water subphase at 24°C and total barrier compression speed rate of 5 mm/min.

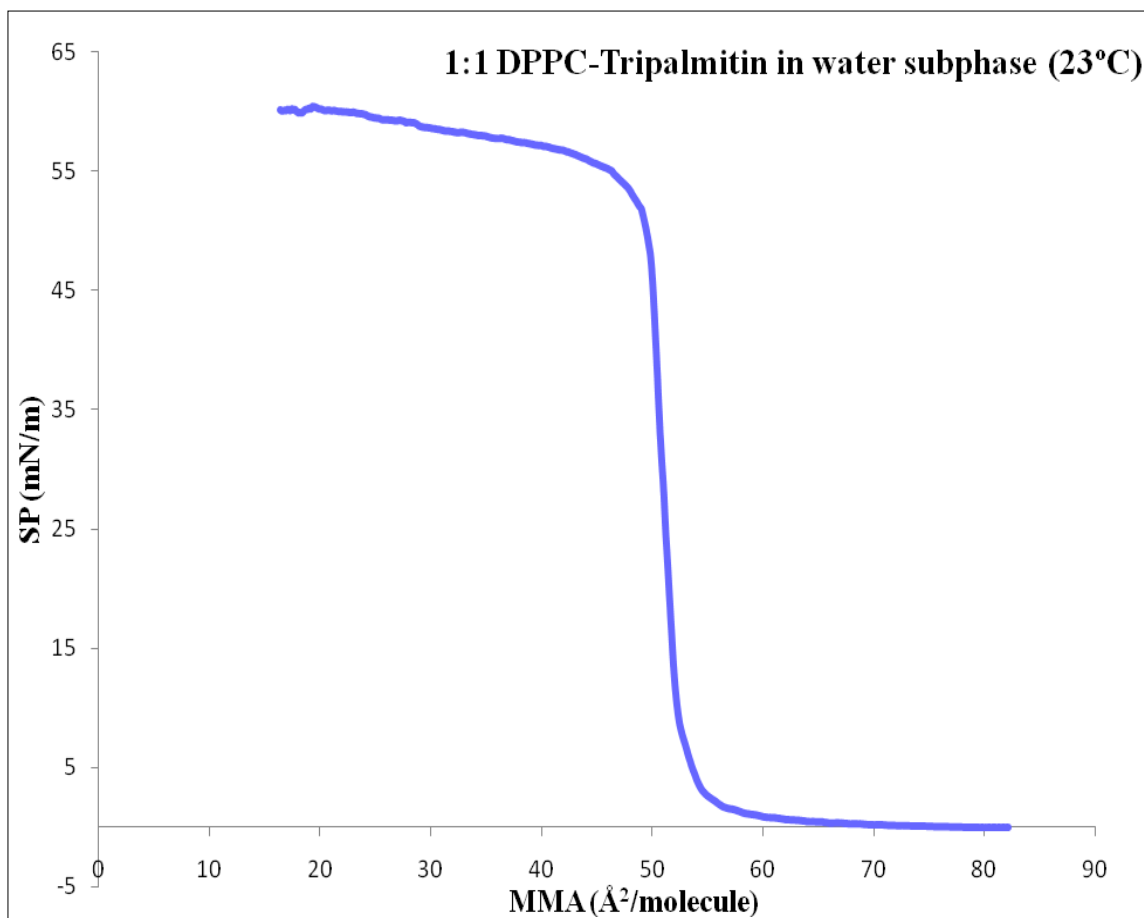


Figure A.5 Surface pressure-area isotherm of 1:1 DPPC-Tripalmitin on water subphase.

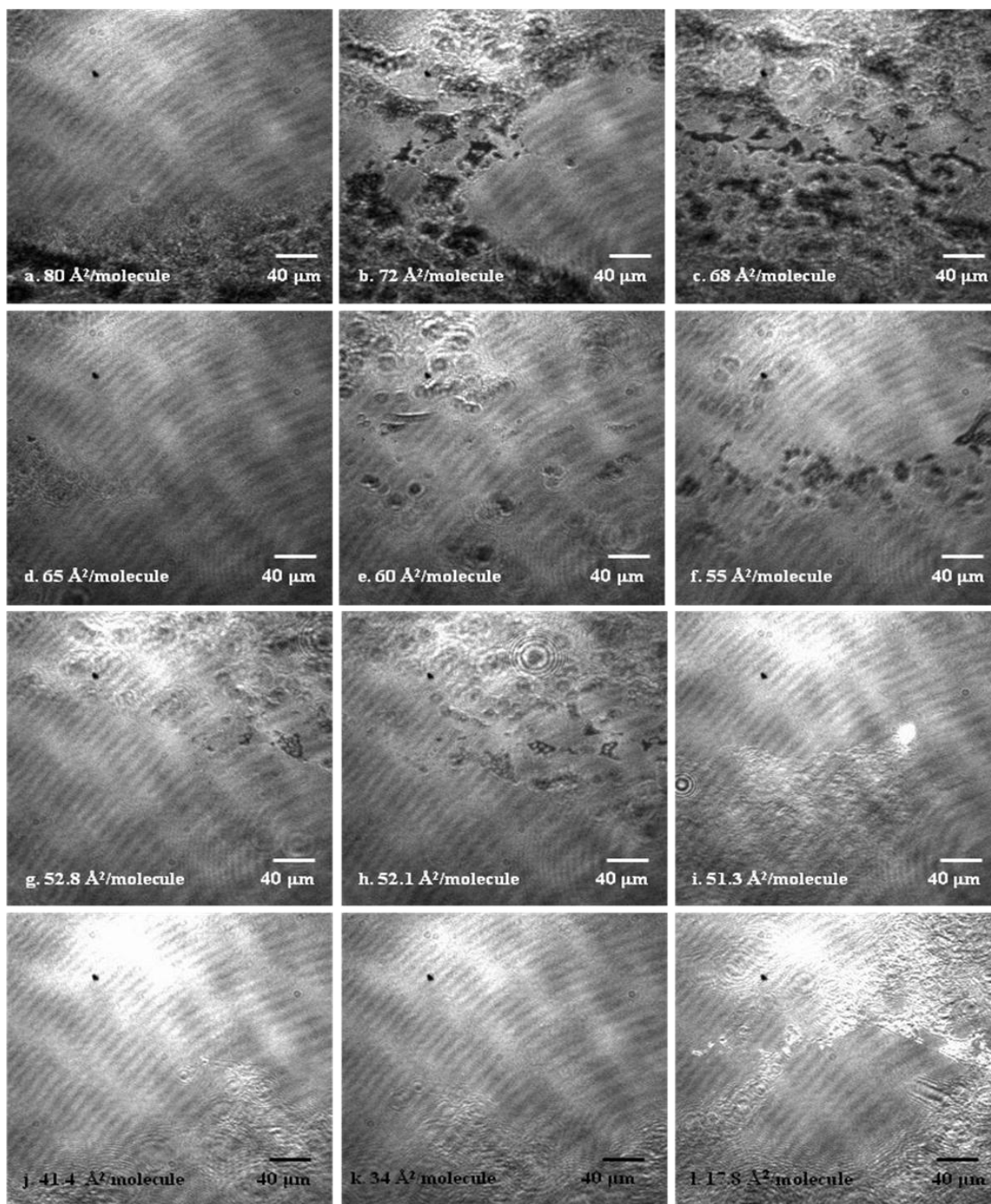


Figure A.6 BAM Images of 1:1 DPPC-Tripalmitin on water subphase at 24°C and total barrier compression speed rate of 5 mm/min.

APPENDIX B

GUIDELINES ON BREWSTER ANGLE MICROSCOPE IMAGE ACQUISITION USING THE ANDOR SOLIS SOFTWARE

At the start of any image acquisition, the following has to be secured: the CCD temperature has cooled down -50°C and the He-Ne laser has initialized. It takes about 30-45 minutes for the CCD to cool down and about 30 minutes for the laser to initialize and discharge a 100% maximum power output.

To carefully switch the power on the He-Ne laser:

1. Unplug the remote interlock connector from the HCU power supply. This will guarantee that no laser beam will come out from the laser head once it is switch on.
2. Plug the high voltage power cord cable from the control box into an electrical outlet.
3. Apply power on the laser by switching the key in front of the HCU power supply. The emission indicator on the front panel will light up to warn of eminent laser emission.

4. When ready to take an image, plug the remote interlock connector into the HCU power supply and laser beam will be emitted from the laser head.
5. After taking images, switch the key in the HCU power supply box to “off” position to safely turn off the laser.

To initialize and operate the CCD and run the controller software:

1. Open the Andor-Solis icon found on the desktop of the BAM computer as the main window is the entry point to the system.
2. To cool down the temperature of the CCD, launch the temperature control dialog box by selecting the Temperature option on the *Hardware* menu or by clicking the *Thermometer* icon at the bottom of the *Main Window* (see Figure B.1).

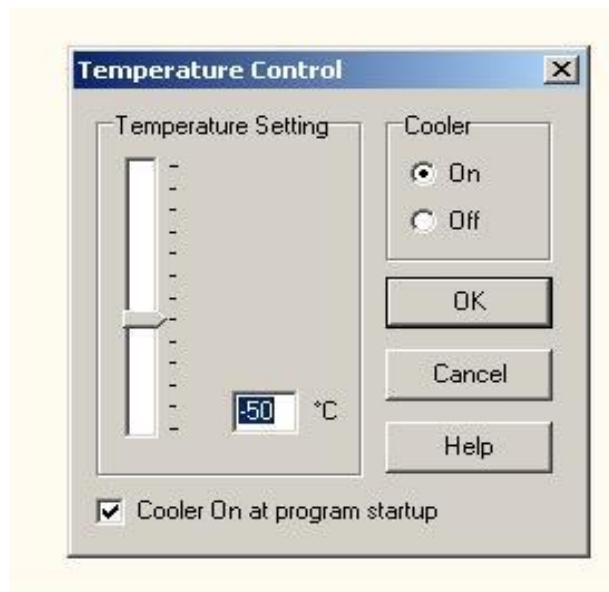


Figure B.1 Temperature control dialog box.

3. Select “on” in the Cooler box and set the *Temperature Setting* to -50°C and click *OK* button.
4. While waiting on the temperature to cool down, set the shutter control by launching the *Shutter Control* dialog box from the *Hardware* dropdown menu (see Figure B.2).

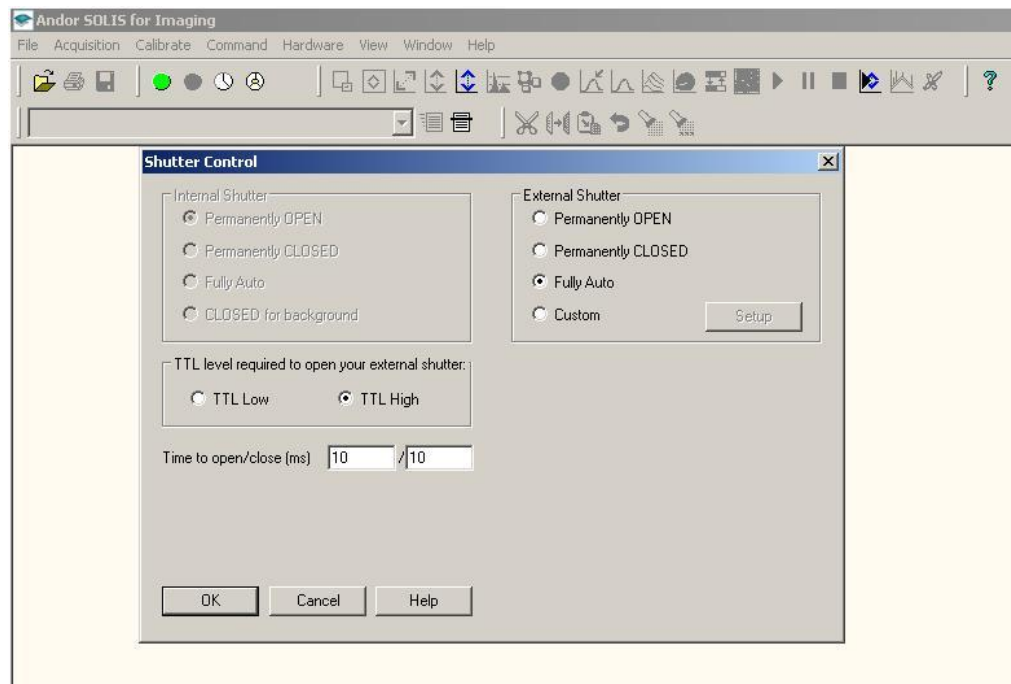


Figure B.2 Shutter control dialog box.

5. The CCD is equipped with an external shutter so in the *External Shutter* in the *Shutter Control* dialog box in Figure B.2, select *Custom* and click on the *Setup* button. A *Custom Settings* window (Figure B.3) will be launched. In this window,

choose *Closed (normal)* mode in the *During Background* box while click on the *Auto (normal)* option at *All other times* box. Hit ok at once.

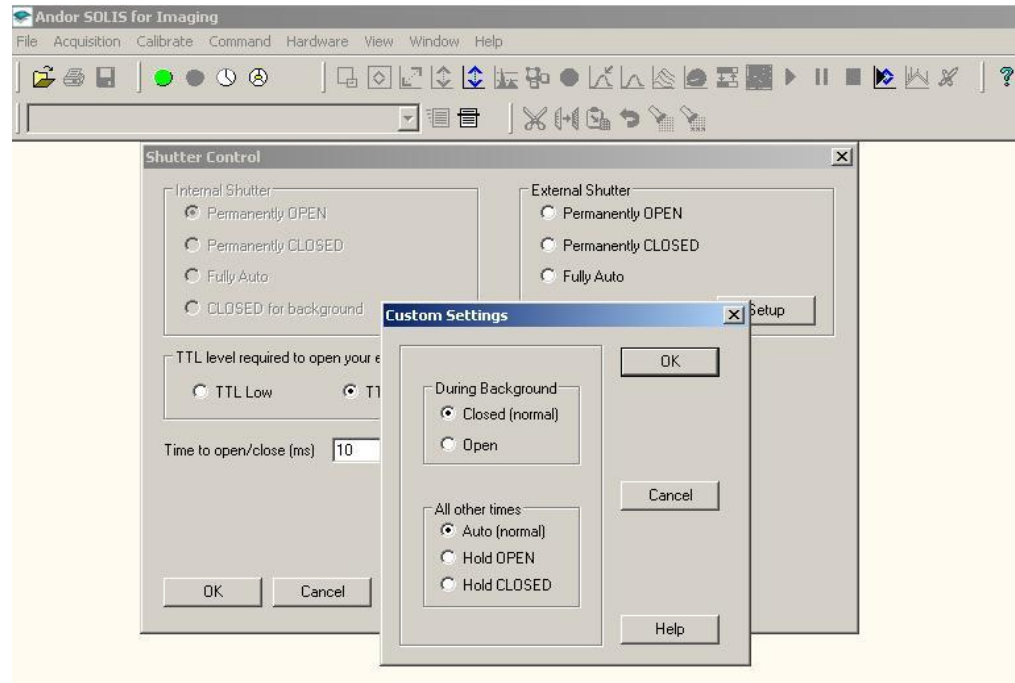


Figure B.3 Custom Setting dialog box of External Shutter control.

6. Still in the *Shutter Control* dialog box, under the *TTL level required to open your shutter*, choose the *TTL high* option and input 10/10 in the *Time to open/close (ms)* window. Click *OK* button in *Shutter Control* dialog box once everything is secured.
7. To set-up the acquisition parameters, click on the *Acquisition Menu* on the *Main Window* and choose the *Setup Acquisition* option from the dropdown menu. The *Setup Acquisition* window is shown in Figure B.4.

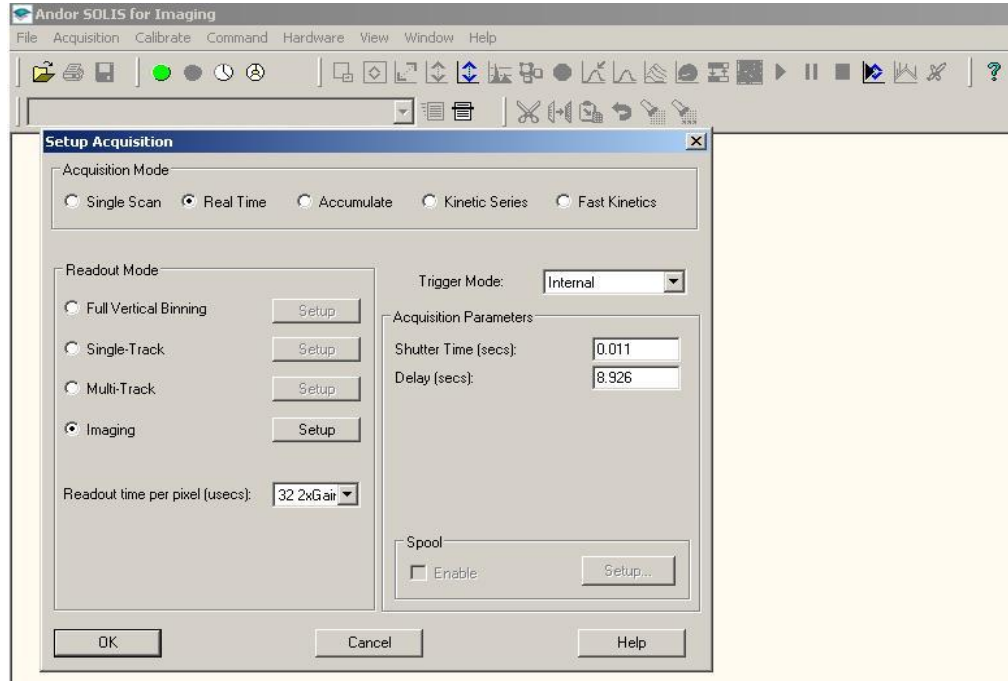


Figure B.4 Setup Acquisition dialog box.

8. In the *Setup Acquisition* window, under the *Acquisition Mode*, the *Single Scan* option can be selected when focusing and positioning the image at the center of the CCD viewing window. The *Real Time* option, on the other hand, can be selected during the actual experiment for a continuous acquisition of images.
9. In the *Readout time per pixel (usecs)* dropdown menu, choose the *32 2xGain* parameter and default settings will automatically be keyed-in the *Acquisition Parameters* box.

10. Still in *Setup Acquisition* window, choose *Imaging* in the *Readout Mode*. Click on the *Setup* button to launch the *Imaging* dialog box (Figure B.5). In this window, choose the *Full Resolution Image* option and hit the *OK* button.

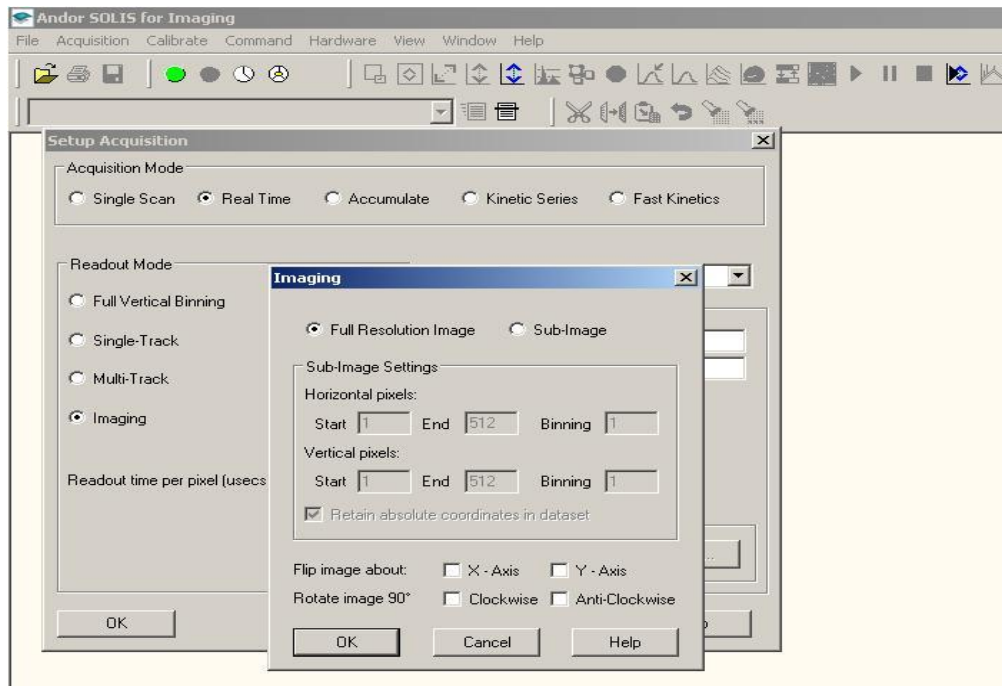


Figure B.5 Imaging dialog box.

11. Once everything is arranged in the *Setup Acquisition* window, click the *OK* button for the changes to take effect.
12. In taking any images, the type of data to be acquired also has to be established. To do so, click the *Acquisition* dropdown menu from the *Main Window* and choose *Data Type* (Figure B.6). In this window, choose *Counts (Bg corrected)* and then hit the *OK* button.

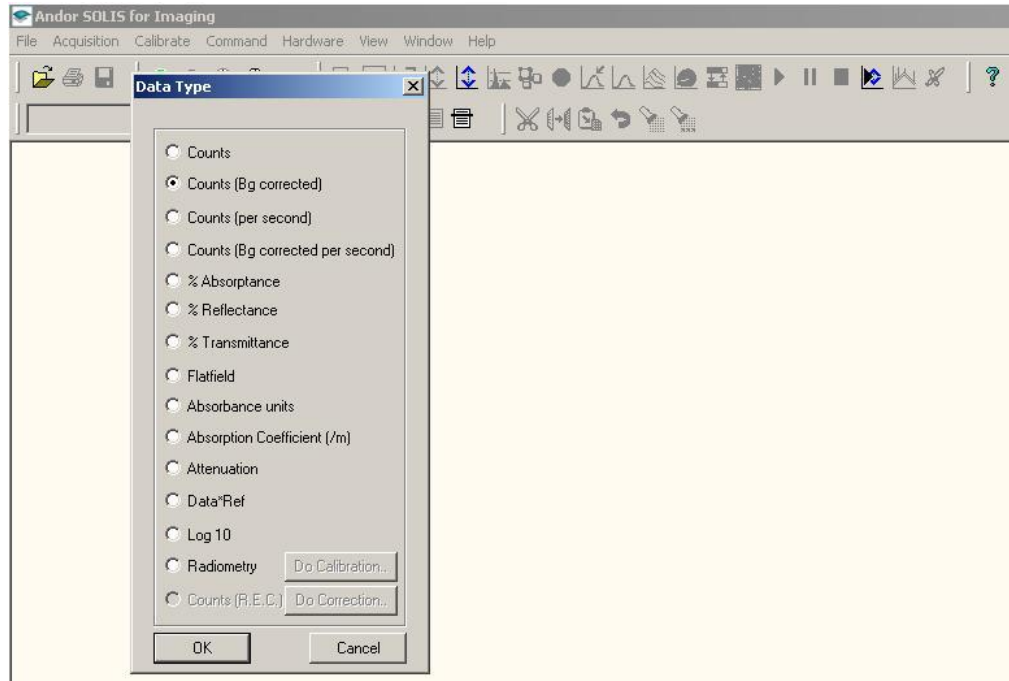


Figure B.6 Data Type dialog box.

13. To start taking images, a background image has to be acquired first so that the dark signal can be subtracted from the actual image. To do so, hit the *Acquisition* mode in the *Main Window* and click on the *Take Background* and a background image is then captured (Figure B.7)

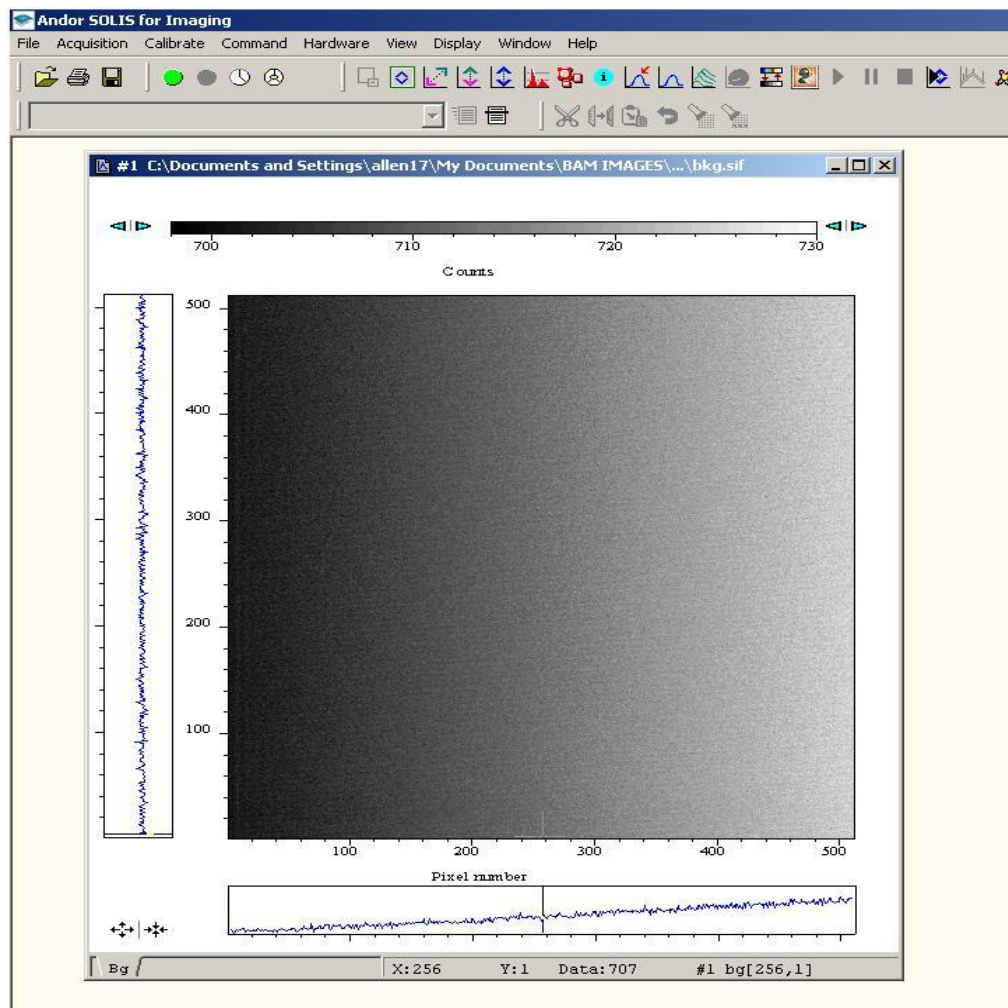


Figure B.7 Acquisition of a Background Image.

14. Once a background image is acquired, sample images can now be taken by clicking on the *Acquisition* menu and choosing the *Take Image* on the selection. Another option is clicking on the green button in the *Main Window*. Images are now manually (*Single Scan*) or automatically (*Real Time*) acquired (see step 8) when the *Take Image* or green button is pressed.

15. The capture image can be rescaled in terms of its contrast. To do so, click on the *Display* tab in the *Main Window*. From the selection, choose *Rescale Data Mode* and in the dropdown menu, choose *Custom* mode (see Figure B.8).

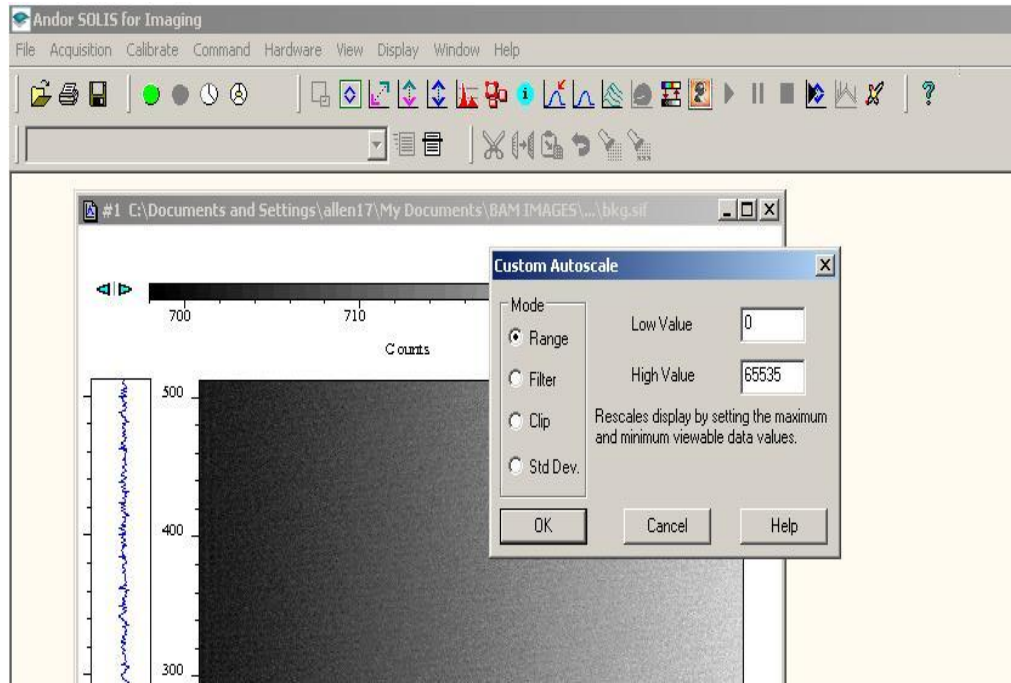


Figure B.8 Rescale Data Mode and Custom Mode Selection.

16. In the *Custom Autoscale* window (Figure B.8) choose the *Range* option under the *Mode* and assign values for the *Low Value* and *High Value* windows. Usually, in the *Low Value* window, 0 (zero) is placed and in *High Value* window, it varies from 50-400, depending on the contrast of the images and the background.

17. To save the images, click *File* in the *Main Window* and choose *Save As...* option.

A *Save As* window will be shown and type-in the file name of the image to be saved in a folder pre-designated.

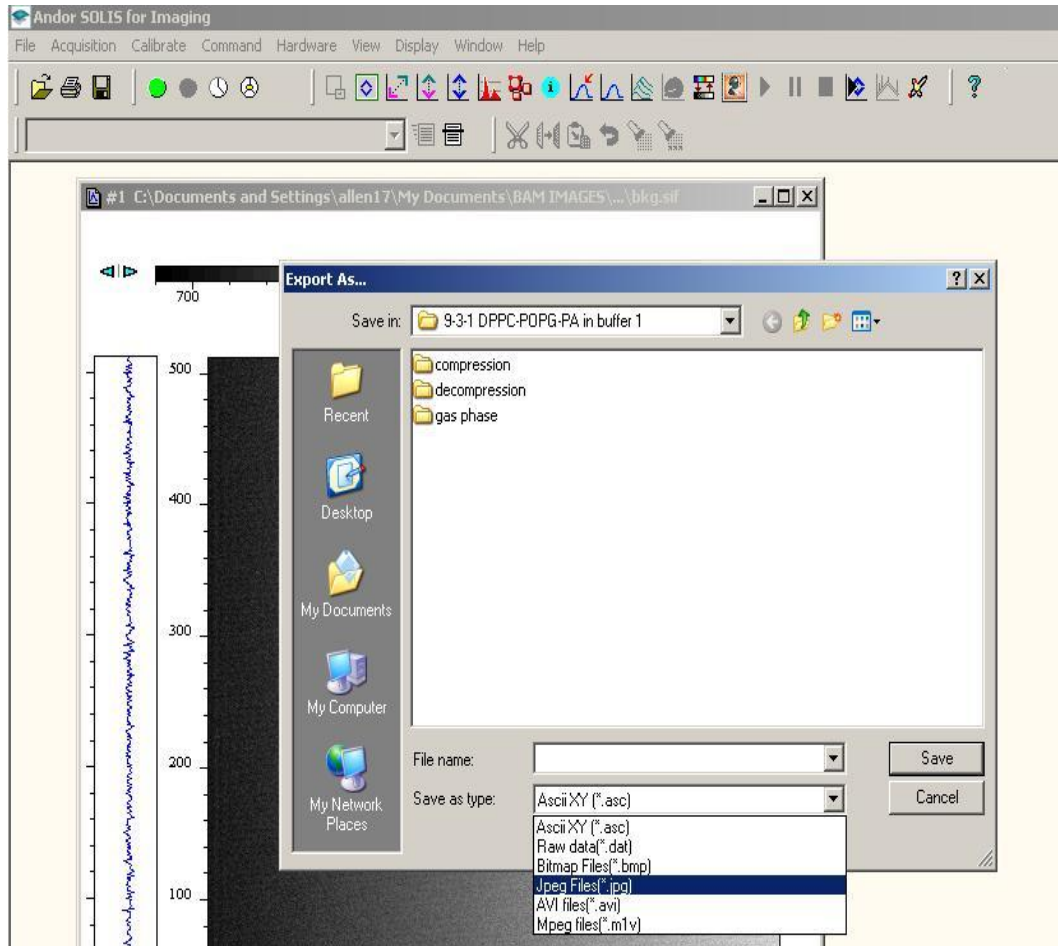


Figure B.9 Export As dialog box.

18. To export an image from the .sif data file to .jpg (JPEG) or .bmp (Bitmap) data files, choose *Export As...* on the *File* menu. An *Export As...* window will show up (Figure B.9) and then choose from the *Save as type* dropdown menu the types

of data file the image can be saved with. Saving the images in .jpg or .bmp data types is convenient because the images can be retrieved even without launching the Andor-Solis software.

REFERENCES

1. Haagsman, H. P. and van Golde, L. M. G. Lung surfactant and pulmonary toxicology. Lung. **1985**. 163:275-303.
2. Creuwels, L. A. J. M., van Golde, L. M. G. and Haagsman, H. P. The pulmonary surfactant system: Biochemical and clinical aspects. Lung. **1997**. 175:1-39.
3. Nalwa, H. S. (Ed.) Handbook of nanostructured biomaterials and their applications in nanobiotechnology. Vol. 1. California: American Scientific Publishers. **2005**.
4. Martinez-Gil, L., Perez-Gil, J. and Mingarro, I. The surfactant peptide KL₄ sequence is inserted with a transmembrane orientation into the Endoplasmic reticulum membrane. Biophysical Journal: Biophysical Letters. **2008**, 95 (6): L36-L38.
5. Robertson, B., Johansson, J. and Curstedt, T. Synthetic surfactants to treat neonatal lung disease. **2000**. 6: 119-124.
6. Alonso, C., Waring, A. and Zasadzinski, J. Keeping lung surfactant where it belongs: Protein regulation of two-dimensional viscosity. Biophysical Journal. **2005**. 89: 266-273.
7. Ding, J., Takamoto, D., Nahmen, A. V., Lipp, M. M., Lee, K. Y., Waring, A. and Zasadzinski, J. Effects of lung surfactant proteins, SP-B and SP-C and palmitic acid on monolayer stability. Biophysical Journal. **2001**. 80 (5):2262-2272.
8. Alonso, C., Alig, T., Yoon, J., Bringezu, F., Warriner, H and Zasadzinski, J. More than a monolayer: Relating lung surfactant structure and mechanics to composition. Biophysical Journal. **2004**. 87:4188-4202.
9. Ma, J., Koppenol, S., Yu, H. and Zografi, G. Effects of a Cationic and Hydrophobic Peptide, KL₄, on Model Lung Surfactant Lipid Monolayers. Biophysical Journal. **1998**. 74:1899-1907.
10. Schürch, S., Goerke, J. and Clements, J. A. Direct determination of volume- and time-dependence of alveolar surface tension in excised lungs. Proceeding of the National Academy of Sciences of the United States of America. **1978**. 75 (7) 3417-3421.

11. Ma, G. and Allen, H. New insights into lung surfactant monolayers using vibrational sum frequency generation spectroscopy. *Photochemistry and Photobiology*. **2006**. 82:1517-1529.
12. Ma, G. and Allen, H. Condensing effect of palmitic acid on DPPC in mixed Langmuir monolayers. *Langmuir*. **2007**. 23:589-597.
13. Ma, G. and Allen, H. Real-time investigation of lung surfactant respreading with surface vibrational spectroscopy. *Langmuir*. **2006**. 22:11267-11274.
14. Sáenz, A., Cañadas, O., Bagatolli, L. A., Sánchez-Barbero, F., Johnson, M. E. and Casals, C. Effect of surfactant protein A on the physical properties and surface activity of KL₄ surfactant. *Biophysics Journal*. **2007**. 92:482-492.
15. Veldhuizen, R., Nag, K., Orgeig, S. and Possmayer, F. The role of lipids in pulmonary surfactant. *Biochimica et Biophysica Acta: Molecular Basis of Disease*. **1998**. 1408:90-108.
16. Durand, D. J., Clyman, R. I., Heymann, M. A., Clements, J. A., Mauray, F., Kitterman, J. and Ballard, P. Effects of a protein-free, synthetic surfactant on survival and pulmonary function in preterm lambs. *The Journal of Pediatrics*. **1985**. 107 (5), 775-780.
17. Notter, R. H. Lung surfactants: Basic science and clinical applications. New York: Marcel Dekker, Inc. **2000**.
18. Ma, G. and Allen, H. DPPC Langmuir monolayer at the air-water interface: Probing the tail and head groups by vibrational sum frequency generation spectroscopy. *Langmuir*. **2006**. 22:5341-5349.
19. Tanaka, Y., Takei, T., Aiba, T., Masuda, K., Kiuchi, A. and Fujiwara, T. Development of synthetic lung surfactants. *Journal of Lipid Research*. **1986**. 27:475-485.
20. Lösche, M. and Möhwald, H. Fluorescence microscope to observe dynamical processes in monomolecular layers at the air/water interface. *Review of Scientific Instruments*. **1984**. 55 (12):1968-1972.
21. Meunier, J. Why a Brewster angle microscope? *Colloids and Surfaces A: Physicochemical and Engineering Aspects*. **2000**. 171:33-40.
22. Hénon, S. and Meunier, J. Microscope at the Brewster angle: Direct observation of first-order phase transitions in monolayers. *Review of Scientific Instruments*. **1991**. 62 (4): 936-939.

23. Cohen Stuart, M. A., Wegh, R. A., Kroon, J. M. and Sudhölter, E. J. R. Design and testing of a low-cost and compact Brewster angle microscope. Langmuir. **1996**. 12:2863-2865.
24. Baszkin, A. and Norde, W. Physical chemistry of biological interfaces. New York: Marcel Dekker, Inc. **2000**.
25. Why Brewster angle microscopy – BAM. KSV Optrel BAM300 Technical Note. KSV Instruments Ltd.
26. Brewster, D. The Cabinet Cyclopædia: Optics. London: Longman, Orme, Brown, Green, Longmans and John Taylor. **1838**.
27. Brewster, D. On the laws which regulate the polarisation of light by reflexion from transparent bodies. Philosophical Transactions of the Royal Society of London. **1815**. 105:125-159.
28. Lakhtakia, A. Would Brewster recognize today's Brewster angle? Optics News. **1989**. 14-18.
29. Boisseau, P., Houdy, P. and Lahmani, M. Nanoscience: Nanobiotechnology and nanobiology. New York: Springer, **2010**.
30. Bass, M. and Mahajan, V. N. (Eds). Handbook of optics, Volume I – Geometrical and physical optics, polarized light, components and instruments (3rd edition). McGraw-Hill, **2010**.
31. Hönig, D. and Möbius, D. Direct visualization of monolayers at the air-water interface by Brewster angle microscopy. The Journal of Physical Chemistry. **1991**. 95:4590-4592.
32. Joshi, B., Khatavkar, R. and Iyer, N. Brewster angle microscope – An excellent tool for nanoscience researchers. Synthesis and reactivity in inorganic, metal-organic and nano-metal chemistry. **2006**. 36:227-229.
33. Lheveder, C., Hénon, S., Mercier, R., Tissot, G., Fournet, P. and Meunier, J. A new Brewster angle microscope. Review of Scientific Instruments. **1998**. 69 (3):1446-1450.
34. Rivière, S., Hénon, S., Meunier, J., Schwartz, D. K., Tsao, M. W. and Knobler, C. M. Textures and phase transitions in Langmuir monolayers of fatty acids. A comparative Brewster angle microscope and polarized fluorescence microscope study. Journal of Chemical Physics. **1994**. 101 (11):10045-10051.

35. Marshall, G., Dennin, M. and Knobler, C. M. A compact Brewster-angle microscope for use in Langmuir-Blodgett deposition. Review of Scientific Instruments. **1998**. 69 (10):3699-3700.
36. Seki, T., Sekizawa, H. and Ichimura, K. Morphological changes in monolayer of a photosensitive polymer observed by Brewster angle microscopy. Polymer. **1997**. 38 (3):725-728.
37. Cantin, S., Fichet, O., Perrot, F. and Teyssi, D. Spontaneous polymerization at the air-water interface: A Brewster angle microscopy study. Langmuir. **2007**. 23 (24):12243-12248.
38. Uredat, S. and Findenegg, G. H. Brewster angle microscopy and capillary wave spectroscopy as a means of studying polymer films at liquid/liquid interfaces. Colloids and Surfaces A: Physicochemical and Engineering Aspects. **1998**. 142:323-332.
39. Werkman, P. J. and Schouten, A. J. Morphological changes of monolayers to two polymerizable pyridine amphiphiles upon complexation with Cu (II) ions at the air-water interface. Langmuir. **1998**. 14:157-164.
40. Kafi, A. K. M. and Kwon, Y. S. Brewster angle microscopic study of mixed lipid-protein monolayer at the air-water interface and its application in biosensing. Talanta. **2008**. 76:1029-1034.
41. Peñacorada, F., Souto, J., de Saja, J. A. and Brehmer, L. Brewster angle microscopy and surface potential measurements of Langmuir-Blodgett films of zinc tri(tert-butyl)-4-sulphophthalocyanine. Applied Surface Science. **2005**. 246:425-429.
42. Dynarowicz-Łątka, P., Miñones, Jr. J., Conde, O., Casas, M. and Iribarnegaray, E. BAM studies on the penetration of amphotericin B into lipid mixed monolayers of cellular membranes. Applied Surface Science. **2005**. 246:334-341.
43. Sacconi, J., Castano, S., Desbat, B. and Blaudez, D. A phospholipid bilayer supported under a polymerized Langmuir film. Biophysical Journal. **2003**. 85:3781-3787.
44. Gonçalves da Silva, A. M., Romão, R., Andrade, S. M. and Costa, S. Incorporation of β -lactoglobulin bromide studied by Brewster angle microscopy. Colloids and Surfaces B: Biointerfaces. **2003**. 30:259-272.
45. Seoane, R., Miñones, Jr. J., Conde, O., Casas, M. and Iribarnegaray, E. Thermodynamic and Brewster angle microscopy studies of fatty acid/cholesterol mixtures at the air/water interface. The Journal of Physical Chemistry B. **2000**. 104:7735-7744.

46. Vollhardt, D. and Gutberlet, T. Brewster angle microscopy study of supersaturated monolayers of long chain fatty acid methyl esters before and beyond the collapse pressure. *Colloids and Surfaces A: Physicochemical and Engineering Aspects*. **1995**. 102:257-264.
47. Teixeira, A., Brogueira, P., Fernandes, A. and Gonçalves da Silva, A. M. Phase behavior of binary mixtures involving tristearin, stearyl stearate and stearic acid: thermodynamics study and BAM observation at the air-water interface and AFM analysis of LB films. *Chemistry and Physics of Lipids*. **2008**. 153:98-108.
48. Symietz, C., Schneider, M., Brezesinski, G. and Möhwald, H. DNA alignment at cationic lipid monolayers at the air/water interface. *Macromolecules*. **2004**. 37:3865-3873.
49. Melzer, V., Weidemann, G., Vollhardt, D., Brezesinski, G., Wagner, R. and Möhwald, H. Brewster angle microscopy and X-ray GID studies of morphology and crystal structure in monolayers of N-tetradecyl- γ,δ -dihydroxypentanoic acid amide. *The Journal of Physical Chemistry B*. **1997**. 101:4752-4758.
50. Gil, A. and Guitián, F. Formation of 2D colloidal crystals by the Langmuir-Blodgett technique monitored in situ by Brewster angle microscopy. *Journal of Colloid and Interface Science*. **2007**. 307:304-307.
51. Benítez, I. O. and Talham, D. R. Brewster angle microscopy of calcium oxalate monohydrate precipitation at phospholipid monolayer phase boundaries. *Langmuir*. **2004**. 20:8287-8293.
52. Castillo, R., Ramos, S. and Ruiz-Garcia, J. Brewster angle microscopy of fullerene monolayers. *Physica A*. **1997**. 236:105-113.
53. Kozarac, Z., Möbius, D. and Martín Romero, M. T. Characterization of aquatic natural microlayers by monolayer techniques and Brewster angle microscopy. *Water Research*. **2000**. 34 (5):1463-1472.
54. Ding, J., Doudevski, I., Warriner, H. E., Alig, T., Zasadzinski, J. A., Waring, A. J., Sherman, M. A. Nanostructure changes in lung surfactant monolayers induced by interactions between palmitoyloleoylphosphatidylglycerol and surfactant protein B. *Langmuir*. **2003**. 19 (5), 1539-1550.
55. Hodges, C. S., Hammond, R. B. and Gidalevitz, D. Behavior of thin films of poly(oxyethylene) – poly(oxybutylene) copolymers studied by Brewster angle microscopy and atomic force microscopy. *Langmuir*. **2008**. 24:1370-13476.

56. Lawrie, G. A, Gentle, I. R. and Barnes, G. T. The structure of mixed monolayer films of DPPC and hexadecanol. Colloids and Surfaces A: Physicochemical and Engineering Aspects. **2000**. 171:217-224.
57. Lipp, M. M., Lee, K. Y. C., Zasadzinski, J. A and Waring, A. J. Design and performance of an integrated fluorescence, polarized fluorescence, and Brewster angle microscope/Langmuir trough assembly for the study of lung surfactant monolayers. Review of Scientific Instruments. **1997**. 68 (6):2574-2582.
58. Kaercher, T., Hönig, D. and Möbius, D. Brewster angle microscopy: A new method of visualizing the spreading of Meibomian lipids. International Ophthalmology. **1993**. 17:341-348.
59. 1911 Encyclopædia Britannica/Goniometer. Wikisource, The Free Library. Available at: http://en.wikisource.org/w/index.php?title=1911_Encylop%C3%A6dia_Britannica/Goniometer&oldid=1187124. Accessed June 25, 2010.
60. Wikipedia contributors. Goniometer. Wikipedia, The Free Encyclopedia. Available at: <http://en.wikipedia.org/w/index.php?title=Goniometer&oldid=365432297>. Accessed June 25, 2010.
61. Helium-neon laser manual: Visible wavelength helium-neon laser system – User’s guide to operation. Research Electro-Optics, Inc. **2008**.
62. Glan-Laser calcite polarizers. Thorlabs. July 15, 2010. Available at: http://www.thorlabs.com/NewGroupPage9.cfm?ObjectGroup_ID=815.
63. Abramowitz, M. Microscope – Basics and Beyond. New York: Olympus America Inc., **2003**.
64. Piston, D. W. Choosing objective lenses: The importance of numerical aperture and magnification in digital optical microscopy. The Biological Bulletin. **1998**. 195:1-4.
65. Abramowitz, M., Spring, K. R., Ernst Keller, H. and Davidson, M. W. Basic principles of microscope objectives. BioTechniques. **2002**. 33:772-781.
66. Properties of microscope objectives. Nikon Microscopy U. July 20, 2010. Available at <http://www.microscopyu.com/articles/optics/objectiveproperties.html>
67. Infinity optical systems. Nikon Microscopy U. July 20, 2010. Available at <http://www.microscopyu.com/articles/optics/cfintro.html>

68. Microscope components for reflected light applications. Nikon Corporation. **2001**.
69. MicroBAM Manual Version 1. Nima Technology. **2008**.
70. de Mul, M. N. G. and Adin Mann, Jr. J. Determination of the thickness and optical properties of a Langmuir film from the domain morphology by Brewster Angle Microcopy. Langmuir. **1998**. 14:2455-2466.
71. Volinsky, R., Gaboriaud, F., Berman, A. and Jelinek, R. Morphology and organization of phospholipid/diacetylene Langmuir films studied by Brewster angle microscopy and fluorescence microscopy. The Journal of Physical Chemistry. **2002**. 106:9231-9236.
72. Discher, B. M., Schief, W. R., Vogel, V. and Hall, S. B. Phase separation in monolayers of pulmonary surfactant phospholipids at the air-water interface: composition and structure. Biophysical Journal. **1999**. 77:2051-2061.
73. Bringezu, F., Ding, J., Brezesinski, G. B. Waring, A. J. and Zasadzinski, J. A. Influence of pulmonary surfactant protein B on model lung surfactant monolayers. Langmuir. **2002**. 18, 2319-2325.
74. Bringezu, F., Ding, J., Brezesinski, G. and Zasadzinski, J. Changes in model lung surfactant monolayers induced by palmitic acid. Langmuir. **2001**. 17:4641-4648.
75. Antharam, V. C., Elliott, D. W., Mills, F. D., Farver, R. S., Sternin, E. and Long, J. R. Penetration depth of surfactant peptide KL₄ into membranes is determined by fatty acid saturation. Biophysical Journal. **2009**. 96:4085-4098.
76. Palmblad, M., Gustafsson, M., Curstedt, T., Johansson, J. and Schürch, S. Surface activity and film formation from the surface associated material of artificial surfactant preparations. Biochimica et Biophysica Acta (BBA) - Biomembranes. **2001**. 1510:106-117.
77. Rana, F., Harwood, J. S., Mautone, A. J. and Dluhy, R. A. Identification of phosphocholine plasmalogen as a lipid component in mammalian pulmonary surfactant using high-resolution ³¹P NMR spectroscopy. Biochemistry. **1993**. 32, 27-31.
78. Johansson, J., Curstedt, T. and Robertson, B. The proteins of a surfactant system. European Respiratory Journal. **1994**. 7:372-391.
79. McCormack, F. X. and Whitsett, J. A. The pulmonary collectins, SP-A and SP-D, orchestrate innate immunity in the lung. **2002**. 109:707-712.

80. Johansson, J. and Curstedt, T. Molecular structures and interactions of pulmonary surfactant components. *European Journal of Biochemistry*. **1997**. 244:675-693.
81. Kuroki, Y., Takahashi, H., Chiba, H., and Akino, T. Surfactant proteins A and D: disease markers. *Biochimica et Biophysica Acta: Molecular Basis of Disease*. **1998**. 1408, (2-3), 334-345.
82. Crouch, E., Wright, J. R. Surfactant proteins A and D and pulmonary host defense. *Annual Review of Physiology*. **2001**. 63 (1), 521-554.
83. Goerke, J. Pulmonary surfactant: functions and molecular composition. *Biochimica et Biophysica Acta*. **1998**. 1408, 79-89.
84. Mizuno, K., Ikegami, M., Chen, C., Ueda, T. and Jobe, A. H. Surfactant protein-B supplementation improves *in vivo* function of a modified natural surfactant. *Pediatric Research*. **1995**. 37 (3), 271-276.
85. Saleem, M., Meyer, M. C., Breitenstein, D., and Galla, H. J. The surfactant peptide KL₄ in lipid monolayers. *Journal of Biological Chemistry*. **2008**. 283 (8) 5195-5207
86. Whitsett, J. A. and Weaver, T. E. Hydrophobic surfactant proteins in lung function and disease. *The New England Journal of Medicine*. **2002**. 347 (26), 2141-2148.
87. Pinto, R. A., Hawgood, S., Clements, J. A., Benson, B. J., Naidu, A., Hamilton, R. L. and Wright, J. R. Association of surfactant protein C with isolated alveolar type II cells. *Biochimica et Biophysica Acta (BBA)/Lipids and Lipid Metabolism*. **1995**. 1255 (1), 16-22.
88. Long, J. R., Mills, F. D., Ganesh, O. K., Antharam, V. C. and Farver, R. S. Partitioning, dynamics, and orientation of lung surfactant peptide KL₄ in phospholipid bilayers. *Biochimica et Biophysica Acta*. **2010**. 1798:216-222.
89. McIntyre, R. C., Pulido, E. J., Bensard, D. D., Shames, B. D. and Abraham, E. Thirty years of clinical trials in acute respiratory distress syndrome. *Critical Care Medicine*. **2000**. 28 (9) 3314-3331.
90. Cai, P., Flach, C. R. and Mendelsohn, R. An infrared reflection-absorption spectroscopy study of the secondary structure in (KL₄)₄K, a therapeutic agent for a respiratory distress syndrome, in aqueous monolayers with phospholipids. *Biochemistry*. **2003**. 42:9446-9452.

91. Brockman, J. M., Wang, Z., Notter, R. H. and Dluhy, R. A. Effect of hydrophobic surfactant proteins SP-B and SP-C on binary phospholipid monolayers. Biophysical Journal. **2003**. 84 (1):326-340.
92. Dluhy, R. A., Reilly, K. E., Hunt, R. D., Mitchell, M. L., Mautone, A. J. and Mendelsohn, R. Infrared spectroscopic investigations of pulmonary surfactant surface film transitions at the air-water interface. Biophysical Journal. **1989**. 56:1173-1181.
93. Flach, C. R., Cai, P., Dieudonné, D., Brauner, J. W., Keough, K. M., Stewart, J. and Mendelsohn, R. Location of structural transitions in an isotopically labeled lung surfactant SP-B peptide by IRRAS. Biophysical Journal. **2003**. 85:340-349.
94. Mendelsohn, R., Brauner, J. W. and Gericke, A. External infrared reflection absorption spectrometry of monolayer films at the air-water interface. Annual Review of Physical Chemistry. **1995**. 46:305-334.
95. Pastrana-Rios, B., Flach, C. R., Brauner, J. W., Mautone, A. J., Mendelsohn, R. A direct test of the “squeeze-out” hypothesis of lung surfactant function. External Reflection FT-IR at the air/water interface. Biochemistry. **1994**. 33:5121-5127.
96. Shanmukh, S., Biswas, N., Waring, A. J., Walther, F. J., Wang, Z., Chang Y., Notter, R. H. and Dluhy, R. A. Structure and properties of phospholipid-peptide monolayers containing monomeric SP-B₁₋₂₅ II. Peptide conformation by infrared spectroscopy. Biophysical Chemistry. **2003**. 113:233-244
97. Wang, L., Cai, P., Galla, H. J., He, H., Flach, C. R. and Mendelsohn, R. Monolayer-multilayer transitions in a lung surfactant model: IR reflection-absorption spectroscopy and atomic force microscopy. European Biophysical Journal. **2005**. 34:243-254.
98. Smith, E. C., Crane, J. M., Laderas, T. G. and Hall, S. Metastability of a supercompressed fluid monolayer. Biophysical Journal. **2003**. 3048-3057.
99. Chung, J. B., Hannemann, R. E., Franses, E. I. Surface analysis of lipid layers at air-water interfaces. Langmuir. **1990**. 6:1647-1655.
100. Lipp, M. M., Lee, K. Y., Waring, A. and Zasadzinski, J. A. Fluorescence, polarized fluorescence and Brewster angle microscopy of palmitic acid and lung surfactant protein B monolayers. Biophysical Journal. **1997**. 72:2783-2804.
101. Nag, K., Perez-Gil, J., Cruz, A. and Keough, K. M. W. Fluorescently labeled pulmonary surfactant protein C in spread phospholipid monolayers. Biophysical Journal. **1996**. 71:246-256.

102. Nag, K., Perez-Gil, J., Ruano, M. L., Worthman, L. A., Stewart, J., Casals, C. and Keough, K. M. Phase transition in films of lung surfactant at the air-water interface. Biophysical Journal. **1998**. 74:2983-2995.
103. Krüger, P., Schalke, M., Wang, Z., Notter, R., Dluhy, R. A. and Lösche, M. Effect of hydrophobic surfactant peptides SP-B and SP-C on binary phospholipid monolayers. I. Fluorescence and dark-field microscopy. Biophysical Journal. **1999**. 77:903-914.
104. Krol, S., Ross, M., Sieber, M., Künneke, S., Galla, H. J. and Janshoff, A. Formation of three-dimensional protein-lipid aggregates in monolayer films induced by surfactant protein B. Biophysical Journal. **2000**. 79:904-918.
105. Takamoto, D. Y., Lipp, M. M., Nahmen, A. V., Lee, K. Y., Waring, A.J. and Zasadzinski, J. A. Interaction of lung surfactant proteins with anionic phospholipids. Biophysical Journal. **2001**. 81:153-169.
106. Piknova, B., Scheif, W. R., Vogel, V., Discher, B. M. and Hall, S. B. Discrepancy between phase behavior of lung surfactant phospholipids and the classical model of surfactant function. Biophysical Journal. **2001**. 81:2172-2180.
107. Discher, B. M., Malone, K. M. Schief, W. R., Grainger, D. W., Vogel, V. and Hall, S. B. Lateral phase separation in interfacial films of pulmonary surfactant. Biophysical Journal. **1996**. 71:2583-2590.
108. Schief, W. R., Antia, M., Discher, B. M., Hall, S. B. and Vogel, V. Liquid-crystalline collapse of pulmonary surfactant monolayers. Biophysical Journal. **2003**. 84:3792-3806.
109. Lipp, M. M., Lee, K. Y., Zasadzinski, J. A. and Waring, A. J. Phase and morphology changes in lipid monolayers induced by SP-B protein and its amino-terminal peptide. Science. **1996**. 273 (5279), 1196-1199.
110. Lipp, M. M., Lee, K. Y., Takamoto, D. Y., Zasadzinski, J. A. and Waring, A. J. Coexistence of buckled and flat monolayers. Physical Review Letters. **1998**. 81 (8) 1650-1653.
111. Krüger, P., Baatz, J. E., Dluhy, R. A. and Lösche, M. Effect of hydrophobic surfactant protein SP-C on binary phospholipid monolayers. Molecular machinery at the air/water interface. Biophysical Chemistry. **2002**. 99 (3), 209-228.
112. McConlogue, C. W. and Vanderlick, T. K. A close look at domain formation in DPPC monolayers. Langmuir. **1997**. 13:7158-7164.

113. Klenz, U., Saleem, M., Meyer, M. C. and Galla, H. Influence of lipid saturation grade and headgroup charge: A refined lung surfactant adsorption model. *Biophysical Journal*. **2008**. 95:699-709.
114. Nahmen, A. V., Schenk, M., Sieber, M. and Amrein, M. The structure of a model pulmonary surfactant as revealed by scanning force microscopy. *Biophysical Journal*. **1997**. 72:463-469.
115. Flanders, B. N., Vickery, S. A. and Dunn, R. C. Imaging of monolayers composed of palmitic acid and lung surfactant protein B. *Journal of Microscopy*. **2001**. 202 (2), 379-385.
116. Notter, R. H., Tabak, S. A. and Mavis, R. D. Surface properties of binary mixtures of some pulmonary surfactant components. *Journal of Lipid Research*. **1980**. 21:10-22.
117. Wang, Z., Hall, S. B. and Notter, R. H. Dynamic surface activity of films of lung surfactant phospholipids, hydrophobic proteins and neutral lipids. *Journal of Lipid Research*. **1995**. 36:1283-1293.
118. Fleming, B. D. and Keough, K. M. Surface respreading after collapse of monolayers containing major lipids of pulmonary surfactant. *Chemistry and Physics of Lipids*. **1988**. 49 (1-2), 81-6.
119. Liu, H., Lu, R. Z., Turcotte, J. G. and Notter, R. H. Dynamic interfacial properties of surface-excess films of phospholipids and phosphonolipid analogs. I. Effects of pH. *Journal of Colloid and Interface Science*. **1994**. 167 (2), 378-390.
120. Liu, H., Lu, R. Z., Turcotte, J. G. and Notter, R. H. Dynamic interfacial properties of surface-excess films of phospholipids and phosphonolipid analogs. II. Effects of chain linkage and headgroup structure. *Journal of Colloid and Interface Science*. **1994**. 167 (2), 391-400.
121. Longo, M. L., Bisagno, A. M., Zasadzinski, J. A., Bruni, R. and Waring, A. J. A function of lung surfactant protein SP-B. *Science*. **1993**. 261 (5120), 453-456.
122. Taneva, S. G. and Keough, K. M. W. Dynamic surface properties of pulmonary surfactant proteins SP-B and SP-C and their mixtures with dipalmitoylphosphatidylcholine. *Biochemistry*. **1994**. 33 (49), 14660-14670.
123. Putz, G., Goerke, J. Tausch, H. W. and Clements, J. A. Comparison of captive and pulsating bubble surfactometers with use of lung surfactants. *Journal of Applied Physiology*. **1994**. 76 (4), 1425-1431.

124. Chang, C. H., Coltharp, K. A., Park, S. Y., Franses, E. I. Surface tension measurement with the pulsating bubble method. **1996.** 114. 185-197.
125. Putz, G., Goerke, J. Schürch, S. and Clements, J. A. Evaluation of pressure-driven captive bubble surfactometer. *Journal of Applied Physiology.* **1994.** 76 (4), 1417-1424.
126. Crane, J. M., Putz, G. and Hall, S. Persistence of phase coexistence in disaturated phosphatidylcholine monolayers at high surface pressures. *Biophysical Journal.* **1999.** 77:3134-3143.
127. Crane, J. M. and Hall, S. Rapid compression transforms interfacial monolayers of pulmonary surfactant. *Biophysical Journal.* **2001.** 80:1863-1872.
128. Schürch, S., Green, F. and Bachofen, H. Formation and structure of surface films: captive bubble surfactometry. *Biochimica et Biophysica Acta: Molecular Basis of Disease.* **1998.** 1408:180-202.
129. Zuo, Y. Y., Gitiafroz, R., Acosta, E., Policova, Z., Cox, P. N., Hair, M. and Neumann, A. W. Effect of humidity on the adsorption kinetics of lung surfactant at air-water interfaces. *Langmuir.* **2005.** 21:10592-10601.
130. Lee, K. Y., Majewski, J., Kuhl, T. L., Howes, P. B., Kjaer, K., Lipp, M. M., Waring, A. J., Zasadzinski, J. A. and Smith, G. S. Synchrotron x-ray study of lung surfactant-specific protein in SP-B in lipid monolayer. *Biophysical Journal.* **2001.** 81:572-585.
131. Lee, K. Y., Gopal, A., Nahmen, A. V., Zasadzinski, J., Majewski, J., Smith, G. S., Howes, P. B. and Kjaer, K. Influence of palmitic acid and hexadecanol on the phase transition temperature and molecular packing of dipalmitoylphosphatidyl-choline monolayers at the air-water interface. *Journal of Chemical Physics.* **2002.** 116 (2), 774-783.
132. Freitas, J. A., Choi, Y. and Tobias, D. J. Molecular dynamics simulations of a pulmonary surfactant protein B peptide in a lipid monolayer. *Biophysical Journal.* **2003.** 84:2169-2180
133. Kandasamy, S. K. and Larson, R. G. Molecular dynamics study of the lung surfactant peptide SP-B₁₋₂₅ with DPPC monolayers: Insights into interactions and peptide position and orientation. *Biophysical Journal.* **2005.** 88:1577-1592.
134. Lee, H., Kandasamy, S. K. and Larson, R. G. Molecular dynamics simulations of the anchoring and tilting of the lung-surfactant peptide SP-B₁₋₂₅ in palmitic acid monolayers. *Biophysical Journal.* **2005.** 89:3807-3821.

135. Kaganer, V. M., Möhwald, H. and Dutta, P. Structure and phase transitions in Langmuir monolayers. Review of Modern Physics. **1999**. 71 (3), 779-819.
136. McConnell, H. M. Structures and transitions in lipid monolayers at the air-water interface. Annual Review of Physical Chemistry. **1991**. 42:171-195.
137. Zasadzinski, J., Ding, J., Warriner, H. E., Bringezu, F. and Waring, A. J. The physics and physiology of lung surfactant. Current Opinion in Colloid and Interface Science. **2001**. 6:506-513.
138. Degen, P., Rehage, H., Klärner, F. and Polkowska, J. Characterization of Langmuir monolayers of molecular clips by means of Brewster angle microscopy. Colloid and Polymer Science. **2005**. 284:44-50.
139. Sovago, M., Wurpel, G. W., Smits, M., Müller, M. and Bonn, M. Calcium-induced phospholipid ordering depends on surface pressure. Journal of the American Chemical Society. **2007**. 129 (36), 11079-11084.
140. Estrela-Lopis, I., Brezenski, G. and Möhwald, H. Miscibility of DPPC and DPPA in monolayers at the air/water interface. Chemistry and Physics of Lipids. **2004**. 131:71-80.
141. Mecke, K. and Stoyan D. (Eds). Morphology of condensed matter – Physics and geometry of spatially complex systems. New York: Springer-Verlag Berlin Heidelberg. **2002**.
142. Roke, S., Schins, J., Müller, M. and Bonn, M. Vibrational spectroscopic investigation of the phase diagram of a biomimetic lipid monolayer. Physical Review Letters. **2003**. 90 (12), 128101-1 – 128101-4.
143. Romão, R. and Gonçalves da Silva, G. Phase behavior and morphology of binary mixtures of DPPC with stearonitrile, acetic acid, and octadecanol at the air-water interface. Chemistry and Physics of Lipids. **2004**. 131 (1):27-39.
144. Casillas-Ituarte, N. N., Chen, X., Castada, H. and Allen, H. C. Na⁺ and Ca²⁺ effect on the hydration and orientation of the phosphate group of DPPC at air–water and air–hydrated silica interfaces. The Journal of Physical Chemistry B. **2010**. 114 (29):9485-9495.
145. McConnell, H. M. and Moy, V. T. Shapes of finite two-dimensional lipid domains. The Journal of Physical Chemistry. **1988**. 92:4520-4525.

146. Keller, D. J., Korb, J. P. and McConnell, H. M. Theory of shape transitions in two-dimensional phospholipid domains. The Journal of Physical Chemistry. **1987**. 91 (25):6417-6422.
147. Mayer, M. A. and Vanderlick, T. K. Monte Carlo simulation of the shapes of domains in phospholipid monolayers. Physical Review E. **1997**. 55 (1):1106-1119.
148. David, A., Franoise, B. and Jean-Francois, J. Phase transitions in Langmuir monolayers of polar molecules. The Journal of Chemical Physics. **1987**. 86 (6):3673-3681.
149. Takahiro, A., Yamamoto, T., Ou-Yang, W., Manaka, T. and Iwamoto, M. Study of the domain shapes and orientational structure of phospholipid monolayers using Maxwell displacement current and Brewster angle microscopy. Japanese Journal of Applied Physics. **2008**. 47 (1):411-415.
150. Lee, K. Y. C. Collapse mechanism of Langmuir monolayers. The Annual Review of Physical Chemistry. **2008**. 59:771-791.
151. Bernhard, W., Mottaghian, J., Gebert, A. Rau, G. A., Hardt, H. and Poets, C. F. Commercial versus native surfactants. American Journal of Respiratory and Critical Care Medicine. **2000**. 162:1524-1533.
152. Sierra-Hernández, M. R. Spectroscopic studies of atmospheric relevant air-aqueous interfaces. Unpublished doctoral dissertation, The Ohio State University, Ohio, United States of America, **2010**.
153. Tang, C. Y. Interfacial studies of fatty acid monolayers: structure, organization and solvation by sum frequency generation vibrational spectroscopy. Unpublished doctoral dissertation, The Ohio State University, Ohio, United State of America, **2010**.
154. Cochrane, C. G. and Revak, S. D. Pulmonary surfactant protein B (SP-B): Structure-function relationships. Science. **1991**. 254 (5031):566-568.
155. Weidemann, G. and Vollhardt, D. Long-range tilt orientational order in phospholipid monolayers: A comparative study. Biophysical Journal. **1996**. 70, 2758-2766.
156. Hawgood, S. and Shiffer, K. Structures and properties of the surfactant-associated proteins. Annual Review of Physiology. **1991**. 53:375-394.

157. Hawgood, S., Benson, B. J., and Hamilton, Jr. R. Effects of a surfactant-associated protein and calcium ions on the structure and surface activity of lung surfactant lipids. *Biochemistry*. **1985**. 24:184-190.
158. Revak, S. D., Merritt, T. A., Hallman, M., Heldt, G., La Polla, R. J., Hoey, K., Houghten, R. and Cochrane, C. G. The use of synthetic peptides in the formation of biophysically and biologically active pulmonary surfactants. *Pediatric Research*. **1991**. 29 (5):460-465.
159. Mills, F. D., Antharam, V. C., Ganesh, O. K., Elliott, D. W., McNeill, S. A. and Long, J. R. The helical structure of surfactant peptide KL₄ when bound to POPC: PPG lipid vesicles. *Biochemistry*. **2008**. 47 (32):8292-8300.
160. Elert, G. (Ed). Index of refraction (Table salt). The Physics Factbook. Available at: <http://hypertextbook.com/facts/2005/AlinaGenis.shtml>. Accessed July 13, 2010.
161. Subedi, D. P., Adhikari, D. R., Joshi, U. M., Poudel, H. M and Niraula, B. Study of temperature and concentration dependence of refractive index of liquids using a novel technique. *Kathmandu University Journal of Science, Engineering and Technology*. **2006**. 2 (1):1-7.
162. Aroti, A., Leontidis, E., Maltseva, E. and Brezesinski, G. Effects of hofmeister anions on DPPC Langmuir monolayers at the air-water interface. *Journal of Physical Chemistry B*. **2004**. 108:15238-15245.
163. Weidemann, G. and Vollhardt, D. Long range tilt orientation order in phospholipid monolayers: a comparison of the order in the condensed phases of dimyristoylphosphatidylethanolamine and dipalmitoylphosphatidylcholine. *Colloids and Surfaces A: Physicochemical and Engineering Aspects*. **1995**. 100:187-202.
164. Weidemann, G. and Vollhardt, D. Long-range tilt orientational order in phospholipid monolayers: the inner structure of dimyristoyl-phosphatidyl-ethanolamine domains. *Thin Solid Films*. **1995**. 262 (1):94-103.
165. Cochrane, C. G., Revak, S. D., Merritt, T. A., Heldt, G. P., Hallman, M., Cunningham, M. D., Easa, D., Pramanik, A., Edwards, D. K. and Alberts, M. S. The efficacy and safety of KL₄-surfactant in preterm infants with respiratory distress syndrome. *American Journal of Respiratory and Critical Care Medicine*. **1996**. 153:404-410.
166. Saxena, S. Lung surfactant: The indispensable component of respiratory mechanics. *Resonance: Journal of Science Education*. **2005**. 10 (8):91-96.

167. Schürch, S., Lee, M. and Gehr, P. Pulmonary surfactant: Surface properties and function of alveolar and airway surfactant. Pure & Applied Chemistry. **1992**. 64 (11):1745-1750.

168. Ding, J., Warriner, H. E. and Zasadzinski, J. A. Magnetic needle viscometer for Langmuir monolayers. Langmuir. **2002**. 18:2800-2806.

169. Ding, J., W. H. E. and Zasadzinski, J. A. Viscosity of two-dimensional suspensions. Physical Review Letters. **2002**. 88 (16), 168102-1–168102-4.